Analysis of a Multi-Scale Asymptotic Model for Internal Gravity Waves in a Moist Atmosphere

Dissertation zur Erlangung des Grades
Doktor der Naturwissenschaften
am Fachbereich Mathematik & Informatik
der Freien Universität Berlin.

Daniel Ruprecht

Berlin 2010

1. Gutachter & Betreuer:
Prof. Dr. Rupert Klein, *Institut für Mathematik, Freie Universität Berlin*

2. Gutachter:
Prof. Andrew J. Majda, *Courant Institute of Mathematical Sciences, New York University*

Datum der Disputation:
13. Juli 2010

Contents

Chapter 1.

Introduction

Internal gravity waves in atmospheric flows are found on scales ranging from the order of 10 km as in figure 1.1 to the order of 100 km, cf. figure 1.2[1]. Their restoring mechanism is based on the stratification of density with height in the atmosphere, which is usually stable to vertical displacements of air parcels. One important source of atmospheric gravity waves is flow over hills and mountains, exciting so-called orographic or lee waves, see e.g. [Sco49] for an early work and [WSD96] for a comprehensive review. Another important source of waves is deep convection. There has been some debate about the essential mechanism that causes deep convection to generate gravity waves, see e.g. [FDH91, LRC01] for discussions.

Understanding the dynamics of gravity waves is important for atmospheric sciences for several reasons. The pioneering works of [Saw59, Lin81] show that the dissipation of breaking internal waves in the stratosphere exerts a force called "gravity wave drag" (GWD) on mid-atmospheric flows. Contemporary weather forecasting as well as climate modelling extensively employ models for planetary-scale flows, so-called "global circulations models" (GCMs). As for example [McL98] shows, including the effect of GWD in those models is essential to obtain realistic mid-atmospheric flows. Because internal waves are too small in scale to be resolved in GCMs, parameterizations of GWD are required. See [KEC03] for a detailed overview, including a comprehensive discussion of several wave-exciting processes. Recently, [JSL+08] found that gravity waves are also important for the parameterization of cirrus clouds.

Internal waves also play an important role in several other meteorological phenomena. [BS89, LR01] present simulations of how a single deep convective cloud affects its environment by emitting gravity waves. By reducing "convective inhibition" (CIN) around the cloud, waves are found to render the "cloud free environment" (CFE) favorable for further convection. In a similar direction points the investigation of a possible feedback mechanism between gravity waves and condensation regions triggering convection in [CEL80]. The possibility of moist convection being triggered by waves is also investigated in [EL75]. Through interactions of

[1] From http://en.wikipedia.org/wiki/Gravity_wave, both figures are public domain.

Figure 1.1.: *Clouds caused by gravity waves. Theresa, Wisconsin, USA.*

this type, gravity waves supposedly are involved in clustering of convection. See [Map93, LM04] for investigations of this hypothesis.

However, atmospheric internal waves not only prepare or trigger moist convection but their propagation characteristics are also modulated by moisture in return. Most importantly, if a parcel is lifted sufficiently to start condensation, the released latent heat offsets some of the cooling by adiabatic expansion and reduces the exerted restoring force. In a conditionally unstable atmosphere, the parcel becomes positively buoyant and moist convection is initiated.

This thesis presents the derivation, analysis and extension of a reduced model for propagation of internal gravity waves in an atmosphere containing deep convective clouds, so-called "hot towers". The derivation is based on techniques from multiple scale perturbation theory, commonly used in applied mathematics, see e.g. [KC96]. Perturbation methods rely on the identification of small, non-dimensional parameters in a set of intricate equations governing the "full" physics of an investigated problem and try to identify a set of simplified equations valid in the limit of vanishing small parameters. In most cases, the full system is very difficult to analyze, let alone to solve, and usually the only way to obtain approximate solutions is by solving the full equations numerically. Reduced models are often much more accessible to mathematical analysis and can thus allow for a concise study of the essential effects, yielding valuable physical insight into the dynamics of the studied problem. Analytical approaches to the problem of interactions between gravity waves and moisture are scarce and most studies rely on numerical modeling, cf. the comments in the introduction in [MR05].

The general framework employed for the derivation of the presented model is developed in [Kle04, Kle08, Kle10]. It provides tools for a systematic derivation of

reduced models in atmospheric sciences and also allows for methodical development of models for interactions of processes on different time- and lengthscales, see [Maj07] for an example. The basics of the derivation are adopted with minor modifications from [KM06]. A closure relying on conditional averaging over the lengthscale of the convective towers is applied to the obtained leading order equations. It allows to derive a set of closed equations by purely analytical means without requiring approximations besides adopting a certain asymptotic regime. The final model is an extension of the well-known linearized anelastic equations, which are widely used to describe propagation of internal gravity waves.

The goal of the present thesis is a thorough analysis and discussion of the resulting model with a focus on the effects arising from the presence of moisture. The analysis confirms some findings of existing works, for example a reduction of momentum flux and inhibition of wave propagation by moisture. Further, new hypotheses on the influence of moisture on gravity wave propagation are formulated: (i) introduction of a lower cut-off horizontal wavenumber and (ii) the ability of moisture to cause critical layers in otherwise non-critical flows. Both are, to the author's knowledge, new hypotheses.

An early series of works investigating the effect of latent heat release on internal waves is [Lal72, EL73a, EL73b]. One essential result of these works is that moisture reduces the effective stability frequency governing internal wave propagation. Further, moisture is found to inhibit the propagation of waves and to increase vertical wavelengths. While the model in the present thesis also features a reduced effective stability, it exhibits a decrease of vertical wavelength by moisture instead. A reduction of the effective stability by moisture is also indicated in [DK82].

[BJD79, BJB80, BF85] present a model switching between a dry and a moist stability frequency depending on the displacement of a parcel. A similar mechanism is found in the presented model, although the multi-scale approach results in a continuous transition between a nearly moist adiabat background and a moist-neutral stratification. Their analysis demonstrates that moisture can exert significant influence on wave induced momentum flux which is closely related to GWD. Strong reduction of momentum flux by moisture is verified in [JB85] by employing a two-dimensional, anelastic, non-hydrostatic model containing a bulk micro-physics scheme for the evolution of the density of vapor and liquid water. Reduced momentum flux and wave amplitudes by moisture are also indicated in the results presented in [DK83], who employ a two-dimensional, compressible, non-hydrostatic model containing a bulk scheme for vapor, cloud water and rain water for the simulation of mountain waves. The model presented in this thesis also features a reduced effective stability and inhibition of wave propagation by moisture. More recent simulations results on interactions of moisture with orographic waves are found for example in [MB03, MR05] who use the weather research & forecasting model (WRF) [2] to investigate flow over topography in an atmosphere close to moist-neutral stratification in order to identify different flow regimes.

[2] See http://wrf-model.org.

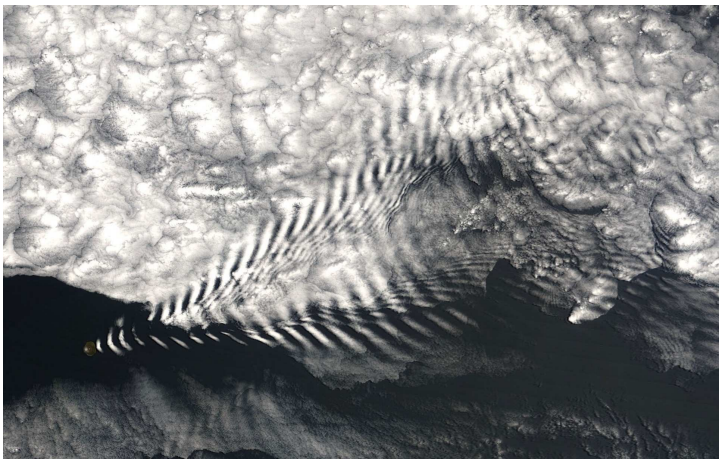

Figure 1.2.: *Wave clouds near Amsterdam Island, picture taken by MODIS on the NASA satellite Terra. Shown is an area with a size of roughly* $600km \times 450km$. *For more information on this image, check out* http://earthobservatory.nasa.gov/IOTD/view.php?id=6151.

Despite the numerous works indicating that moisture can significantly modify the characteristics of gravity waves and especially the generated GWD, there seem to be only very few works aimed at including moisture effects into parameterizations of orographic wave drag. The review [KEC03] mentions only [Sur89], who investigates the effect of replacing the dry stability frequency by a moist counterpart in a GWD parameterization. More recently, this approach has been employed in [Joo09]. In both cases, despite the simplistic representation, better results are obtained by including the moist stability frequency. The insights gained by the analysis of the reduced model performed in the present thesis might help in further advancement at this point. Because of the similarity of the essential moisture-related parameter in the presented model to a routinely computed parameter in GCMs as well as the simple linear structure of the equations, the reduced model itself might constitute a good starting point for developing parameterizations of orographic wave drag that take effects of moisture on GWD into account.

The present thesis consists of six chapters besides this introduction. A reader interested primarily in the essential results may want to skip the details of the derivation and go directly to the summary of the model in 2.2.6 and then continue with the results of the mathematical and numerical analysis presented in chapters 3 and 5. Section 2.1 briefly presents the employed general framework while 2.2 discusses in detail the derivation. Chapter 4 introduces the numerical scheme used to compute approximate time-dependent solutions of the model. Chapter 6 presents an extension of the model to the regime of small saturation deficits, featuring nonlinear interaction of saturated area fraction and vertical velocity. Finally, 7 provides a brief summary of the thesis.

Chapter 2.

Model Derivation

This chapter presents the derivation of the final closed model (2.70), subsequently analyzed in the following chapters. Section 2.1 outlines the necessary tools for the derivation: The governing equations in non-dimensional form, the arising non-dimensional parameters and the used micro-physics model are discussed in the subsections 2.1.1 and 2.1.3 while subsection 2.1.2 presents the distinguished limit connecting the small parameters. Section 2.1.4 classifies the ansatz in the context of the unified modelling approach discussed in the introduction. In section 2.2, after a brief explanation of the mechanics of internal waves, the actual derivation is given. The scales and coordinates as well as the asymptotic expansions involved in the ansatz are introduced in subsection 2.2.2. The resulting leading order equations are collected in subsection 2.2.4. From these, the final model (2.70) is obtained by applying a suitable closure strategy as demonstrated in subsection 2.2.5. The chapter ends with subsection 2.2.7 briefly discussing the essential moisture-related parameter arising in the model.

2.1. Tools for the Derivation

2.1.1. Governing Equations

The equations describing the flow of a compressible fluid are derived from the principles of conservation of mass, momentum and energy, see for example ch. 4 in [Gil82]. Assuming smooth solutions or interpreting derivatives in an appropriate sense, these integral conservation principles can be transformed into a set of partial differential equations for velocity, density ρ and energy, here given as potential temperature θ, which is explained below. The velocity field $\mathbf{v} = (\mathbf{u}, w)$ is split into its horizontal part $\mathbf{u} = (u, v)$ and its vertical part w. The non-dimensionalized version of these equations, given in [KM06], reads

$$\begin{aligned}
\rho_t + \nabla_\parallel \cdot (\rho \mathbf{u}) + (\rho w)_z &= 0 \\
\mathbf{u}_t + \mathbf{u} \cdot \nabla_\parallel \mathbf{u} + w\mathbf{u}_z + \frac{1}{\mathrm{Ro_B}} (\boldsymbol{\Omega} \times \mathbf{v})_\parallel + \frac{1}{\mathrm{M}^2} \frac{1}{\rho} \nabla_\parallel p &= \mathbf{D_u} \\
w_t + \mathbf{u} \cdot \nabla_\parallel w + ww_z + \frac{1}{\mathrm{Ro_B}} (\boldsymbol{\Omega} \times \mathbf{v})_\perp + \frac{1}{\mathrm{M}^2} \frac{1}{\rho} p_z &= D_w - \frac{1}{\overline{\mathrm{Fr}}^2} \\
\theta_t + \mathbf{u} \cdot \nabla_\parallel \theta + w\theta_z &= D_\theta + S_\theta.
\end{aligned} \tag{2.1}$$

The pressure p is related to the other variables by the ideal gas law

$$p = (\rho\theta)^\gamma . \tag{2.2}$$

Just as the velocity field, the gradient in (2.1) is split into the horizontal part $\nabla_\parallel = (\partial_x, \partial_y)$ and the vertical part ∂_z. The terms $\mathbf{D_u}$ and D_w represent the effects of turbulent and molecular transport processes. They are assumed to be negligible and set to zero in the course of this thesis. $\boldsymbol{\Omega}$ is the vector of earth rotation. The subscript $\perp$ denotes projection onto the vertical, while $\parallel$ denotes projection onto the horizontal tangential plane. S_θ models sources of energy, e.g. latent heat, radiation, heat fluxes from the surface, etc. Finally, (2.1) contains three non-dimensional parameters:

$$\mathrm{M} = \frac{u_{\mathrm{ref}}}{\sqrt{p_{\mathrm{ref}}/\rho_{\mathrm{ref}}}} = \frac{u_{\mathrm{ref}}}{c_{\mathrm{sound}}} \tag{2.3}$$

is the Mach-number and denotes the ratio of the typical velocity of the fluid to the speed of sound-waves.

$$\overline{\mathrm{Fr}} = \frac{u_{\mathrm{ref}}}{\sqrt{g h_{\mathrm{scale}}}} = \frac{u_{\mathrm{ref}}}{c_{\mathrm{barotropic}}} \tag{2.4}$$

is the barotropic Froude-number and denotes the ratio of the flow velocity to the speed of barotropic gravity waves.

$$\mathrm{Ro_B} = \frac{u_{\mathrm{ref}}}{l_{\mathrm{bulk}} f} \tag{2.5}$$

is the bulk Rossby-number. l_{bulk} is a reference lengthscale for the bulk microphysics and f is the Coriolis parameter. In the derivation, M, $\overline{\mathrm{Fr}}$ and $1/\mathrm{Ro_B}$ are considered small parameters, indicating that for the studied regime, sound-waves and barotropic gravity waves have negligible influence, while $1/\mathrm{Ro_B} \ll 1$ indicates that Coriolis forces are of little importance.

Potential Temperature

Potential temperature is introduced to allow for reasonably comparing the temperatures of air parcels at different heights in the atmosphere. It is closely related

to the stability of the atmosphere with respect to vertical displacements, see the discussion in subsection 2.2.1. Potential temperature is defined as the temperature a parcel **would** acquire, if moved adiabatically, i.e. without heat exchange with its environment, to a reference pressure p_{ref} usually set to $p_{\mathrm{ref}} = 1000$ hPa. It is related to sensible temperature T by

$$\theta = T \left(\frac{p_{\mathrm{ref}}}{p} \right)^{\kappa}, \tag{2.6}$$

whereas p is the pressure of the parcel at its original height.

$$\kappa = \frac{R}{c_{\mathrm{p}}} = \frac{c_{\mathrm{p}} - c_{\mathrm{v}}}{c_{\mathrm{p}}} \tag{2.7}$$

is called the isentropic exponent. R is the gas constant while c_{p} and c_{v} are the specific heats of air for constant pressure and volume, respectively. In a moist atmosphere, the situation is complicated by the fact that c_{p}, c_{v} depend on the amount of water contained in the parcel. In [Etl96], (2.6) is derived for the dry case while [Ema94] provides a detailed discussion of the moist case.

2.1.2. Distinguished Limit

Following [MK03, KM06], the three arising non-dimensional parameters are connected by a universal expansion parameter ε in the distinguished limit

$$\mathrm{M} \sim \overline{\mathrm{Fr}} \sim \varepsilon^2 \,, \quad \frac{1}{\mathrm{Ro_B}} \sim \varepsilon \quad \text{as} \quad \varepsilon \to 0. \tag{2.8}$$

By this limit, (2.1) becomes

$$\begin{aligned} \rho_t + \nabla_{\|} \cdot (\rho \mathbf{u}) + (\rho w)_z &= 0 \\ \mathbf{u}_t + \mathbf{u} \cdot \nabla_{\|} \mathbf{u} + w \mathbf{u}_z + \varepsilon f \left(\Omega \times \vec{v} \right)_{\|} + \varepsilon^{-4} \frac{1}{\rho} \nabla_{\|} p &= 0 \\ w_t + \mathbf{u} \cdot \nabla_{\|} w + w w_z + \varepsilon \left(\Omega \times \vec{v} \right)_{\perp} + \varepsilon^{-4} \frac{1}{\rho} p_z &= -\varepsilon^{-4} \\ \theta_t + \mathbf{u} \cdot \nabla_{\|} \theta + w \theta_z &= \varepsilon^2 \left(\tilde{S}_\theta^\varepsilon + S_\theta^{q,\varepsilon} \right). \end{aligned} \tag{2.9}$$

The source term S_θ in (2.1) is split into $\tilde{S}_\theta^\varepsilon$, related to external sources of energy like radiation or fluxes of sensible heat from the ground into the air, and $S_\theta^{q,\varepsilon}$, modelling heat release and consumption by micro-physical processes. This thesis focusses on interaction with moisture, so $\tilde{S}_\theta^\varepsilon$ is assumed to be zero. To close the equations, $S_\theta^{q,\varepsilon}$ has to be connected to the prognostic quantities. Usually this is done by introducing additional assumptions based on physical arguments. In contrast, the model in the present thesis features an analytically computed closure outlined

in section 2.2, based on the combination of the dynamical equations (2.1) with the bulk micro-scale model discussed in subsection 2.1.3. The closure procedure essentially consists of deriving an expression for the leading order contribution from $S_\theta^{q,\varepsilon}$ out of the leading order equations obtained from (2.13).

2.1.3. Bulk Micro-Physics Model

The dynamic equations (2.9) are coupled with a bulk warm micro-physics model, see [Gra98] for a detailed discussion. "Warm" indicates that no ice phase is included in the model. The model features three moist quantities q_v, q_c, q_r measured in mixing ratios, i.e.

$$q_\mathrm{i} = \frac{m_i}{m_\mathrm{d}} \ , \quad i = \mathrm{v}, \mathrm{c}, \mathrm{r} \tag{2.10}$$

whereas m_i is the mass of the corresponding species while m_d is the mass of dry air. q_v is water vapor, i.e. water in gas phase. q_c is cloud water, representing small, hovering droplets while q_r is rain water, i.e. droplets that are large enough to fall down. By dividing through the volume of a considered parcel, mixing ratios can also be expressed as density ratios

$$q_\mathrm{i} = \frac{\rho_i}{\rho_\mathrm{d}} \ , \quad i = \mathrm{v}, \mathrm{c}, \mathrm{r}. \tag{2.11}$$

Note the difference between the water vapor mixing ratio and the specific humidity, defined as the ratio of the mass of water vapor to the mass of *moist* air, i.e.

$$s = \frac{m_\mathrm{v}}{m_\mathrm{m}} = \frac{m_v}{m_\mathrm{d} + m_\mathrm{t}} \tag{2.12}$$

where m_t is the total mass of water. Because in most situations $m_\mathrm{t} \ll m_\mathrm{d}$, the specific humidity is often a good approximation of the vapor mixing ratio.

The employed model includes four conversion mechanisms between the species, emerging as source terms in the equations:

1. *Evaporation:* C_ev is the evaporation of rain water into water vapor.
2. *Condensation:* C_d is the condensation of water vapor into cloud water or, if $C_\mathrm{d} < 0$, the evaporation of cloud water into water vapor.
3. *Auto-conversion:* C_ac denotes the accumulation of cloud water droplets into rain water.
4. *Collection:* C_cr denotes the collection of cloud water droplets by falling rain water.

Again neglecting the effects of turbulent and molecular transport, the bulk micro-physics model adopted from [KM06] reads

$$\begin{aligned} q_{\mathrm{v},t} + \mathbf{u}\cdot\nabla_{\parallel} q_{\mathrm{v}} + w q_{\mathrm{v},z} &= C_{\mathrm{ev}} - C_{\mathrm{d}} \\ q_{\mathrm{c},t} + \mathbf{u}\cdot\nabla_{\parallel} q_{\mathrm{c}} + w q_{\mathrm{c},z} &= C_{\mathrm{d}} - C_{\mathrm{ac}} - C_{\mathrm{cr}} \\ q_{\mathrm{r},t} + \mathbf{u}\cdot\nabla_{\parallel} q_{\mathrm{r}} + w q_{\mathrm{r},z} + \frac{1}{\rho}\left(\rho q_{\mathrm{r}} V_{\mathrm{T}}\right)_z &= C_{\mathrm{ac}} + C_{\mathrm{cr}} - C_{\mathrm{ev}}. \end{aligned} \tag{2.13}$$

V_{T} denotes the terminal velocity of rain droplets and is assumed to be constant. By careful scaling of the source terms, the right hand side terms in (2.13) can be rescaled by powers of ε, see again [KM06] for the details. The resulting rescaled model reads

$$\begin{aligned} q_{\mathrm{v},t} + \mathbf{u}\cdot\nabla_{\parallel} q_{\mathrm{v}} + w q_{\mathrm{v},z} &= -\varepsilon^{-n}\hat{C}_{\mathrm{d}} + \hat{C}_{\mathrm{ev}} \\ q_{\mathrm{c},t} + \mathbf{u}\cdot\nabla_{\parallel} q_{\mathrm{c}} + w q_{\mathrm{c},z} &= \varepsilon^{-n}\hat{C}_{\mathrm{d}} - \varepsilon^{-1}\hat{C}_{\mathrm{cr}} - \hat{C}_{\mathrm{ac}} \\ q_{\mathrm{r},t} + \mathbf{u}\cdot\nabla_{\parallel} q_{\mathrm{r}} + w q_{\mathrm{r},z} + \frac{1}{\rho}\left(V_{\mathrm{T}}^{**}\rho q_{\mathrm{r}}\right)_z &= \varepsilon^{-1}\hat{C}_{\mathrm{cr}} - \hat{C}_{\mathrm{ev}} + \hat{C}_{\mathrm{ac}}. \end{aligned} \tag{2.14}$$

The exponent $n \gg 1$ in the coefficient of the source term C_{d} is a measure of how fast condensation and evaporation take place. In the model derived here, n is sufficiently large, so that on the considered timescales these processes are instantaneous and transient changes would be seen only on faster timescales.

The moisture related energy source term $S_\theta^{q,\varepsilon}$ in $(2.9)_4$ in rescaled form reads

$$S_\theta^{q,\varepsilon} = \Gamma^{**} L^{**} q_{\mathrm{vs}}^{**} \frac{\theta}{p}\left(\varepsilon^{-n}\hat{C}_{\mathrm{d}} - \hat{C}_{\mathrm{ev}}\right). \tag{2.15}$$

To close the model, the source terms have to be expressed as functions of the three moist species

$$\begin{aligned} \hat{C}_{\mathrm{d}} &= C_{\mathrm{d}}^{**}\left(q_{\mathrm{v}} - q_{\mathrm{vs}}\right) H_{\circ}\left(q_{\mathrm{c}}, q_{\mathrm{v}}, q_{\mathrm{vs}}\right)\left(q_{\mathrm{c}} + \varepsilon q_{\mathrm{cn}}^{**}\right) \\ \hat{C}_{\mathrm{ev}} &= -C_{\mathrm{ev}}^{**}\left(q_{\mathrm{v}} - q_{\mathrm{vs}}\right) H_{>}(q_{\mathrm{r}})\sqrt{q_{\mathrm{r}}} \\ \hat{C}_{\mathrm{cr}} &= C_{\mathrm{cr}}^{**} q_{\mathrm{c}} q_{\mathrm{r}} \\ \hat{C}_{\mathrm{ac}} &= C_{\mathrm{ac}}^{**}\max\left(0, q_{\mathrm{c}} - \varepsilon q_{\mathrm{c}}^{**}\right). \end{aligned} \tag{2.16}$$

See [KM06] for the definition of the weighting functions $H_{>}$ and $H_{\circ}$. The double-star quantities are $\mathcal{O}(1)$ scaling factors emerging from the non-dimensionalization.

2.1.4. Unified Modelling Framework

In [Kle04] a framework for the systematic derivation of reduced meteorological models based on multi-scale asymptotic techniques is developed. It consists of the identification of a set of scale-independent reference quantities, valid for the full

range of atmospheric flows. These quantities are combined into three characteristic non-dimensional parameters π_1, π_2, π_3. These are connected by a universal expansion parameter ε in a distinguished limit

$$\pi_1 = \mathcal{O}(1) \ , \quad \pi_2 = \mathcal{O}(\varepsilon^2) \ , \quad \pi_3 = \mathcal{O}(\varepsilon^3) \ , \quad \text{as } \varepsilon \to 0. \tag{2.17}$$

Note that in the later advancements of the framework in [Kle08, Kle10], a different set of parameters is used and the distinguished limit is slightly modified. The distinguished limit (2.8) used in this thesis can be obtained from (2.17) by expressing the dimensionless parameters in (2.8) in terms of π_1, π_2, π_3, see [Kle04].

Addressing Regimes by Choosing Specific Coordinates

The universal scales identified in the framework are a lengthscale of 10 km and a timescale of 1000 s with corresponding coordinates labeled $\mathbf{x}$, z and t. To address a particular regime characterized by specific scales, a set of coordinates resolving these scales is introduced by rescaling $\mathbf{x}$, z and t by powers of ε. All quantities are then expanded in asymptotic series, whose general form reads

$$\mathcal{U}(\mathbf{x}, z, t; \varepsilon) = \sum_{i \in \mathbb{N}} \phi^{(i)}(\epsilon) \mathcal{U}^{(i)} \left(\ldots, \varepsilon^{-1}t, t, \varepsilon t, \ldots, \varepsilon^{-1}\mathbf{x}, \mathbf{x}, \varepsilon\mathbf{x}, \ldots, \varepsilon^{-1}z, z, \varepsilon z, \ldots \right). \tag{2.18}$$

The $\phi^{(i)}$ in (2.18) are asymptotic scaling functions and have to satisfy

$$\phi^{(i+1)}(\varepsilon) = o(\phi^{(i)}(\varepsilon)) \quad \text{as} \quad \varepsilon \to 0 \tag{2.19}$$

for the expansions to remain valid. In a concrete case, the coefficients $\mathcal{U}^{(i)}$ are allowed to depend exactly on the coordinates resolving the scales characterizing the investigated regime.

For example, the coordinates

$$\varepsilon^2 t \ , \quad \varepsilon^2 \mathbf{x} \ , \quad z \tag{2.20}$$

resolve a horizontal scale of $\sim$ 1000 km, a vertical scale of $\sim$ 10 km and a timescale of approximately one day. These scales correspond to the regime of quasi-geostrophic flow and the ansatz

$$\mathcal{U}^{(i)}(\varepsilon^2\mathbf{x}, z, \varepsilon^2 t) \tag{2.21}$$

does indeed yield the well-known quasi-geostrophic model. The detailed derivation can be found in [Kle08].

This unified approach allows for the re-derivation of a large number of well-known meteorological models, see table 1 in [Kle04]. It also provides a systematic approach for the derivation of new models, including models for the study of interactions between phenomena acting on different scales, see the examples cited in [Kle08]. In the present thesis, this framework is employed to derive a model describing interactions of non-hydrostatic gravity waves with deep convective hot towers.

2.2. Derivation

2.2.1. Internal Gravity Waves

Borrowing the definition from p. 205 in [Lig78], gravity waves are waves *"driven by a balance between fluid's inertia and its tendency, under gravity, to return to a state of stable equilibrium with heavier fluid underlying lighter"*. Surface gravity waves arise at the interface between two fluids with different density, for example at the sea surface between water and air. These waves can travel only along the interface, i.e. in case of the ocean surface, solely in the horizontal. Internal gravity waves occur inside a stratified fluid, stable to vertical displacements, i.e. fluids inside which density decreases continuously with height.

The central mechanism in the generation of internal gravity waves under dry conditions is sketched briefly here following section 6.4 in [Etl96]. Consider a parcel of air with mass m_p, displacing air of mass m. By Archimedes' law, the buoyancy force acting on this parcel is

$$B = (m - m_\mathrm{p})\, g \tag{2.22}$$

with g being the gravitational acceleration, i.e. $g \approx 9.81$ m s^{-2}. Denote by $z(t)$ the parcel's height at time t. By Newton's law, the acceleration due to buoyancy equals

$$B = m_\mathrm{p}\ddot{z}(t) = (m - m_\mathrm{p})\, g \tag{2.23}$$

or, dividing by the volume of the parcel equal to the volume of the displaced air,

$$\ddot{z}(t) = \frac{\rho - \rho_\mathrm{p}}{\rho_\mathrm{p}} g \tag{2.24}$$

whereas ρ_p is the parcel's density while ρ is the density of the environment. The following assumptions are made:

1. The thermodynamic state of the parcel changes adiabatically, i.e. its potential temperature is constant.
2. The pressure of the air parcel is identical to the pressure in the environment, i.e. $p_\mathrm{p} = p$.
3. The mass of the parcel is constant, i.e. mixing can be neglected.

Note that assumption 1 is violated, if the parcel produces precipitating condensate. However, this brief outline does not yet consider moist effects. Further, the asymptotic derivation leading to the final model reveals that the considered timescale is too short to allow for the generation of significant amounts of rain.

By assumption 2, the ideal gas law yields

$$p = \rho R T = p_\mathrm{p} = \rho_\mathrm{p} R T_\mathrm{p} \;\Rightarrow\; \rho = \frac{p}{RT}\,,\ \rho_\mathrm{p} = \frac{p}{RT_\mathrm{p}} \tag{2.25}$$

so that (2.24) can be rewritten as

$$\ddot{z}(t) = \frac{T_\mathrm{p} - T}{T} g. \tag{2.26}$$

By definition (2.6) and assumption 2,

$$\theta_\mathrm{p} = T_\mathrm{p} \left(\frac{p_0}{p}\right)^\kappa \quad , \quad \theta = T \left(\frac{p_0}{p}\right)^\kappa \tag{2.27}$$

and (2.26) becomes

$$\ddot{z}(t) = \frac{\theta_\mathrm{p} - \theta}{\theta} g. \tag{2.28}$$

Now denote by z_0 the initial height of the parcel and perform a Taylor expansion of the potential temperature distribution of the background around this height

$$\theta\left(z_0 + \delta z\right) = \theta(z_0) + \frac{\partial \theta}{\partial z} \delta z + \mathcal{O}(\delta z^2). \tag{2.29}$$

Assuming that initially the parcel has no buoyancy or equivalently that it has the same potential temperature as the environment in conjunction with assumption 1 yields $\theta(z_0) = \theta_\mathrm{p} =: \theta_0 = const.$ Inserting (2.29) into (2.28) and using that z_0 is constant, thus $\ddot{z} = \ddot{\delta z}$, yields an equation for the displacement of the parcel

$$\ddot{\delta z}(t) = -\theta_0^{-1} \frac{\partial \theta}{\partial z} g \delta z(t) + \mathcal{O}(\delta z^2). \tag{2.30}$$

If the parcel is subject to some externally forced displacement Z at time $t = 0$, to leading order the performed oscillation reads

$$z(t) = z_0 + \delta z(t) = z_0 + Z \exp\left(i \sqrt{\frac{g}{\theta_0} \frac{\partial \theta}{\partial z}} t\right). \tag{2.31}$$

Thus in a stably stratified atmosphere with $\partial\theta/\partial z > 0$ the parcel performs an oscillation around its initial height z_0 with amplitude Z and an angular frequency

$$N := \sqrt{\frac{g}{\theta_0} \frac{\partial \theta}{\partial z}}. \tag{2.32}$$

This frequency is called "stability frequency" or "Brunt-Väisälä frequency", see e.g. p. 51f. in [Gil82]. For the non-dimensional equations used in the model derivation in this thesis it turns out to be simply

$$N = \sqrt{\Theta_z^{(2)}} \tag{2.33}$$

whereas $\Theta^{(2)}$ is the background potential temperature introduced in the expansion of θ in (2.41).

Moisture can significantly affect this mechanism. Depending on the amplitude of the oscillation and the initial vapor content, the parcel might reach its lifting condensation level (LCL) during its ascend. Onsetting condensation releases latent heat, compensating for some of the adiabatic cooling the rising parcel undergoes. The cooling rate without condensation, referred to as "dry adiabatic lapse rate", is about 1 K/100 m while the cooling rate with condensation, the "moist adiabatic lapse rate", can be as small as 0.4 K/100 m, see [Ste05]. Depending on the stratification of the atmosphere, the reduced lapse rate decreases the restoring force acting on a parcel by reducing the temperature difference to the environment. This influences the oscillation of the parcel and significantly affects the dynamics of gravity waves. In a conditionally unstable atmosphere, latent heat renders the parcel's buoyancy positive, triggering moist convection.

Momentum Flux

Vertical propagation of internal gravity waves leads to a vertical flux of mean horizontal momentum. Denote by (u, w) the wave-related perturbations from a background in the velocity field. The net flux across a level $z = const.$ induced by waves reads

$$\tau_{\text{net}} = \left\langle \rho^{(0)} uw \right\rangle \tag{2.34}$$

cf. section 6.7 in [Büh09]. The parentheses $\langle \cdot \rangle$ denote the average over the horizontal wave-scale coordinate $\mathbf{x}$. τ_{net} has the dimension of force per unit area, N m^{-2}, or stress. As discussed for example in [KEC03], τ_{net} is closely related to gravity wave drag (GWD) and hence important for the parameterization of GWD in global circulation models.

2.2.2. Scales and Corresponding Coordinates

The scales characterizing the regime to be modelled are summarized in (2.35) and sketched in figure 2.1. The horizontal and vertical wave-scale of 10 km correspond to the regime of non-hydrostatic, non-rotating gravity waves specified in ch. 8 in [Gil82], see especially table 8.1. Based on measurements during GATE[1] [LZ80, Ste05] indicate a median diameter of "convective events" in tropical deep convection of 900 m, justifying the horizontal tower-scale in (2.35) of 1 km.

[1] GARP (Global Atmospheric Research Program) Atlantic Tropical Experiment

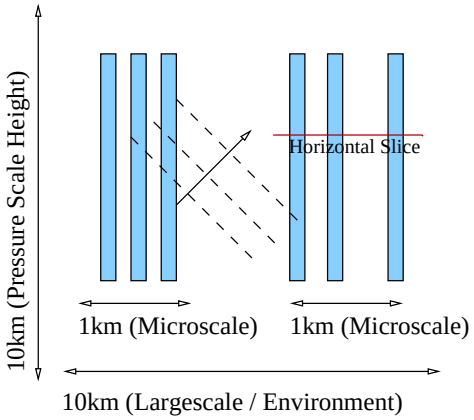

Figure 2.1.: *Scales involved in the model: Deep convective moist towers (vertical bars) extending through the depth of the h_{sc} deep troposphere with horizontal variation on a 1 km micro-scale and embedded into an order of 10 km wide environment. The dashed lines sketch the phase lines of an internal gravity wave travelling through this background. A horizontal slice through a collection of convective towers is marked, cf. figure 2.2.*

Typical flow velocity:	$u_{\mathrm{ref}} \approx 10\ \mathrm{m\ s}^{-1}$	
Vertical wave-scale:	$h_{\mathrm{sc}} \approx 10\ \mathrm{km}$	
Horizontal wave-scale:	$\mathbf{x}_{\mathrm{ref}} \approx 10\ \mathrm{km}$	(2.35)
Horizontal scale of deep convective towers:	$\eta_{\mathrm{ref}} \approx 1\ \mathrm{km}$	
Timescale of internal waves:	$\tau_{\mathrm{ref}} \approx 100\ \mathrm{s}$	

The timescale $(2.35)_5$ stems from the typical value of $N = 0.01\mathrm{s}^{-1}$ for the stability frequency in the troposphere, see p. 52 in [Gil82]. The scales in (2.35), following [KM06], are resolved by introducing suitable coordinates. $\mathbf{x}$ resolves the large 10 km horizontal scale while z resolves the vertical h_{sc} scale. To resolve the horizontal micro-physics scale $(2.35)_4$ an additional horizontal coordinate

$$\eta := \varepsilon^{-1}\mathbf{x} \tag{2.36}$$

is introduced. The coordinate t resolves a 1000 s timescale. In order to resolve τ_{ref}, the temporal coordinate is changed from t to

$$\tau := \varepsilon^{-1}t. \tag{2.37}$$

To include wave propagation as well as horizontal advection over h_{sc} distances in in the model, the ansatz for the horizontal velocity used in [KM06] is slightly

modified by introducing a constant, horizontal background velocity $\mathbf{u}^\infty$ of order $\mathcal{O}(\varepsilon^{-1})$, cf. (2.40). In order to avoid inconsistencies in the derivation, a second time-coordinate

$$\tau' := \varepsilon^{-2} t \tag{2.38}$$

resolving the timescale set by advection of flows with u^∞-velocity over η_{ref}-distances has to be introduced. All terms related to τ' drop out by sublinear growth conditions later in the derivation. Summarized, the following coordinates are employed

$$\begin{aligned} \text{Horizontal:} \quad & \mathbf{x} \quad , \quad \eta = \varepsilon^{-1}\mathbf{x} \\ \text{Vertical:} \quad & z \\ \text{Time:} \quad & \tau = \varepsilon^{-1} t \quad , \quad \tau' = \varepsilon^{-2} t. \end{aligned} \tag{2.39}$$

In principle, every coefficient in the expansions of the variables could depend on all of these coordinates. Some physically motivated restrictions are however included in the expansions presented in subsection 2.2.3, see [KM06] for details.

2.2.3. Expansions

Horizontal Velocity

The ansatz for horizontal velocity including the constant background wind $\mathbf{u}^\infty$ reads

$$\mathbf{u}(\mathbf{x}, z, t; \varepsilon) = \varepsilon^{-1}\mathbf{u}^\infty + \mathbf{u}^{(0)}(\mathbf{x}, z, \tau) + \mathcal{O}(\varepsilon). \tag{2.40}$$

Although this scaling would suggest background flows of the order of 100 m s^{-1}, a value of $u^\infty = 0.1$, corresponding to a velocity of 10 m s^{-1}, is generally used in this thesis. The justification of this apparent inconsistency between asymptotic scaling of $\mathbf{u}^\infty$ and the actual values employed for it is given in [RKM10].

Other Expansions

Expansions of vertical velocity, potential temperature, pressure and density are adopted from [KM06], but are now also allowed to depend on τ', i.e.

$$\begin{aligned} w(\mathbf{x}, z, t; \varepsilon) &= w^{(0)}(\eta, \mathbf{x}, z, \tau, \tau') + \mathcal{O}(\varepsilon) \\ \theta(\mathbf{x}, z, t; \varepsilon) &= 1 + \varepsilon^2 \Theta^{(2)}(z) + \varepsilon^3 \theta^{(3)}(\eta, \mathbf{x}, z, \tau, \tau') + \mathcal{O}(\varepsilon^4) \\ (p, \rho)(\mathbf{x}, z, t; \varepsilon) &= (p^{(0)}, \rho^{(0)})(z) + \varepsilon (p^{(1)}, \rho^{(1)})(z) + \varepsilon^2 (p^{(2)}, \rho^{(2)})(z) \\ &\quad + \varepsilon^3 (p^{(3)}, \rho^{(3)})(\eta, \mathbf{x}, z, \tau, \tau') + \mathcal{O}(\varepsilon^4). \end{aligned} \tag{2.41}$$

The mixing ratios for water vapor, cloud water and rain water are expanded as

$$q_{\text{i}} = q_{\text{i}}^{(0)}(\eta, \mathbf{x}, z, \tau, \tau') + \varepsilon q_{\text{i}}^{(1)}(\eta, \mathbf{x}, z, \tau, \tau') + \mathcal{O}(\varepsilon^2) \ , \ i = \text{v, c, r.} \tag{2.42}$$

The expansions (2.40), (2.41) and (2.42) are inserted into the non-dimensional dynamic equations (2.9) and the bulk micro-scale equations (2.14) and the leading order equations are collected. All quantities are split up into

$$\phi = \bar{\phi} + \tilde{\phi} \tag{2.43}$$

with

$$\bar{\phi}(\mathbf{x}, z, \tau) = \lim_{\eta_0 \to \infty} \frac{1}{|[-\eta_0, \eta_0]^d|} \int_{[-\eta_0, \eta_0]^d} \phi(\eta, \mathbf{x}, z, \tau)\ d\eta \tag{2.44}$$

denoting the average over η and the tilde denoting perturbations. In the two-dimensional case analyzing a x-z-plane set $d = 1$ while $d = 2$ corresponds to the full three-dimensional case. The splitting (2.43) yields a set of equations for the averages $\bar{\phi}$ and an additional set of equations for the perturbations $\tilde{\phi}$.

2.2.4. Leading Order Equations

Key steps of the derivation can be found in appendix A.1. The leading order equations for the averages read

$$\begin{aligned}
\mathbf{u}^{(0)}_\tau + \mathbf{u}^\infty \cdot \nabla_x \mathbf{u}^{(0)} + \nabla_x \pi^{(3)} &= 0 \\
\bar{w}^{(0)}_\tau + \mathbf{u}^\infty \cdot \nabla_x \bar{w}^{(0)} + \pi^{(3)}_z &= \bar{\theta}^{(3)} \\
\bar{\theta}^{(3)}_\tau + \mathbf{u}^\infty \cdot \nabla_x \bar{\theta}^{(3)} + \bar{w}^{(0)} \Theta^{(2)}_z &= \frac{\Gamma^{**} L^{**} q^{**}_{\mathrm{vs}}}{p_0} \left(\overline{H_{q_\mathrm{v}} C^{(0)}_\mathrm{d}} + \overline{(H_{q_\mathrm{v}} - 1)\, C^{(0)}_\mathrm{ev}} \right) \\
\nabla_x \cdot \left(\rho^{(0)} \mathbf{u}^{(0)} \right) + \left(\rho^{(0)} \bar{w}^{(0)} \right)_z &= 0
\end{aligned} \tag{2.45}$$

with $\pi^{(3)} = p^{(3)}/\rho^{(0)}$ and $\Theta^{(2)}_z(z)$ being the potential temperature gradient of the background. H_{q_v} is a switching function, distinguishing between leading-order saturated and non-saturated regions

$$H_{q_v}(q_v) = \begin{cases} 1 & : \quad q^{(0)}_\mathrm{v} \geq q^{(0)}_\mathrm{vs} \quad \text{(saturation)} \\ 0 & : \quad q^{(0)}_\mathrm{v} < q^{(0)}_\mathrm{vs} \quad \text{(non-saturation)} \end{cases} . \tag{2.46}$$

The equations for the perturbations $\tilde{w}^{(0)}$ and $\tilde{\theta}^{(3)}$ read

$$\begin{aligned}
\tilde{w}^{(0)}_\tau + \mathbf{u}^\infty \cdot \nabla_x \tilde{w}^{(0)} + \mathbf{u}^{(0)} \cdot \nabla_\eta \tilde{w} &= \tilde{\theta}^{(3)} \\
\tilde{\theta}^{(3)}_\tau + \mathbf{u}^\infty \cdot \nabla_x \tilde{\theta}^{(3)} + \mathbf{u}^{(0)} \cdot \nabla_\eta \tilde{\theta}^{(3)} + \tilde{w}^{(0)} \Theta^{(2)}_z &= \\
\frac{\Gamma^{**} L^{**} q^{**}_{\mathrm{vs}}}{p_0} \left(H_{q_v} C^{(0)}_\mathrm{d} - \overline{H_{q_v} C^{(0)}_\mathrm{d}} + (H_{q_v} - 1)\, C^{(0)}_\mathrm{ev} - \overline{(H_{q_v} - 1)\, C^{(0)}_\mathrm{ev}} \right) .
\end{aligned} \tag{2.47}$$

To obtain a closed system for the wave-scale coordinates, expressions for the averaged source terms $\overline{H_{q_\mathrm{v}} C^{(0)}_\mathrm{d}}$ and $\overline{(H_{q_\mathrm{v}} - 1)\, C^{(0)}_\mathrm{ev}}$ in $(2.45)_3$ are derived in subsection

2.2.5 from (2.47) and the leading order equations arising from the bulk microphysics model (2.14).

As explained in A.1 two different regimes can be distinguished with respect to the leading order equations emerging from the micro-physical model:

Saturation In the regime of leading order saturation, i.e. $H_{\mathrm{q_v}} = 1$, the leading order equations emerging from (2.14) are

$$\begin{aligned} -\left(\bar{w}^{(0)} + \tilde{w}^{(0)}\right) q_{\mathrm{vs,z}}^{(0)} &= C_{\mathrm{d}}^{(0)} \\ q_{\mathrm{r},\tau}^{(0)} + \mathbf{u}^{\infty} \cdot \nabla_x q_{\mathrm{r}}^{(0)} + \mathbf{u}^{(0)} \cdot \nabla_\eta q_{\mathrm{r}}^{(0)} &= 0. \end{aligned} \tag{2.48}$$

Non-saturation In regions that are not saturated at leading order, i.e. $H_{\mathrm{q_v}} = 0$, the leading order equations obtained from (2.14) read

$$\begin{aligned} C_{\mathrm{ev}}^{**}\left(q_{\mathrm{vs}}^{(0)} - q_{\mathrm{v}}^{(0)}\right)\sqrt{q_{\mathrm{r}}^{(0)}} &= C_{\mathrm{ev}}^{(0)} \\ q_{\mathrm{v},\tau}^{(0)} + \mathbf{u}^{\infty} \cdot \nabla_x q_{\mathrm{v}}^{(0)} + \mathbf{u}^{(0)} \cdot \nabla_\eta q_{\mathrm{v}}^{(0)} &= 0 \\ q_{\mathrm{r},\tau}^{(0)} + \mathbf{u}^{\infty} \cdot \nabla_x q_{\mathrm{r}}^{(0)} + \mathbf{u}^{(0)} \cdot \nabla_\eta q_{\mathrm{r}}^{(0)} &= 0. \end{aligned} \tag{2.49}$$

As in [KM06] the cloud water mixing ratio is systematically small and $q_{\mathrm{c}}^{(0)} \equiv 0$ obtains in both regimes.

2.2.5. Closing the Model

Below, using (2.45), (2.47) (2.48) and (2.49), a closed set of equations depending only on the wave-scale related coordinates $\mathbf{x}$, z τ but still including the net effects from the micro-scale moist processes is derived analytically.

As discussed in [KM06], typical atmospheric values of convective available potential energy (CAPE) constrain the possible deviation of θ from a moist adiabat. In an atmosphere where deep convection can extend over heights comparable to h_{sc}, the order of magnitude of CAPE can be estimated by

$$\mathrm{CAPE}^{*} \sim g h_{\mathrm{sc}} \frac{\Delta T_{\mathrm{v}}}{T_{\mathrm{v,env}}} \tag{2.50}$$

whereas ΔT_{v} denotes deviations of virtual temperature from a moist adiabatic environment. According to [Ema94] typical dimensional values for CAPE are of the order 400 $\mathrm{m^2\ s^{-2}}$. For $T_{\mathrm{v,env}} \sim 300$ K, (2.50) yields an estimate

$$\Delta T_{\mathrm{v}}^{*} \sim \frac{400\ \mathrm{m^2\ s^{-2}} \cdot 300\ \mathrm{K}}{10^4\ \mathrm{m} \cdot 10\ \mathrm{m\ s^{-2}}} \sim 1.2\ \mathrm{K}. \tag{2.51}$$

This is in line with values $\Delta T_{\mathrm{v}} \sim 0.5$ K indicated by [Ste05].

In non-dimensional terms (2.51) becomes

$$\Delta T_{\mathrm{v}} \sim \frac{\Delta T_{\mathrm{v}}^*}{300\ \mathrm{K}} \sim 4 \cdot 10^{-3} \sim \mathcal{O}(\varepsilon^3). \tag{2.52}$$

Thus deviations from a moist-neutral stratification can arise only at $\theta^{(3)}$ or higher orders and $\Theta^{(2)}$ satisfies the moist adiabatic equation

$$\Theta_z^{(2)} = -\frac{\Gamma^{**} L^{**} q_{\mathrm{vs}}^{**}}{p^{(0)}} q_{\mathrm{vs},z}^{(0)} \tag{2.53}$$

cf. [KM06]. Hence the model describes small, asymptotic variations of potential temperature around a moist adiabatic background. See appendix A.2 for a brief comment on relaxing this assumption. Note that the leading order in the expansion of θ is equal to unity, corresponding to constant potential temperature with height, i.e. a dry adiabatic stratification. The $\mathcal{O}(\varepsilon^2)$ term provides an additional contribution, resulting in an overall moist adiabatic stratification and $\theta^{(3)}$ denotes perturbations from this background, determining buoyancy.

Abbreviate

$$\hat{L} := \frac{\Gamma^{**} L^{**} q_{\mathrm{vs}}^{**}}{p^{(0)}} \tag{2.54}$$

and multiply $(2.48)_1$ by $H_{q_{\mathrm{v}}}$ and use (2.53) to obtain

$$H_{\mathrm{q_v}} \left(\bar{w}^{(0)} + \tilde{w}^{(0)} \right) \frac{1}{\hat{L}} \Theta_z^{(2)} = H_{\mathrm{q_v}} C_{\mathrm{d}}^{(0)}. \tag{2.55}$$

Averaging over η yields

$$\overline{H_{q_{\mathrm{v}}}} \bar{w}^{(0)} \Theta_z^{(2)} + \overline{\left(H_{q_{\mathrm{v}}} \tilde{w}^{(0)} \right)} \Theta_z^{(2)} = \hat{L} \overline{H_{q_{\mathrm{v}}} C_{\mathrm{d}}^{(0)}}. \tag{2.56}$$

According to $(2.49)_2$, $q_{\mathrm{v}}^{(0)}$ is simply advected by the large- and small-scale flow in non-saturated regions. In the saturated regime $q_{\mathrm{v}}^{(0)} = q_{\mathrm{vs}}^{(0)}(z)$ trivially satisfies the same advection equation. Thus the solution for $q_{\mathrm{v}}^{(0)}$ is completely determined by its initial distribution and reads

$$q_{\mathrm{v}}^{(0)}(\mathbf{x}, z, \eta, \tau) = q_{\mathrm{v}}^{(0)}(\mathbf{x} - \mathbf{u}^{\infty}\tau, z, \eta - \int_0^{\tau} \mathbf{u}^{(0)}(\mathbf{x}, z, t')\ dt', 0). \tag{2.57}$$

Define

$$\sigma(\mathbf{x}, z, \tau) := \overline{H_{\mathrm{q_v}}(\mathbf{x}, z, \eta, \tau)}. \tag{2.58}$$

It turns out that σ is the essential moisture-related parameter in the model, see subsection 2.2.7 for a discussion. As $\int_0^{\tau} \mathbf{u}^{(0)}(\mathbf{x}, z, t')\ dt'$ is independent of η, (2.57) and (2.58) yield

$$\begin{aligned}\sigma(\mathbf{x},z,\tau) &= \overline{H_{\mathrm{q_v}}(\mathbf{x},z,\eta,\tau)} \\ &= \overline{H_{\mathrm{q_v}}(\mathbf{x}-\mathbf{u}^{\infty}\tau,z,\eta-\int_0^{\tau}\mathbf{u}^{(0)}(\mathbf{x},z,t')\;dt',0)} \\ &= \sigma(\mathbf{x}-\mathbf{u}^{\infty}\tau,z,0).\end{aligned} \tag{2.59}$$

By using (2.58), equation (2.56) can be rewritten as

$$\sigma\bar{w}^{(0)}\Theta_z^{(2)} + \overline{\left(H_{q_\mathrm{v}}\tilde{w}^{(0)}\right)}\Theta_z^{(2)} = \hat{L}\overline{H_{q_\mathrm{v}}C_{\mathrm{d}}^{(0)}}. \tag{2.60}$$

To evaluate (2.60), an equation for the conditionally averaged perturbation

$$w' := \overline{H_{\mathrm{q_v}}\tilde{w}^{(0)}} \tag{2.61}$$

is required. Multiply (2.47) by $H_{\mathrm{q_v}}$ and average again over η. Note that as q_v satisfies $(\partial_\tau + \mathbf{u}^{\infty}\cdot\nabla_x)\,q_\mathrm{v} = 0$, the order of averaging and differentiating can be reversed, i.e.

$$\left(\overline{H_{\mathrm{q_v}}\tilde{w}_\tau}\right) + \mathbf{u}^{\infty}\cdot\left(\overline{H_{\mathrm{q_v}}\nabla_x\tilde{w}}\right) = \left(\overline{H_{\mathrm{q_v}}\tilde{w}}\right)_\tau + \mathbf{u}^{\infty}\cdot\nabla_x\left(\overline{H_{\mathrm{q_v}}\tilde{w}}\right). \tag{2.62}$$

Using $H_{q_\mathrm{v}}^2 = H_{q_\mathrm{v}}$, $H_{q_\mathrm{v}}\,(H_{q_\mathrm{v}}-1) = 0$ and setting

$$\theta' := \overline{H_{\mathrm{q_v}}\tilde{\theta}} \tag{2.63}$$

yields

$$\begin{aligned} w'_\tau + \mathbf{u}^{\infty}\cdot\nabla_x w' &= \theta' \\ \theta'_\tau + \mathbf{u}^{\infty}\cdot\nabla_x\theta' + w'\Theta_z^{(2)} &= \hat{L}\overline{\left[H_{q_\mathrm{v}}C_{\mathrm{d}}^{(0)} - H_{q_\mathrm{v}}\overline{H_{\mathrm{q_v}}\tilde{C}^{(0)}}\right]} \\ &\quad - \hat{L}\overline{\left[H_{q_\mathrm{v}}\overline{(H_{q_\mathrm{v}}-1)\,C_{\mathrm{ev}}^{(0)}}\right]}. \end{aligned} \tag{2.64}$$

Further computation of the source term, using (2.60) and definition (2.58), yields

$$\begin{aligned} &\hat{L}\overline{\left[H_{q_\mathrm{v}}C_{\mathrm{d}}^{(0)} - H_{q_\mathrm{v}}\overline{H_{\mathrm{q_v}}\tilde{C}^{(0)}} - H_{q_\mathrm{v}}\left[\overline{(H_{q_\mathrm{v}}-1)\,C_{\mathrm{ev}}^{(0)}}\right]\right]} \\ &= \hat{L}\overline{H_{q_\mathrm{v}}C_{\mathrm{d}}^{(0)}} - \sigma\hat{L}\overline{H_{q_\mathrm{v}}C_{\mathrm{d}}^{(0)}} - \sigma\hat{L}\left[\overline{(H_{q_\mathrm{v}}-1)\,C_{\mathrm{ev}}^{(0)}}\right] \\ &= (1-\sigma)\left(\sigma\bar{w}^{(0)}\Theta_z^{(2)} + w'\Theta_z^{(2)}\right) - \sigma\bar{C}_- \\ &= (1-\sigma)\,\sigma\bar{w}^{(0)}\Theta_z^{(2)} + (1-\sigma)\,w'\Theta_z^{(2)} - \sigma\bar{C}_- \end{aligned} \tag{2.65}$$

with

$$\begin{aligned}\bar{C}_- &:= \hat{L}\left[\overline{(H_{q_\mathrm{v}}-1)\,C_{\mathrm{ev}}^{(0)}}\right] \\ &= \hat{L}C_{\mathrm{ev}}^{**}\overline{(H_{\mathrm{q_v}}-1)\left(q_{\mathrm{vs}}^{(0)}-q_{\mathrm{v}}^{(0)}\right)\sqrt{q_{\mathrm{r}}^{(0)}}}\end{aligned} \tag{2.66}$$

using (2.49). Inserting this into $(2.64)_2$ results in

$$\begin{aligned} w'_\tau + \mathbf{u}^\infty \cdot \nabla_x w' &= \theta' \\ \theta'_\tau + \mathbf{u}^\infty \cdot \nabla_x \theta' + \sigma \Theta_z^{(2)} w' &= \sigma\,(1-\sigma)\,\bar{w}^{(0)} \Theta_z^{(2)} - \sigma \bar{C}_-. \end{aligned} \tag{2.67}$$

Finally, using (2.60) and (2.66), $(2.45)_3$ can be written as

$$\bar{\theta}^{(3)}_\tau + \mathbf{u}^\infty \cdot \nabla_x \bar{\theta}^{(3)} + (1-\sigma)\,\Theta_z^{(2)} \bar{w}^{(0)} = \Theta_z^{(2)} w' + \bar{C}_-. \tag{2.68}$$

Note that in non-saturated regions with $H_{\mathrm{q_v}} = 0$, the saturation deficit $q_{\mathrm{vs}}^{(0)} - q_{\mathrm{v}}^{(0)}$ in (2.66) is greater than zero . Further, $\hat{L}$, C_{ev}^{**} and $q_{\mathrm{r}}^{(0)}$ are also positive, so that

$$\bar{C}_- \leq 0 \tag{2.69}$$

constitutes a negative source term in (2.68) representing the net effect of evaporative cooling in non-saturated areas. The equations (2.48) and (2.49) indicate that $q_{\mathrm{r}}^{(0)}$, just as $q_{\mathrm{v}}^{(0)}$, is only advected by the flow so that $\bar{C}_-$ can be obtained by suitable horizontal translations of its initial distribution $\bar{C}_-(\tau = 0)$, analogously to (2.59).

2.2.6. Summary of the Model

The complete, closed model consists of the equations $(2.45)_{1,2}$ for $\mathbf{u}^{(0)}$ and $\bar{w}^{(0)}$ plus the anelastic constraint $(2.45)_4$, equation (2.68) for the large-scale potential temperature, and the averaged bulk micro-scale equations (2.67) providing the closure for the moisture-related source term in (2.68).

Linearized, anelastic moist dynamics:

$$\begin{aligned} \mathbf{u}_\tau + \mathbf{u}^\infty \cdot \nabla_x \mathbf{u} + \nabla_x \pi &= 0 \\ \bar{w}_\tau + \mathbf{u}^\infty \cdot \nabla_x \bar{w} + \pi_z &= \bar{\theta} \\ \bar{\theta}_\tau + \mathbf{u}^\infty \cdot \nabla_x \bar{\theta} + (1-\sigma)\,\Theta_z^{(2)} \bar{w} &= \Theta_z^{(2)} w' + \bar{C}_- \\ \nabla_x \cdot \left(\rho^{(0)} \mathbf{u}\right) + \left(\rho^{(0)} \bar{w}\right)_z &= 0 \end{aligned} \tag{2.70}$$

Averaged tower-scale dynamics:

$$\begin{aligned} w'_\tau + \mathbf{u}^\infty \cdot \nabla_x w' &= \theta' \\ \theta'_\tau + \mathbf{u}^\infty \cdot \nabla_x \theta' + \sigma \Theta_z^{(2)} w' &= \sigma\,(1-\sigma)\,\Theta_z^{(2)} \bar{w} - \sigma \bar{C}_-. \end{aligned}$$

The superscripts 0 and 3 are dropped for the purpose of simplified notation.

If all micro-scale related terms vanish, i.e.

$$\sigma = 0\ ,\ \bar{C}_- = 0 \quad \text{and} \quad w'(\tau = 0) = \theta'(\tau = 0) = 0, \tag{2.71}$$

(2.70) reduces to

$$\begin{aligned} \mathbf{u}_\tau + \mathbf{u}^\infty \cdot \nabla_x \mathbf{u} + \nabla_x \pi &= 0 \\ \bar{w}_\tau + \mathbf{u}^\infty \cdot \nabla_x \bar{w} + \pi_z &= \bar{\theta} \\ \bar{\theta}_\tau + \mathbf{u}^\infty \cdot \nabla_x \bar{\theta} + \Theta_z^{(2)} \bar{w} &= 0 \\ \nabla_x \cdot \left(\rho^{(0)} \bar{u} \right) + \left(\rho^{(0)} \bar{w} \right)_z &= 0 \end{aligned} \tag{2.72}$$

which are the well-known anelastic equations linearized around a background velocity $(\mathbf{u}^\infty, 0)$ and a background stratification $\Theta_z^{(2)}$ and analyzed, for example, in [DSWT03]. Comparing (2.72) and (2.70) reveals that moisture modifies (2.72) in several ways:

1. The effective stability is reduced from $\Theta_z^{(2)}$ to $N_{\text{eff}}^2 = (1-\sigma)\,\Theta_z^{(2)}$. A reduction of stability by moisture is also indicated e.g. in [EL73a, DK82]. An explicit switching mechanism between a background stability in non-saturated regions and a reduced moist stability inside clouds to capture the effect of moisture on wave-scale dynamics is employed in [BJD79, BJB80, JB85]. In (2.70), the reduced effective stability arises naturally from the asymptotic approach.

2. A source term $\Theta_z^{(2)} w'$ for the large-scale potential temperature arises, describing the net latent heat release or consumption due to micro-scale processes. This source term is determined by two additional prognostic equations for the weighted averages w' and θ'. As the large-scale vertical velocity $\bar{w}$ occurs in the right hand side of $(2.70)_6$, there is actually a bi-directional coupling between large-scale and averaged tower-scale dynamics.

3. The evaporation of rain in non-saturated regions results in a constant cooling, described by the source term $\bar{C}_-$. On the considered scales, this cooling term is constant in time.

2.2.7. Saturated Area Fraction

By definition (2.46), the switching function H_{q_v} is the characteristic function of leading-order saturated areas. Definition (2.44) yields

$$\begin{aligned} \sigma(\mathbf{x}, z, \tau) &= \lim_{\eta_0 \to \infty} \frac{1}{\left| [-\eta_0, \eta_0]^d \right|} \int_{[-\eta_0, \eta_0]^d} H_{\text{q}_\text{v}}(\mathbf{x}, z, \eta', \tau)\, d\eta' \\ &= \lim_{\eta_0 \to \infty} \frac{\left| \{ \eta \in (-\eta_0, \eta_0)^d : q_\text{v}^{(0)}(\mathbf{x}, z, \eta, \tau) \geq q_{\text{vs}}^{(0)}(z) \} \right|}{\left| [-\eta_0, \eta_0]^d \right|}. \end{aligned} \tag{2.73}$$

Hence for a fixed point $(\mathbf{x}, z, \tau)$, σ indicates the area fraction of saturated regions

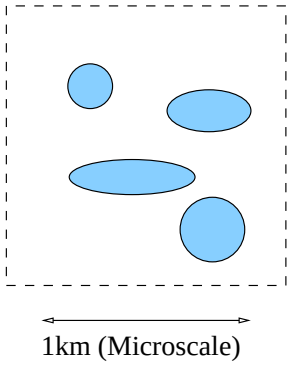

Figure 2.2.: *Sketched downward view on a horizontal slice through a group of deep convective towers, cf. figure 2.1. Colored regions indicate cuts through clouds.*

on the η-scale. In figure 2.1 a horizontal slice through a group of deep convective towers is marked. Figure 2.2 shows an example of a downward view onto such a slice. Colored areas denote cuts through clouds. According to e.g. [Tom02], in warm clouds without ice phase no significant over-saturations occur and cloudy and saturated regions essentially coincide. Hence σ is also the area fraction of cloudy (=colored) regions. Thus for $\sigma = 1$ the whole square is filled while $\sigma = 0$ corresponds to no colored regions at all, i.e. all-over non-saturated air.

The scales in (2.35) result in dimensional vertical displacements in the model of order

$$\xi_{\text{dim}} \sim w_{\text{ref}} \cdot \tau_{\text{ref}} \approx 1000\text{m} \approx \varepsilon h_{\text{sc}}. \tag{2.74}$$

As h_{sc} is the vertical lengthscale, the non-dimensionalized displacement is of order

$$\xi \sim \mathcal{O}(\varepsilon). \tag{2.75}$$

Because $z \sim \mathcal{O}(1)$ and $q_{\text{vs}} \sim \mathcal{O}(1)$, the amount of cloud water evaporating into vapor or vapor condensating into cloud water is of order

$$q \sim \frac{dq_{\text{vs}}}{dz}\xi \sim \mathcal{O}(\varepsilon). \tag{2.76}$$

If a saturation deficit at leading order is present initially, i.e.

$$\delta q_{\text{vs}} \sim \mathcal{O}(1), \tag{2.77}$$

no leading order effect on δq_{vs} can be induced by (2.76). For this reason, on the employed 100 s timescale, vertical displacements of a parcel can neither evaporate enough cloud water in saturated areas nor condensate enough vapor in non-saturated areas to affect $\delta q_{\text{vs}}^{(0)}$ and influence the size of saturated areas at leading order. Thus σ is constant over time in the derived model, satisfying (2.59). This regime is sketched in the left graphic in figure 2.3. Shown is an example distribu-

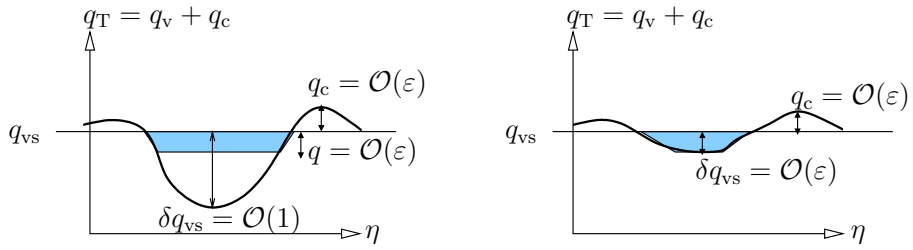

Figure 2.3.: Left: *Leading order saturation deficit.* Right: *Small saturation deficit. Shown is an example distribution of the amount of total water* $q_\mathrm{T} = q_\mathrm{v} + q_\mathrm{c}$. *The horizontal line indicates the saturation mixing ratio* q_vs. *As the leading order cloud water mixing ratio* $q_\mathrm{c}^{(0)}$ *is zero in both regimes, the surplus* $q_\mathrm{T} - q_\mathrm{vs}$ *is of order* $\mathcal{O}(\varepsilon)$ *in saturated regions. The colored area indicates the* $q \sim \mathcal{O}(\varepsilon)$ *amount of condensate released on the employed timescale by vertical displacement.*

tion of the sum $q_\mathrm{T} = q_\mathrm{v} + q_\mathrm{c}$ of water vapor and cloud water mixing ratio. The horizontal line is the saturation mixing ratio q_vs. As cloud water is systematically small, i.e. $q_\mathrm{c}^{(0)} = 0$, the surplus $q_\mathrm{T} - q_\mathrm{vs}$ is of order $\mathcal{O}(\varepsilon)$ in saturated regions. The colored area indicates the small amount $q = \mathcal{O}(\varepsilon)$ released by vertical displacements on the considered scales for time and vertical velocity. In the left figure, the saturation deficit is of order unity, so the released condensate can not change the area of saturated regions at leading order.

The situation is different if the saturation deficit is assumed to be of higher order, i.e.

$$\delta q_\mathrm{vs} \sim \mathcal{O}(\varepsilon) \tag{2.78}$$

equivalent to assuming leading order saturation $q_\mathrm{v}^{(0)} = q_\mathrm{vs}^{(0)}$ beforehand. The right graphic in figure 2.3 sketches this. Although the amount of released condensate is still small, because of the likewise small saturation deficit changes in the area of saturated regions are now of order $\mathcal{O}(1)$ and the scaling (2.76) suffices to affect the size of non-saturated/saturated regions at leading order and σ is no longer a constant but becomes a prognostic quantity, too. The extension of the model to this regime is discussed in detail in chapter 6.

Cloud Cover Fraction

A problem encountered commonly in the development of GCMs is that the average relative humidity in a grid-cell with boundaries featuring a length of the order of 100 km is not sufficient to reasonably represent cloud patterns inside the cell. Because clouds extending over the full size of a cell are uncommon, the average relative humidity for the entire cell is usually less then 100% and the whole cell would have to be considered cloud-free, leading to massive underestimation of

cloudiness and thus a severe ill-treatment of cloud related quantities like cloud albedo. For this reason, all GCMs compute some form of cloud cover fraction parameter inside each cell, indicating in some sense the area fraction of clouds, see [Tom02, JK99, Jak99] and citations therein. The cloud cover fraction parameter is reminiscent of σ, but with the average computed over a finite GCM grid-cell and without an explicit separation of the micro-scale from the grid-cell scale.

One "future issue" in the field of gravity wave parameterizations pointed out in the review of [KEC03] is to investigate how moisture affects the wave drag produced by orographic waves. Developing ways to connect σ to the cloud fraction in a GCM and subsequently devising a modified wave drag parameterization based on (2.70) that includes the influence of moisture on momentum transport could be an interesting approach to tackle this problem. In principal, a suitably simplified version of (2.70) could also be used in a super-parameterization approach, analogously to [KR01], who embed a full two-dimensional cloud resolving model (CRM) in every grid-cell to parameterize cloud fraction and other moisture-related quantities. Although the massive computational cost most likely prohibits using such an approach in an operational GCM, it might still be useful for analytic purposes. However, this issue is not pursued further in this thesis, but mentioned as a possible direction for future research, utilizing its results.

Chapter 3.

Analytical Properties

This chapter presents an investigation of some analytical properties of the model (2.70). The influence of the micro-scale equations on different quantities is analyzed in section 3.1. A description of the model's dynamics in terms of energy is presented in section 3.2. Section 3.3 investigates how σ influences the characteristics of plane wave solutions. Among other things, the dispersion relation, the group velocity and a Taylor-Goldstein equation are derived. Section 3.4 discusses a particular simplified type of analytically obtained solutions for the case of constant coefficients. Finally, section 3.5 demonstrates that σ can cause critical layers and presents qualitative approximate solutions in their vicinity.

Because all numerical examples shown and analyzed below employ two-dimensional domains in a x-z-slice, this chapter also focusses on the two-dimensional case with one horizontal and one vertical coordinate. Thus the vector quantities $\mathbf{u}$, $\mathbf{u}^\infty$, η and $\mathbf{x}$ become scalars and are denoted as u^∞, u, η and x, while the horizontal gradient ∇_x becomes ∂_x. However, the analytical results presented in this chapter do not rely explicitly on 2-D specific properties, although calculations become simplified, hence the findings can potentially also be confirmed in an analysis of the three-dimensional system.

To streamline notation, the partial derivative with respect to time and the advective term are combined into the linearized material derivative and denoted

$$\frac{D}{D\tau} = \partial_\tau + u^\infty \partial_x. \tag{3.1}$$

3.1. Micro-Scale Dynamics

3.1.1. Constrains on Initial Data

By definition, $\sigma = 0$ equals

$$\lim_{\eta_0 \to \infty} \frac{1}{2\eta_0} \int_{-\eta_0}^{\eta_0} H_{\mathrm{q_v}} \, d\eta = 0. \tag{3.2}$$

Assuming that $\tilde{w}$ is bounded in η and using the mean value theorem for integration yields

$$\begin{aligned} w' &= \lim_{\eta_0 \to \infty} \frac{1}{2\eta_0} \int_{-\eta_0}^{\eta_0} H_{\mathrm{q_v}} \tilde{w} \, d\eta \\ &= \lim_{\eta_0 \to \infty} \frac{1}{2\eta_0} \tilde{w}(\zeta(\eta_0)) \int_{-\eta_0}^{\eta_0} H_{\mathrm{q_v}} \, d\eta \\ &= 0. \end{aligned} \tag{3.3}$$

Thus if the area fraction of saturated regions is zero, the tower-scale vertical velocity must also vanish. An identical argument yields $\theta' = 0$.

On the other hand, $\sigma = 1$ equals

$$H_{\mathrm{q_v}} = 1 \text{ almost everywhere.} \tag{3.4}$$

Thus

$$\begin{aligned} w' &= \lim_{\eta_0 \to \infty} \frac{1}{2\eta_0} \int_{-\eta_0}^{\eta_0} H_{\mathrm{q_v}} \tilde{w} \, d\eta \\ &= \lim_{\eta_0 \to \infty} \frac{1}{2\eta_0} \int_{-\eta_0}^{\eta_0} \tilde{w} \, d\eta \\ &= \overline{\tilde{w}} = 0, \end{aligned} \tag{3.5}$$

hence for the case of all-over saturated air, there is also no non-zero tower-scale vertical velocity possible. Again, $\theta' = 0$ can be concluded accordingly.

Although the initial value problem (2.70) mathematically allows for non-zero initial values w' and θ' together with $\sigma = 0$ or $\sigma = 1$, this is not consistent with the definition of the tower-scale quantities in the derivation of the model and no physically meaningful solutions can be expected.

3.1.2. Conserved Quantity

Multiplying $(2.70)_3$ with σ and adding $(2.70)_6$ yields

$$\sigma \frac{D\bar{\theta}}{D\tau} + \frac{D\theta'}{D\tau} = \frac{D}{D\tau} \left(\sigma\bar{\theta} + \theta' \right) = 0. \tag{3.6}$$

Thus $\sigma\bar{\theta} + \theta'$ is constant and one can define

$$\theta_0 := \sigma\bar{\theta} + \theta' \big|_{\tau=0} = \sigma\bar{\theta} + \theta'. \tag{3.7}$$

Using (2.58) and (2.63), θ_0 can be expressed as

$$\theta_0 = \sigma\bar{\theta} + \theta' = \overline{H_{\mathrm{q_v}}}\bar{\theta} + \overline{H_{\mathrm{q_v}}\tilde{\theta}} = \overline{H_{\mathrm{q_v}} \left(\bar{\theta} + \tilde{\theta} \right)} = \overline{H_{\mathrm{q_v}} \theta} \tag{3.8}$$

showing that the average over the total potential temperature inside convective towers is constant in time.

3.1.3. Displacement in Non-Saturated Areas

In non-saturated regions with $H_{\mathrm{q_v}} = 0$, the leading order equations for the micro-scale perturbations (2.47) simplify to

$$\begin{aligned} \frac{D\tilde{w}^{(0)}}{D\tau} + u^{(0)}\tilde{w}_\eta &= \tilde{\theta}^{(3)} \\ \frac{D\tilde{\theta}^{(3)}}{D\tau} + u^{(0)}\tilde{\theta}^{(3)}_\eta + \tilde{w}^{(0)}\Theta^{(2)}_z &= -\hat{L}\overline{H_{\mathrm{q_v}} C^{(0)}_{\mathrm{d}}} \end{aligned} \tag{3.9}$$

if rain is absent, i.e. $q^{(0)}_{\mathrm{r}} = 0$, thus $C^{(0)}_{\mathrm{ev}} = 0$ and employing (2.54). If the initial data for $\tilde{w}^{(0)}$ and $\tilde{\theta}^{(3)}$ are constant on the η scale in non-saturated regions, i.e.

$$\nabla_\eta \tilde{w}^{(0)}(\tau = 0, \eta) = \nabla_\eta \tilde{\theta}^{(3)}(\tau = 0, \eta) = 0 \quad \text{if} \quad H_{\mathrm{q_v}}(\eta) = 0, \tag{3.10}$$

equation (3.9) further simplifies to

$$\begin{aligned} \frac{D\tilde{w}^{(0)}}{D\tau} + u^{\infty}\tilde{w}^{(0)}_x &= \tilde{\theta}^{(3)} \\ \frac{D\tilde{\theta}^{(3)}}{D\tau} + u^{\infty}\tilde{\theta}^{(3)}_x + \tilde{w}^{(0)}\Theta^{(2)}_z &= -\hat{L}\overline{H_{\mathrm{q_v}} C^{(0)}_{\mathrm{d}}}. \end{aligned} \tag{3.11}$$

Because the averaged source term on the right hand side of $(3.11)_2$ is constant in η, if (3.10) holds at $\tau = 0$ it holds for all $\tau > 0$. Thus the perturbations $\tilde{w}^{(0)}$ and $\tilde{\theta}^{(3)}$ only vary inside the saturated, convective towers but are constant between them, see figure 3.1.

Assuming that the limits in the indefinite integrals can be arbitrarily exchanged, the constant value $\tilde{w}_{\mathrm{us}}$ in the non-saturated regions can be computed from the large-scale averages defined in (2.44) by

$$\begin{aligned} \tilde{w}_{\mathrm{us}} = \frac{\int_{-\infty}^{\infty}(1 - H_{\mathrm{q_v}})\,\tilde{w}^{(0)} d\eta}{\int_{-\infty}^{\infty}(1 - H_{\mathrm{q_v}})\,d\eta} &= \frac{\int_{-\infty}^{\infty}(1 - H_{\mathrm{q_v}})\,\tilde{w}^{(0)} d\eta}{\int_{-\infty}^{\infty} d\eta} \frac{\int_{-\infty}^{\infty} d\eta}{\int_{-\infty}^{\infty}(1 - H_{\mathrm{q_v}})\,d\eta} \\ &= \left(\bar{\tilde{w}}^{(0)} - w'\right)\frac{1}{1-\sigma} \\ &= -w'\frac{1}{1-\sigma}. \end{aligned} \tag{3.12}$$

Net updrafts inside the convective towers, i.e. $w' > 0$, produce a homogeneous downdraft $\tilde{w}_{\mathrm{us}} < 0$ in the non-saturated regions between them. The vertical

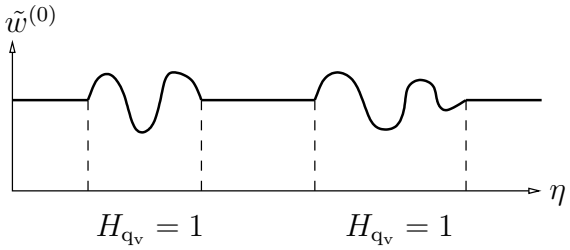

Figure 3.1.: *General shape of $\tilde{w}^{(0)}$: Variations occur only inside saturated, convective towers where $H_{\mathrm{q_v}} = 1$ while $\tilde{w}^{(0)}$ is constant outside of towers.*

displacement ξ_{us} in non-saturated regions and, by continuity, also at the interface between saturation and non-saturation satisfies

$$\frac{D\xi_{\mathrm{us}}}{D\tau} = \bar{w} + \tilde{w}_{\mathrm{us}} = \bar{w} - \frac{w'}{1-\sigma}. \tag{3.13}$$

From $(2.70)_3$ with $\bar{C}_- = 0$ it follows that

$$\frac{1}{(1-\sigma)\,\Theta_z^{(2)}}\frac{D\bar{\theta}}{D\tau} = -\left(\bar{w} - \frac{w'}{1-\sigma}\right) = -\frac{D\xi_{\mathrm{us}}}{D\tau}. \tag{3.14}$$

Hence, in the absence of evaporating rain, the displacement ξ_{us} depends solely on the large-scale potential temperature

$$\xi_{\mathrm{us}} = -\frac{\bar{\theta}}{(1-\sigma)\,\Theta_z^{(2)}}. \tag{3.15}$$

This is consistent with the formula for the dry case derived in [Büh09], section 6.2, with N^2 replaced by the effective stability $N^2_{\mathrm{eff}} = (1-\sigma)\,\Theta_z^{(2)}$. For fixed $\bar{\theta}$, the displacement ξ_{us} becomes larger if σ increases. Thus (3.15) indicates that moisture, by reducing stability, amplifies displacements generated by buoyancy.

Then again, (3.7) indicates that $\theta_0 = \sigma\bar{\theta} + \theta'$ is conserved, so depending on the evolution of θ', increasing σ can also reduce $\bar{\theta}$, thus inducing a decreasing tendency for ξ_{us}. The example presented in subsection 3.3.2 however shows an increase of ξ_{us} for increasing σ.

3.1.4. Pseudo-Momentum

As explained in [Büh09], zonal pseudo-momentum is a central quantity in the study of interaction between wave- and mean-flows, see especially p. 129f. In the following, it is shown how σ affects pseudo-momentum in the presented model. The problem of parameterizing wave drag basically comprises capturing the effect

of waves on the mid-atmospheric mean flow, cf. subsection 7.2.7 in [Büh09]. Hence the following derivations might also be useful in further work on this subject.

The vorticity of the large-scale flow reads

$$q := u_z - \bar{w}_x. \tag{3.16}$$

Applying ∂_z to $(2.70)_1$, ∂_x to $(2.70)_2$ and subtracting yields

$$\frac{Dq}{D\tau} = -\bar{\theta}_x. \tag{3.17}$$

By using (3.15) this can be transformed into

$$\frac{Dq}{D\tau} = -\bar{\theta}_x = (1-\sigma)\,\Theta_z^{(2)}\xi_{\mathrm{us},x} - \sigma_x\Theta_z^{(2)}\xi_{\mathrm{us}}. \tag{3.18}$$

The first term describes generation of vorticity by horizontal variations in the vertical displacement as discussed in section 6.2 in [Büh09] for the incompressible, dry case with the stability N^2 replaced by the effective stability $(1-\sigma)\,\Theta_z^{(2)}$. The second term describes a new mechanism where vorticity is generated by an inhomogeneous zonal distribution of moisture, even in situations with homogeneous vertical displacement.

Analogously to the derivations in section 6.3 for unsheared and in section 7.1 for sheared background flow in [Büh09], the Eulerian pseudo-momentum is derived by multiplying (3.17) by $\bar{\theta}/\left((1-\sigma)\,\Theta_z^{(2)}\right)$, i.e. the stability is again replaced by the effective stability, and averaging over x. This leads to

$$\frac{D}{D\tau}\left\langle \frac{\bar{\theta}q}{(1-\sigma)\,\Theta_z^{(2)}} \right\rangle + \langle q\bar{w}\rangle = \left\langle \frac{qw'}{1-\sigma} \right\rangle \tag{3.19}$$

whereas the parentheses $\langle\cdot\rangle$ just as in (2.34) denote the average in x. For this zonal average, periodic fields in x or an unbounded domain plus boundedness of all fields is assumed, so that the identity $\langle\phi_x\rangle = 0$ obtains.

The term on the right hand side can be interpreted in two different ways. It can either be included in the definition of the pseudo-momentum by setting

$$\tilde{p}_{\mathrm{alt}} := \left\langle \frac{\bar{\theta}q}{(1-\sigma)\,\Theta_z^{(2)}} \right\rangle - \left\langle \frac{qw'}{1-\sigma} \right\rangle \tag{3.20}$$

similar to the treatment of a sheared background flow in subsection 7.1.1 in [Büh09] or it can be interpreted as a forcing of the wave-flow, resulting in a forcing of pseudo-momentum. The latter interpretation is adopted here and $\tilde{p}$ is defined as

$$\tilde{p} := \left\langle \frac{\bar{\theta}q}{(1-\sigma)\,\Theta_z^{(2)}} \right\rangle \tag{3.21}$$

so (3.19) becomes

$$\frac{D\tilde{p}}{D\tau} + \langle q\bar{w}\rangle = \left\langle \frac{qw'}{1-\sigma} \right\rangle . \tag{3.22}$$

If $\sigma = 0$ and subsequently $w' = 0$, (3.21) reduces to the definition of Eulerian pseudo-momentum in [Büh09], p. 113 for non-sheared background flow. Otherwise the net micro-scale effects cause a forcing of pseudo-momentum, cf. subsection 6.3.2 in [Büh09]. However, the forcing has not to be modelled but is readily provided by the micro-scale dynamic equations $(2.70)_{5,6}$.

By multiplying with $\rho^{(0)}$ and using the anelastic constraint $(2.70)_4$, the second term in (3.22) can be transformed as follows

$$\begin{aligned}
\left\langle \rho^{(0)} q\bar{w} \right\rangle &= \left\langle \rho^{(0)} \left(u_z - \bar{w}_x\right) \bar{w} \right\rangle \\
&= \left\langle \rho^{(0)} u_z \bar{w} \right\rangle - \rho^{(0)} \left\langle \bar{w}_x \bar{w} \right\rangle \\
&= \left\langle \rho^{(0)} u \bar{w} \right\rangle_z - \left\langle u \left(\rho^{(0)} \bar{w} \right)_z \right\rangle \\
&= \left\langle \rho^{(0)} u \bar{w} \right\rangle_z + \rho^{(0)} \left\langle u u_x \right\rangle \\
&= \left\langle \rho^{(0)} u \bar{w} \right\rangle_z .
\end{aligned} \tag{3.23}$$

Using (3.23), (3.22) becomes

$$\rho^{(0)} \tilde{p}_\tau + \underbrace{\left\langle \rho^{(0)} u \bar{w} \right\rangle_z}_{=\partial_z \tau_{\mathrm{net}}} = \rho^{(0)} \underbrace{\left\langle \frac{qw'}{1-\sigma} \right\rangle}_{:=\tilde{\mathcal{F}}} \tag{3.24}$$

corresponding to the equation for pseudo-momentum in [Büh09], p. 141. Equation (3.24) demonstrates how changes of pseudo-momentum in the presented model, similar to the sheared and non-sheared dry case analyzed in [Büh09], are directly related to vertical changes in the momentum flux τ_{net} defined in (2.34) as well as forcing by micro-scale dynamics.

Chapter 6 in [Büh09] analyzes the response of a mean-flow to waves of asymptotically small amplitude a. It is found that the average $\mathcal{O}(a^2)$ zonal flow response to waves $\langle u_2 \rangle$ evolves according to

$$\partial_t \langle u_2 \rangle = \partial_t \tilde{p} - \tilde{\mathcal{F}}. \tag{3.25}$$

As mentioned in [RKM10], the derivation of the model in the present thesis can be equivalently formulated as an asymptotic analysis for small wave amplitudes if the dimensional governing equations are non-dimensionalized with a reference velocity

$$u_{\mathrm{ref}} = N h_{\mathrm{sc}} = 100 \text{ m s}^{-1} \tag{3.26}$$

set by the timescale of internal waves instead of advection. The distinguished limit (2.8) then becomes

$$\mathrm{M} \sim \overline{\mathrm{Fr}} \sim \varepsilon, \quad \mathrm{Ro_B} \sim \varepsilon^{-2} \quad \text{as } \varepsilon \to 0 \tag{3.27}$$

and the expansions of the velocity read

$$\mathbf{u} = \mathbf{u}^{\infty} + \varepsilon \mathbf{u}^{(0)}(x,z,t) + \mathcal{O}(\varepsilon^2) \quad \text{and} \quad w = \varepsilon w^{(0)}(\eta,x,z,t) + \mathcal{O}(\varepsilon^2). \tag{3.28}$$

Thus the amplitude of the wave-related velocity field $\left(\mathbf{u}^{(0)}, w^{(0)}\right)$ is now a small parameter, just as in [Büh09]. The derivation employing this ansatz is equivalent to the one presented in chapter 2 and the obtained model is again (2.70).

Supposedly, the analysis from [Büh09] can be adopted to demonstrate that the mean-flow response to waves governed by (2.70) also evolves according to (3.25). Employing the pseudo-momentum equation (3.24) forced by the tower-scale dynamics would then allow to analytically address the effect of moisture on the wave-forcing of a mean-flow.

3.1.5. Oscillator as Source of Gravity Waves

In [LRC01], possible mechanisms how tropical deep convection generates gravity waves are investigated, employing high-resolution, three-dimensional simulations. They analyze the obtained results by combining the governing equations into a single, forced linear wave equation for vertical velocity, see equation (6) in [LRC01], which for an unsheared background flow reads

$$D_{tt}\left[\nabla^2 w - \left(\frac{w}{H_\mathrm{s}}\right)_z\right] + N^2 \nabla_{||}^2 w = \mathcal{F}. \tag{3.29}$$

The source term $\mathcal{F}$ is split into three components

$$\mathcal{F} = \underbrace{\mathcal{F}_\mathrm{a}}_{\text{advection}} + \underbrace{\mathcal{F}_\mathrm{h}}_{\text{heating}} + \underbrace{\mathcal{F}_\mathrm{s}}_{\text{shear}} \tag{3.30}$$

corresponding to different mechanisms of gravity wave generation, and the magnitude of the different components is assessed from the gained simulation data. [LRC01] conclude that the dominant forcing of (3.29) are oscillations around the "level of neutral buoyancy" (LNB) related to the advection component $\mathcal{F}_\mathrm{a}$ of (3.30). In the absence of source terms for velocity, denoted F_u, F_v, F_w in [LRC01], their expression for $\mathcal{F}_\mathrm{a}$ simplifies to

$$\mathcal{F}_\mathrm{a} = \nabla_{||}^2 F_\mathrm{b} \tag{3.31}$$

whereas F_b is the right hand side source term of the buoyancy equation. A similar expression can be derived from (2.70), in which F_b is provided by the tower-scale dynamics.

Combining $(2.70)_1 - (2.70)_4$ into a single equation for $\bar{w}$, using $\rho^{(0)} = \exp(-z)$, assuming $\nabla_x \sigma = 0$ and denoting $\nabla_x = \nabla_{||}$ and $\nabla_x^2 + \partial_{zz} = \nabla^2$ for a notation consistent with (3.29), yields

$$\frac{D^2}{D\tau^2}\left(\nabla^2 w - w_z\right) + (1-\sigma)\,\Theta_z^{(2)}\nabla_{||}^2 w = \nabla_{||}^2 \underbrace{\left(\Theta_z^{(2)} w'\right)}_{=F_\mathrm{b}} \tag{3.32}$$

whereas $F_\mathrm{b} = \Theta_z^{(2)} w'$ is the source term in the large-scale buoyancy equation $(2.70)_3$. Equation (3.32) is precisely the forced, linear wave equation (3.29) with $H_s = 1$, compatible with the fact that (3.32) is non-dimensional while (3.29) is not, and the stability N^2 replaced by the effective stability $(1-\sigma)\,\Theta_z^{(2)}$. Denote by

$$\mathcal{F} = \nabla_{||}^2 F_\mathrm{b} = \nabla_{||}^2 \left(\Theta_z^{(2)} w'\right) \tag{3.33}$$

the source term on the right hand side. Combining $(2.70)_5$ and $(2.70)_6$ after multiplication with $\Theta_z^{(2)}$ results in the equation

$$\frac{D^2}{D\tau^2}\mathcal{F} + \sigma\Theta_z^{(2)}\mathcal{F} = \sigma\,(1-\sigma)\,\Theta_z^{(2)}\nabla_{||}^2\bar{w} \tag{3.34}$$

for $\mathcal{F}$. Obviously, $\mathcal{F}$ is oscillatory, forced by the large-scale flow $\bar{w}$ and advected by the background flow u^∞. Thus the result in [LRC01], stemming from numerical simulations, that the main component of $\mathcal{F}$ is oscillatory and related to $\mathcal{F}_\mathrm{a}$ features, at least on the formal level of equations, an interesting similarity to the asymptotic model derived in the present thesis, exhibiting an oscillatory $\mathcal{F}$ in the closure of the leading order equations.

3.2. Energy

Employing the definitions from section 6.1 in [Büh09] and replacing the stability with the effective stability modified by σ, the kinetic and potential energy of the large-scale flow can be defined as

$$E_\mathrm{kin} := \frac{\rho^{(0)}}{2}\left(u^2 + \bar{w}^2\right) \quad , \quad E_\mathrm{pot} := \frac{\rho^{(0)}}{2}\frac{\bar{\theta}^2}{(1-\sigma)\,\Theta_z^{(2)}}. \tag{3.35}$$

Multiplying $(2.70)_{1-3}$ with $\rho^{(0)}u$, $\rho^{(0)}\bar{w}$ and $\rho^{(0)}\bar{\theta}$ respectively and using $(2.70)_4$ yields

$$\frac{DE_\mathrm{kin}}{D\tau} + \left(\rho^{(0)}u\pi\right)_x + \left(\rho^{(0)}\bar{w}\pi\right)_z = \rho^{(0)}\bar{w}\bar{\theta} \tag{3.36}$$

and

$$\frac{DE_\mathrm{pot}}{D\tau} = -\rho^{(0)}\bar{w}\bar{\theta} + \rho^{(0)}\frac{w'\bar{\theta}}{1-\sigma} + \rho^{(0)}\frac{\bar{C}_-\bar{\theta}}{(1-\sigma)\,\Theta_z^{(2)}}. \tag{3.37}$$

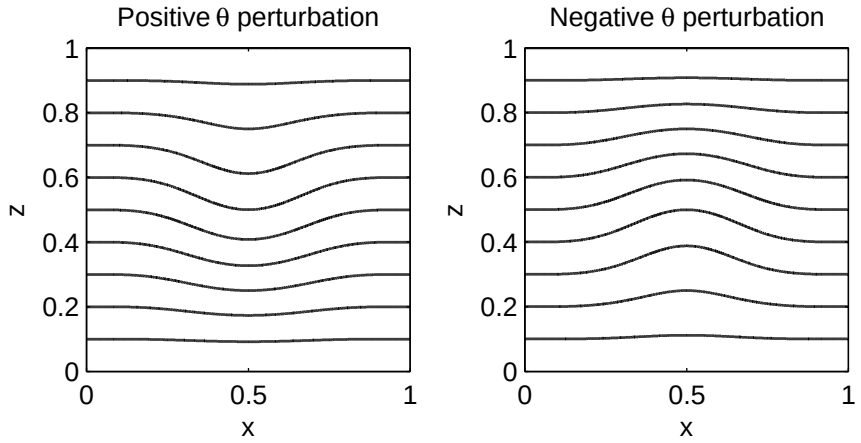

Figure 3.2.: *Stratification in the presence of a large-scale perturbation* $\bar{\theta}$. Left: *Positive perturbation* $\bar{\theta} > 0$. Right: *Negative perturbation* $\bar{\theta} < 0$.

Note that in the absence of the source terms related to tower-scale dynamics in (3.37), the total energy

$$E_{\text{tot}} := E_{\text{kin}} + E_{\text{pot}} \tag{3.38}$$

satisfies the conservation law

$$\frac{DE_{\text{tot}}}{D\tau} + \left(\rho^{(0)} u\pi\right)_x + \left(\rho^{(0)} \bar{w}\pi\right)_z = 0. \tag{3.39}$$

Integration over the volume of a parcel and assuming no flux of energy across the boundaries yields

$$\frac{D}{D\tau} \int_{V_{\text{parcel}}} E_{\text{tot}} \, dV = 0 \tag{3.40}$$

hence the total energy of a parcel is conserved in the absence of tower-scale effects. This is compatible with the following considerations: Figure 3.2 sketches isolines of the stratification for positive and negative large-scale deviations $\bar{\theta}$ from the background $\Theta^{(2)}$. The potential energy corresponds to the deformation of the isoline.

If a parcel with positive $\bar{\theta}$ (left figure) rises, i.e. $\bar{w} > 0$, isolines move upwards, reducing the deformation, corresponding to the reduction of E_{pot} by the negative source term $-\rho^{(0)}\bar{w}\bar{\theta}$ in (3.37). The potential energy is completely converted into kinetic energy according to (3.36) so the total energy of the parcel remains unchanged. This also holds true for a parcel with $\bar{\theta} < 0$ (right figure) and $\bar{w} < 0$. Vice versa, a parcel with $\bar{\theta} > 0$ (left figure) moving downward, i.e. $\bar{w} < 0$, increasing the deformation of isolines converts kinetic into potential energy exactly as a parcel with $\bar{\theta} < 0$ (right figure) and $\bar{w} > 0$, compatible with $\rho^{(0)}\bar{w}\bar{\theta} < 0$

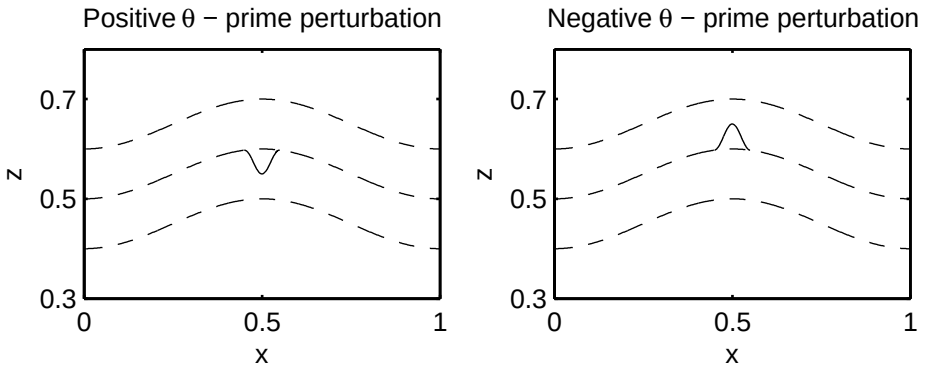

Figure 3.3.: *Stratification in the presence of a tower-scale perturbations θ'. The dashed lines are isolines of the large-scale stratification given by $\Theta^{(2)}$ plus $\bar{\theta}$.*
Left: $\theta' > 0$. Right: $\theta' < 0$.

reducing E_{kin} in (3.36) and increasing E_{pot} in (3.37). This is the basic oscillation mechanism for gravity waves in absence of latent heat release.

The tower-scale dynamics introduce an additional effect: The micro-scale velocity w' does not affect the parcel's kinetic energy. It provides however, according to $(2.70)_3$, a source term for $\bar{\theta}$ describing the net release or consumption of latent heat in saturated regions by small-scale up- or downdrafts. If $\bar{\theta} > 0$ the parcel is already warmer than the environment so released latent heat corresponding to $w' > 0$ increases the deformation of isolines, compatible with an increase of E_{pot} by $\bar{\theta}w' > 0$ in (3.37). Analogously, cooling by latent heat consumption of a parcel already cooler than the environment, i.e. $w' < 0$ and $\bar{\theta} < 0$ also increases the potential energy by $w'\bar{\theta} > 0$ in (3.37).

The other way round, if a parcel with $\bar{\theta} > 0$ is cooled by $w' < 0$ or a parcel with $\bar{\theta} < 0$ is warmed by $w' > 0$, the source term $\bar{\theta}w'$ is negative, resulting in a decrease of the parcel's potential energy E_{pot}, as the micro-scale influence does counteract the large-scale deviation $\bar{\theta}^{(3)}$ from the background stratification $\Theta^{(2)}$.

Cooling by evaporating rain described by the source term $\bar{C}_- < 0$ has a similar effect, reducing E_{pot} for $\bar{\theta} > 0$ and increasing it for $\bar{\theta} < 0$.

Analogously to (3.35) define the tower-scale energies as

$$E'_{\text{kin}} := \frac{\rho^{(0)}}{2}(w')^2 \ , \quad E'_{\text{pot}} := \frac{\rho^{(0)}}{2}\frac{(\theta')^2}{\sigma\Theta_z^{(2)}}. \tag{3.41}$$

They satisfy

$$\frac{DE'_{\text{kin}}}{D\tau} = \rho^{(0)}w'\theta' \tag{3.42}$$

and

$$\frac{DE'_{\text{pot}}}{D\tau} = -\rho^{(0)} w'\theta' + \rho^{(0)} (1-\sigma)\, \bar{w}\theta' - \rho^{(0)} \frac{\bar{C}_- \theta'}{\Theta_z^{(2)}}. \tag{3.43}$$

The source term $\pm\rho^{(0)} w'\theta'$ corresponds to an analogous conversion mechanism between tower-scale kinetic and potential energy as described for the large-scale energies above.

Figure 3.3 sketches a "zoomed in" example of small-scale perturbations θ' from a large-scale stratification described by $\bar{\theta}$. The figure is somewhat simplified, because positive or negative θ' only indicates positive or negative perturbation from the solid $\bar{\theta}$ isoline *on average*, but not at every single point. Thus the isoline of the perturbation could, in principle, oscillate around the dashed $\bar{\theta}$-isoline as well. The following consideration thus refers to *average* effects and does not hold point wise for every η.

The tower-scale potential energy E'_{pot} corresponds to the difference between the dashed line, indicating the large-scale stratification given by Θ^2 and $\bar{\theta}^{(3)}$ and the solid isoline, containing also the contribution of θ'. If in the situation sketched in the left figure with $\theta' > 0$ the dashed lines are moved upward by a large-scale updraft $\bar{w} > 0$, the tower-scale potential energy E'_{pot} increases according to the positive source term $\bar{w}\theta'$ in (3.43). For a large-scale downdraft, the dashed lines are displaced downward and E'_{pot} decreases according to $\bar{w}\theta' < 0$. Analogously, in the situation sketched in the right figure with $\theta' < 0$, a large-scale downdraft $\bar{w} < 0$ increases E'_{pot} while an updraft decreases it, compatible with a positive and negative $\bar{w}\theta'$ in (3.43) respectively.

Evaporative cooling of rain reduces the large-scale temperature $\bar{\theta}$ and increases the deformation of the dashed isolines, which indicate a positive $\bar{\theta} > 0$ in both figures. In the left figure this increases E'_{pot} compatible with $-\theta'\bar{C}_- > 0$ while for the right figure $-\theta'\bar{C}_- < 0$ obtains and E'_{pot} decreases.

3.3. Structure of Plane Wave Solutions

3.3.1. Dispersion relation

The leading order density for a near-homentropic atmosphere in the Newtonian limit $(\gamma \to 1) = \mathcal{O}(\varepsilon)$, see [KM06], reads

$$\rho^{(0)}(z) = \exp(-z) \tag{3.44}$$

in non-dimensional terms. Thus the anelastic constraint $(2.70)_4$ can be rewritten as

$$u_x + \bar{w}_z - \bar{w} = 0. \tag{3.45}$$

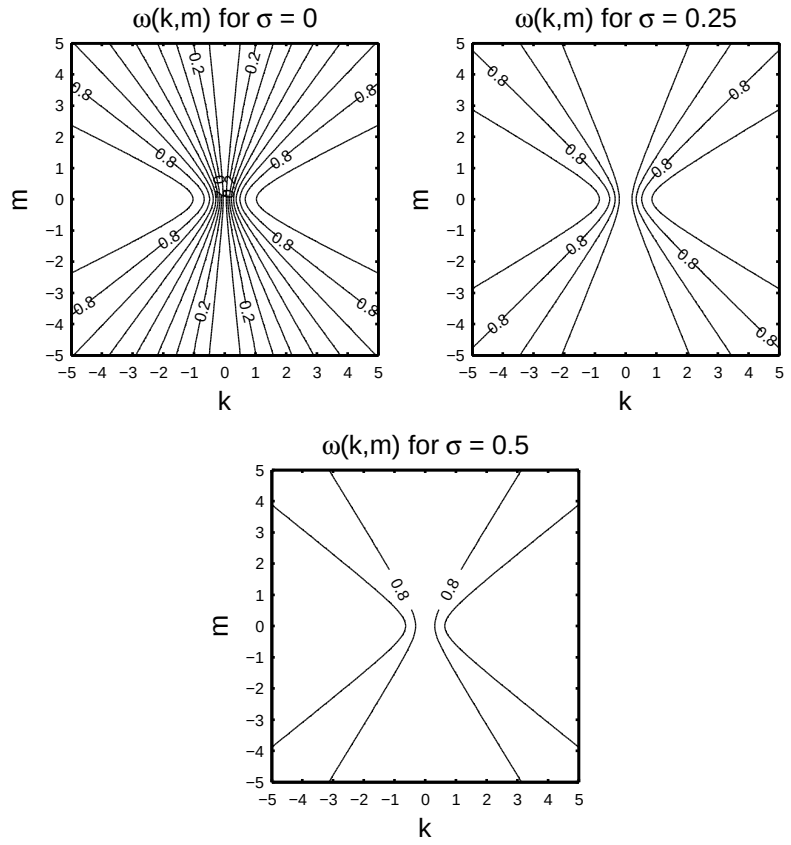

Figure 3.4.: *Isolines of the frequency* ω_{intr} *depending on the wave vector* (k, m) *with* $\sqrt{\Theta_z^{(2)}} = 1$ *for* $\sigma = 0$, $\sigma = 0.25$ *and* $\sigma = 0.5$. *The interval between isolines is* 0.1 *in all three figures.*

Applying a standard plane wave ansatz results in a complex valued dispersion relation as the decreasing density (3.44) leads to growing amplitudes of gravity waves with height. A real valued expression is obtained by allowing for a vertically growing amplitude in the ansatz. Insert

$$\phi(x, z, \tau) = \hat{\phi} \exp(\mu z) \exp(i(kx + mz - \omega\tau)) \tag{3.46}$$

with $\phi \in \{\bar{u}, \bar{w}, \bar{\theta}, \pi, w', \theta'\}$ into (2.70) and assume, for the purpose of this section, $\bar{C}_- = 0$ i.e. no source terms from evaporation of rain and that σ is uniform in x. The resulting equations read

$$\begin{aligned}
-i\omega\hat{\tilde{u}} + u^\infty ik\hat{\tilde{u}} + ik\hat{\pi} &= 0 \\
-i\omega\hat{\tilde{w}} + u^\infty ik\hat{\tilde{w}} + (im+\mu)\hat{\pi} &= \hat{\tilde{\theta}} \\
-i\omega\hat{\tilde{\theta}} + u^\infty ik\hat{\tilde{\theta}} + (1-\sigma)\Theta_z^{(2)}\hat{\tilde{w}} &= \Theta_z^{(2)}\hat{w}' \\
ik\hat{\tilde{u}} + (im+\mu)\hat{\tilde{w}} - \hat{\tilde{w}} &= 0 \\
-i\omega\hat{w}' + u^\infty ik\hat{w}' &= \hat{\theta}' \\
-i\omega\hat{\theta}' + u^\infty ik\hat{\theta}' + \sigma\Theta_z^{(2)}\hat{w}' &= \sigma(1-\sigma)\Theta_z^{(2)}\hat{\tilde{w}}.
\end{aligned} \tag{3.47}$$

Successive elimination of the $\hat{\phi}$ results in

$$(\omega - u^\infty k)^2 = \frac{k^2 - \sigma(\mu^2 - \mu - m^2) - \sigma i(2\mu m - m)}{k^2 - (\mu^2 - \mu - m^2) - i(2\mu m - m)}\Theta_z^{(2)}. \tag{3.48}$$

Setting

$$\mu = \frac{1}{2} \tag{3.49}$$

yields

$$(\omega - u^\infty k)^2 = \frac{k^2 + \sigma(m^2 + \frac{1}{4})}{k^2 + m^2 + \frac{1}{4}}\Theta_z^{(2)} \tag{3.50}$$

and rearranging terms provides the final, real-valued dispersion relation

$$\omega = u^\infty k + \omega_{\text{intr}} = u^\infty k \pm \sqrt{\frac{k^2 + \sigma(m^2 + \frac{1}{4})}{k^2 + m^2 + \frac{1}{4}}\Theta_z^{(2)}}. \tag{3.51}$$

For $\sigma = 0$, (3.51) is identical to the dispersion relation for the pseudo-incompressible equations derived in [Dur89]. ω_{intr} is the so-called intrinsic frequency, seen by an observer moving with the background flow. Figure 3.4 shows the dependence of ω_{intr} on the wave vector (k, m) for $\sigma = 0, 0.25, 0.5$. Just as in the dry case, the frequency depends only on the direction of the wave vector but not on its magnitude. As σ increases, the accessible range of frequencies narrows down, the minimum propagating frequency

$$\omega_{\text{intr,min}} = \sqrt{\sigma\Theta_z^{(2)}} \tag{3.52}$$

being obtained for purely vertically oriented wave vectors $(0, m)$.

Interestingly, for the incompressible case without the 1/4 term, (3.51) equals the dispersion relation for internal gravity waves in a rotating fluid, see e.g. section 8.4 in [Gil82], with the Coriolis parameter f^2 replaced by $\sigma\Theta_z^{(2)}$. In the incompressible case, ω_{intr} can also be expressed as a function of the angle α between the wave vector (k, m) and the horizontal

$$\omega_{\text{intr,incomp}} = \sqrt{\left(\cos^2(\alpha) + \sigma\sin^2(\alpha)\right)\theta_z^{(2)}}. \tag{3.53}$$

3.3.2. Temporal Evolution of a Plane Wave

In order to investigate how a plane wave solution of (2.70) evolves with time, insert an ansatz

$$\phi\left(x,z,\tau\right)=\hat{\phi}(\tau)\exp\left(\mu z\right)\exp\left(i(kx+mz)\right) \tag{3.54}$$

with $\phi\in\left\{u,\bar{w},\bar{\theta},\pi,w',\theta'\right\}$. As before, $\exp(\mu z)$ captures the amplitude growth with height caused by decreasing density. Assuming $u^{\infty}=0$ here, setting $\mu=0.5$ as before and combining $(2.70)_1$ - $(2.70)_4$ into a single equation for $\bar{w}$ as well as $(2.70)_5$ and $(2.70)_6$ into an equation for w' yields, after dropping the hats, the second order linear system of ordinary differential equations

$$\begin{aligned}\left(k^2+m^2+\frac{1}{4}\right)\bar{w}_{\tau\tau}+\left(1-\sigma\right)\Theta_z^{(2)}k^2\bar{w}&=\Theta_z^{(2)}k^2w'\\ w'_{\tau\tau}+\sigma\Theta_z^{(2)}w'&=\sigma\left(1-\sigma\right)\Theta_z^{(2)}\bar{w}\end{aligned} \tag{3.55}$$

or in vector-matrix form

$$\begin{pmatrix}\bar{w}\\ w'\end{pmatrix}_{\tau\tau}+\begin{pmatrix}\frac{(1-\sigma)\Theta_z^{(2)}k^2}{k^2+m^2+0.25} & -\frac{\Theta_z^{(2)}k^2}{k^2+m^2+0.25}\\ -\sigma(1-\sigma)\Theta_z^{(2)} & \sigma\Theta_z^{(2)}\end{pmatrix}\begin{pmatrix}\bar{w}\\ w'\end{pmatrix}=0. \tag{3.56}$$

The non-zero eigenvalues of the system equal the solutions of the dispersion relation (3.51)

$$\omega_{\text{intr}}=\pm\sqrt{\frac{k^2+\sigma\left(m^2+\frac{1}{4}\right)}{k^2+m^2+\frac{1}{4}}\Theta_z^{(2)}}. \tag{3.57}$$

Although in (2.70) the parameter σ is only advected with u^{∞} and thus constant in τ in the absence of background flow, for illustration purposes (3.56) is solved numerically with a prescribed σ slowly varying in time

$$\sigma(\tau)=0.8\exp\left(-\frac{1}{2}\left(\frac{\tau-100}{20}\right)^2\right). \tag{3.58}$$

The employed ODE solver is *ode45* in MATLAB. The used initial values are $\bar{w}=0.5$ and $w'=0$, the wave numbers are $k=m=1$ and the stratification is set to $\sqrt{\Theta_z^{(2)}}=1$.

Figure 3.5 shows the obtained solutions. The upper figure shows the evolution of the amplitudes of $\bar{w}$ and w' as well as the prescribed σ. w' is zero initially, but increases as σ increases at the expense of $\bar{w}$. The amplitude of $\bar{w}$ increases back to its original value and w' vanishes as σ vanishes. The lower figure shows the evolution of the non-saturated displacement ξ_{us}, cf. (3.12), (3.13). As indicated in (3.15), by reducing the effective stability a non-zero σ increases the amplitude of ξ_{us}. Figure in 3.6 shows the frequency of maxima of $\bar{w}$ (diamonds) as well as the frequency ω_{intr} as a solid line, computed analytically from the dispersion relation

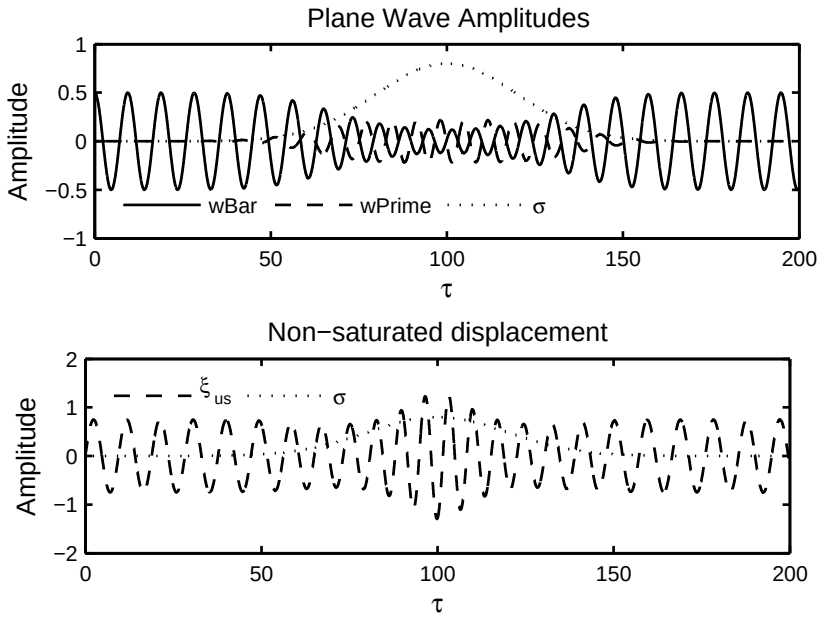

Figure 3.5.: *Numerical solution of* (3.55) *with prescribed* σ. Upper: *Amplitudes of* $\bar{w}$, w' *over time.* Lower: *Amplitudes of the resulting displacement* ξ_{us} *over time.*

(3.51). Despite naturally exhibiting some lag, the maxima-computed frequencies evolve in good agreement with the values computed from the dispersion relation (3.51). The increase of frequency by σ matches the results from the analysis of the dispersion relation in subsection 3.3.1, where it is found that σ reduces the range of attainable values for ω_{intr} by raising the minimum possible frequency while leaving the maximum value constant.

3.3.3. Group velocity

Concept

To illustrate the concept of group velocity, an example discussed in [Gri02] is briefly presented here. Consider a wave-packet solution of some initial value problem, given as a superposition of Fourier-modes

$$u(x,t) = \int_{-\infty}^{\infty} F(k) \exp\left(i(kx - \omega t)\right) dk. \tag{3.59}$$

Assume that $F(k)$ is supported in the vicinity of a dominant wave number k_0 and rapidly decays with increasing distance from it. The dispersion relation of the

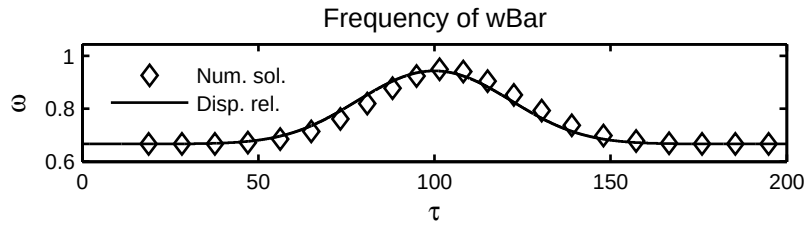

Figure 3.6.: *Frequencies computed from distance between maxima (diamonds) in $\bar{w}$ and analytically from the dispersion relation (solid line).*

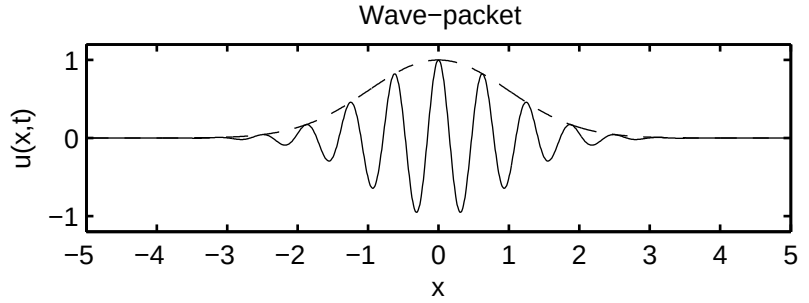

Figure 3.7.: *A wave-packet: The individual modes travel according to the phase velocity ω/k while the wave-packet itself, visualized by its envelope, travels with the group velocity c_g.*

system, expressing the frequency ω as a function of the wave number k, can be approximated as

$$\omega(k) \approx \omega(k_0) + b_1 (k - k_0) + b_2 (k - k_0)^2 \tag{3.60}$$

where

$$b_1 = \left.\frac{d\omega}{dk}\right|_{k=k_0} =: c_\mathrm{g} \quad \text{and} \quad b_2 = \frac{1}{2} \left.\frac{d^2\omega}{dk^2}\right|_{k=k_0} . \tag{3.61}$$

Using this in (3.59) and introducing $\kappa := k - k_0$ yields

$$u(x,t) \approx \exp\left(i(k_0 x - \omega_0 t)\right) \int_{-\infty}^{\infty} F(k_0 + \kappa) \exp\left(i(\kappa x - c_\mathrm{g} t) \exp\left(-ib_2\kappa^2 t\right) d\kappa. \tag{3.62}$$

The term proportional to κ^2 is a small correction, so defining

$$A(x,t) = \int_{-\infty}^{\infty} F(k_0 + \kappa) \exp\left(i(\kappa x - c_\mathrm{g} t)\, d\kappa \right. \tag{3.63}$$

leads to

$$u(x,t) \approx A(x,t) \exp\left(i(k_0 x - \omega_0 t)\right). \tag{3.64}$$

Thus to leading order, the wave-packet described by u is a single plane wave with wave number k_0, frequency ω_0 and moving at velocity ω_0/k_0 with a time-space dependent amplitude $A(x,t)$, travelling at speed c_g. Hence the phase velocity is the velocity at which individual modes of a wave-packet travel while the group velocity is the speed at which the packet as a whole propagates, see figure 3.7. Phase- and group velocity are, in general, different and may even point in opposite directions. In figure 3.7 for example, the individual modes might travel from right to left while the wave-packet itself travels from left to right. As shown in section 4.4 in [Lig78], group velocity is also associated with the flux of wave energy.

Group Velocity in the Model

Computing the derivative of (3.51) with respect to k and m yields the group velocity

$$\mathbf{c}_\mathrm{g} = (u_\mathrm{g}, w_\mathrm{g}) = (u^\infty, 0) \pm \frac{(1-\sigma)\sqrt{\theta_z^{(2)}}}{(k^2+m^2+\frac{1}{4})^{\frac{3}{2}}(k^2+\sigma(m^2+\frac{1}{4}))^{\frac{1}{2}}} \left(k(m^2+\frac{1}{4}), -mk^2\right). \tag{3.65}$$

In a dry ($\sigma = 0$), incompressible ($\mu = 0$, so no $\frac{1}{4}$ term) atmosphere, $\mathbf{c}_\mathrm{g}$ simplifies to the well-known expression for the group velocity of internal waves in a stratified fluid, see e.g. section 4.4 in [Lig78],

$$\mathbf{c}_{\mathrm{g,dry,inc}} = (u^\infty, 0) \pm \frac{m\sqrt{\theta_z^{(2)}}}{(k^2+m^2)^{\frac{3}{2}}}(m, -k). \tag{3.66}$$

One essential feature of these waves is that $\mathbf{c}_{\mathrm{g,dry,inc}} \perp (k,m)$, i.e. the direction of energy transport by waves is perpendicular to the direction of intrinsic phase propagation. Because of the 1/4 term, this does not hold for (3.65), but still waves with upward directed phase propagation, i. e. either positive m and positive branch in (3.51) and (3.65) or negative m and negative branch in (3.51) and (3.65), feature downward directed group velocity and vice versa.

As σ increases, the coefficient in (3.65) decreases and eventually, for $\sigma = 1$, vanishes. Thus increasing moisture reduces the transport of energy by waves and eliminates it completely in all-over saturated regions, sparing only advection of energy by u^∞.

The ratio of vertical to horizontal component of $\mathbf{c}_\mathrm{g}$ determines the slope at which a wave-packet propagates

$$\Delta_\mathrm{g} = \frac{w_\mathrm{g}}{u_\mathrm{g}}. \tag{3.67}$$

Figure 3.8 shows the angle between a line with slope $w_\mathrm{g}/u_\mathrm{g}$ and the horizontal depending on σ for a flow with $\sqrt{\Theta_z^{(2)}} = 1$ and $u^\infty = 0.1$. For all modes, moisture

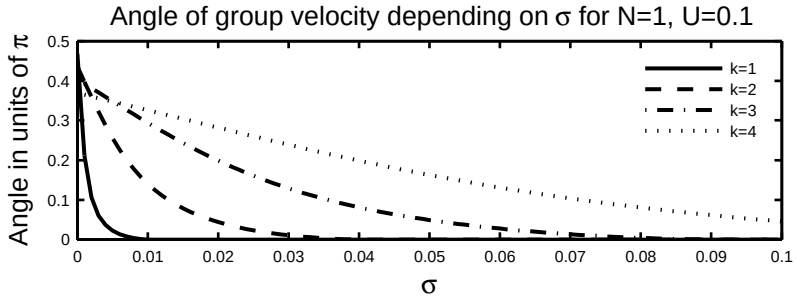

Figure 3.8.: *Angle between the direction of the group velocity and the horizontal for wave numbers* $k = 1, \ldots, 4$ *depending on* σ *in a steady-state flow with* $\sqrt{\Theta_z^{(2)}} = 1$ *and* $u^\infty = 0.1$.

decreases the angle of the group velocity, so σ also reduces the propagation angle of wave-packets. See subsection 3.4.2 for illustration.

3.3.4. Taylor-Goldstein Equation

A special class of simplified solutions are those with non-constrained vertical profiles but plane wave structure in the horizontal and in time, i.e.

$$\phi(x, z, \tau) = \hat{\phi}(z) \exp(\mu z) \exp(ik(x - c\tau)). \tag{3.68}$$

Here, $c = \omega/k$ denotes the horizontal phase speed observed at a fixed height, while $\phi \in \{\bar{u}, \bar{w}, \bar{\theta}, \pi, w', \theta'\}$. The term involving μ describes, just as in the derivation of the dispersion relation, the growing amplitudes with height caused by the decreasing density in the anelastic model. Inserting (3.68) into (2.70) and eliminating all $\hat{\phi}$ except for $\hat{\bar{w}}$ yields

$$\left[\frac{\Theta_z^{(2)} - k^2(u^\infty - c)^2}{k^2(u^\infty - c)^2 - \sigma\Theta_z^{(2)}} k^2\right] \hat{\bar{w}} + \mu(\mu - 1)\hat{\bar{w}} + (2\mu - 1)\hat{\bar{w}}_z + \hat{\bar{w}}_{zz} = 0. \tag{3.69}$$

Setting $\mu = 1/2$ as in 3.3.1 results in the final equation

$$\left[\frac{\Theta_z^{(2)} - k^2(u^\infty - c)^2}{k^2(u^\infty - c)^2 - \sigma\Theta_z^{(2)}} k^2 - \frac{1}{4}\right] \hat{\bar{w}} + \hat{\bar{w}}_{zz} = 0. \tag{3.70}$$

This equation for the vertical profile $\hat{\bar{w}}(z)$ is called Taylor-Goldstein equation. In the incompressible, dry case, i. e. with $\sigma = 0$ and without the $1/4$ term, (3.70) reduces to its well-known incompressible dry counterpart derived e.g. in ch. 13 in [Etl96]. As the coefficient of $\hat{\bar{w}}$ depends on z, (3.70) is a second order ODE with varying coefficients.

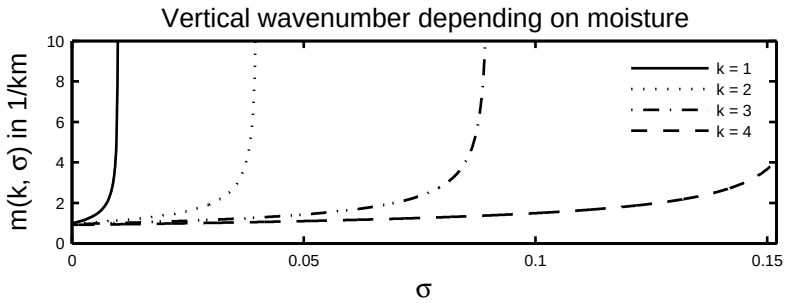

Figure 3.9.: *Steady-state vertical wave number $m(k)$ depending on σ for $k = 1, \ldots, 4$ with $\sqrt{\Theta_z^{(2)}} = 1$ and $u^\infty = 0.1$.*

3.3.5. Vertical Wave Numbers

The coefficient in (3.70) is the square of the local vertical wave number, so

$$m(z,k) = \pm\sqrt{\left[\frac{\Theta_z^{(2)} - k^2(u^\infty - c)^2}{k^2(u^\infty - c)^2 - \sigma\Theta_z^{(2)}}k^2 - \frac{1}{4}\right]}. \tag{3.71}$$

Figure 3.9 shows how, for steady-state solutions with $c = 0$, m depends on σ for different k. Increasing σ also increases m. Thus, as the vertical wavelength is inversely proportional to the wave number, moisture in the presented model reduces the vertical wavelength. This is contrary to the findings of [EL73b, JB85], who indicate an increase of vertical wavelength by moisture. Increasing m results in a steeper propagation angle of individual modes. However, as pointed out in subsection 3.3.3, moisture also reduces the angle of group-velocity, so that simultaneously the propagation angle of a wave pattern composed of a superposition of numerous modes is bent towards the horizontal. Note that for some value $\sigma_c(k)$, the vertical wave numbers diverge to infinity. See section 3.5 for further discussion.

Cut-Off Wave Numbers in Steady-State Solutions

Modes with imaginary vertical wave number m are evanescent and do not propagate vertically but only decay exponentially with height, see section 6.8 in [Gil82]. Wave numbers k at which $m(k)$ turns from real (propagating) into imaginary (evanescent) are called cut-off wave numbers. For steady-state solutions (3.71) simplifies to

$$m(k) = \pm\sqrt{\left[\frac{\Theta_z^{(2)} - k^2(u^\infty)^2}{k^2(u^\infty)^2 - \sigma\Theta_z^{(2)}}k^2\right]}. \tag{3.72}$$

Neglect the 1/4 term for the course of this paragraph, as this clarifies the calculation without qualitatively affecting the result. If

$$|k| > k_{\text{up}} := \frac{\sqrt{\Theta_z^{(2)}}}{u^\infty} \tag{3.73}$$

the radicand in (3.72) yields an imaginary m and the corresponding mode is evanescent. This upper cut-off is independent of σ and likewise found in the dry case, see e.g. subsection 6.4.1 in [Büh09]. In contrast to the dry case, the radicand in (3.72) also turns negative for

$$\frac{\sqrt{\Theta_z^{(2)}}}{u^\infty} \geq \sqrt{\sigma}\frac{\sqrt{\Theta_z^{(2)}}}{u^\infty} =: k_{\text{low}} > |k|. \tag{3.74}$$

Thus moisture introduces a lower cut-off wave number absent in the dry non-rotating case. A similar mechanism is present in the regime of rotating gravity waves. There, the lower cut-off is f/u^∞, f being the Coriolis parameter, see subsection 8.2.3 in [Büh09]. However, because $f_{\text{dim}} \sim 10^{-4}$ s^{-1}, see section 7.5 in [Gil82], corresponding to a non-dimensional value of $f \sim 10^{-2}$ using $(2.35)_5$, the lower cut-off wave number in the rotating case is small. In contrast, $\sqrt{\sigma\Theta_z^{(2)}}$ is of order unity so that (3.74) can render a significant number of modes evanescent.

A typical value for the stability frequency in dimensional terms is $N = 0.01$ s^{-1} corresponding to $\sqrt{\Theta_z^{(2)}} = 1$. A typical background flow velocity is 10 m s^{-1} or $u^\infty = 0.1$. Consider small cloudy areas and set $\sigma = 0.1$. This results in an upper cut-off wave number $k_{\text{up}} = 10$ and a lower cut-off $k_{\text{low}} \approx 3.16$. The resulting non-dimensional minimum and maximum wavelengths are

$$\lambda_- = \frac{2\pi}{k_{\text{up}}} \quad \text{and} \quad \lambda_+ = \frac{2\pi}{k_{\text{low}}}. \tag{3.75}$$

The lengthscale $h_{\text{sc}} \approx 10^4$ m leads to a reference value for k of

$$k_{\text{ref}} = \frac{2\pi}{h_{\text{sc}}} \approx 2\pi 10^{-4} \text{ m}^{-1}. \tag{3.76}$$

Computing the dimensional values λ_+^*, λ_-^* corresponding to (3.75) by employing the reference value $\lambda_{\text{ref}} = 2\pi/k_{\text{ref}}$ set by (3.76) yields

$$\lambda_-^* = \frac{2\pi}{k_{\text{up}}}\frac{2\pi}{k_{\text{ref}}} = \frac{2\pi}{10}\cdot 10^4 \text{ m} \approx 6 \text{ km}\ , \quad \lambda_+^* = \frac{2\pi}{k_{\text{low}}}\frac{2\pi}{k_{\text{ref}}} \approx 20 \text{ km}. \tag{3.77}$$

Thus in dimensional terms, propagation is restricted to horizontal wavelengths between 6 km and 20 km. For $\sigma = 0.2$, the maximum wavelength is further reduced to 14 km, so even small values of σ prevent a significant range of wavelengths from propagating. The cut-off is illustrated by the examples in subsection 3.4.1.

3.4. Steady-State Orographic Waves

A widely investigated problem is the wave response excited by flow over a mountain in a stable stratified atmosphere. In this section, steady-state solutions of this type for (2.70) are derived for the simplified case of constant coefficients and compared to their dry counterparts. The description of the problem consists of the steady-state version of (2.70) on a domain $\Omega = [0, L] \times [0, H]$ plus a lower boundary condition set by topography. Letting h denote a function describing the shape of the hill the thereby imposed linearized boundary condition reads

$$w(x, 0, \tau) = u^\infty h_x(x), \tag{3.78}$$

see e.g. ch. 6 in [Büh09]. Periodic boundary conditions in x are assumed. At the upper boundary, a radiation boundary condition is required to prevent unphysical energy transport into the domain. Seek solutions of the form

$$\phi(x, z, \tau) = \exp(\mu z) \sum_{n=-N_x}^{n=N_x} \hat{\phi}^{(n)}(z) \exp(ik_n x) \tag{3.79}$$

with $\mu = 0.5$ and $k_n = 2\pi n/L$. As demonstrated in subsection 3.3.4, for every $-N_x \leq n \leq N_x$ this leads to (3.70) with $c = 0$ i.e.

$$\left[\frac{\Theta_z^{(2)} - k_n^2 (u^\infty)^2}{k_n^2 (u^\infty)^2 - \sigma \Theta_z^{(2)}} k_n^2 - \frac{1}{4} \right] \hat{w}^{(n)} + \hat{w}_{zz}^{(n)} = 0. \tag{3.80}$$

Equation (3.80) has to be solved for the different n, and the superposition (3.79) yields the final solution. All figures in this section show quantities converted back into dimensional units for more descriptive results.

If the stratification $\Theta_z^{(2)}$, the background flow u^∞ and σ are all constant with height, (3.80) can be solved analytically

$$\hat{\hat{w}}^{(n)}(z) = A^{(n)} \exp(im(k_n)z) + B^{(n)} \exp(-im(k_n)z) \tag{3.81}$$

whereas $A^{(n)}$ and $B^{(n)}$ have to be determined according to the upper and lower boundary condition. For the propagating case, i.e. real $m(k_n)$, the upper boundary condition has to rule out downward directed energy propagation into the domain, see [KD82, Bou83]. The background flow is always assumed to be positive, i.e. $u^\infty > 0$. Thus if setting $\omega = 0$ in (3.51), the sign of the root has to be the opposite of the sign of k and hence the sign of the root in (3.65) must also be $-\mathrm{sgn}(k)$ so that

$$\mathrm{sgn}(w_\mathrm{g}) = \mathrm{sgn}(k)\mathrm{sgn}(m). \tag{3.82}$$

In order to have $w_\mathrm{g} \geq 0$ in (3.65), m has to be positive if $\mathrm{sgn}(k) > 0$ and negative if $\mathrm{sgn}(k) < 0$. Thus set

$$m(k_n) = \mathrm{sgn}(k_n) \sqrt{\frac{\Theta_z^{(2)} - k_n^2 (u^\infty)^2}{k_n^2 (u^\infty)^2 - \sigma \Theta_z^{(2)}} k_n^2 - \frac{1}{4}} \tag{3.83}$$

and $B = 0$ in (3.81). For imaginary $m(k)$, choose the sign so that $\exp(im(k_n)z) \to 0$ for $z \to \infty$ and again set $B = 0$.

For solutions of type (3.79), the lower boundary condition (3.78) reads

$$\hat{\tilde{w}}^{(n)}(z = 0) = u^{\infty} i k_n H^{(n)} \tag{3.84}$$

whereas $H^{(n)}$ is the n-th coefficient in the Fourier representation of the topography, i.e.

$$h(x) = \sum_{n=-\infty}^{n=\infty} H^{(n)} \exp(i k_n x). \tag{3.85}$$

Hence the remaining coefficient reads

$$A^{(n)} = u^{\infty} i k_n H^{(n)}. \tag{3.86}$$

To allow for numerical evaluation of (3.79), truncate the series and set

$$A^{(n)} = 0 \quad \text{for} \quad |n| > N_x. \tag{3.87}$$

The topographies studied in subsection 3.4.1 excite only two modes k_{n_1}, k_{n_2}, so for

$$N_x \geq \max\{k_{n_1}, k_{n_2}\} \tag{3.88}$$

the approximation (3.87) is exactly satisfied. While the topography in subsection 3.4.2 does in principal excite modes of all wave numbers, the amplitudes decay as k_n increases so if N_x is chosen sufficiently large the effect of truncating higher wave number modes is negligible.

The final analytical solution for the vertical profile of an individual mode reads

$$\hat{\tilde{w}}^{(n)}(z) = u^{\infty} i k_n H^{(n)} \exp(im(k_n)z) \tag{3.89}$$

while the superposition of all computed modes reads

$$\hat{\tilde{w}}(x, z) = \exp(\mu z) \sum_{n=-N_x}^{n=N_x} u^{\infty} i k_n H^{(n)} \exp\left(i(m(k_n)z + k_n x)\right). \tag{3.90}$$

By employing the anelastic constraint (3.45), the profiles of the modes of horizontal velocity can be computed according to

$$\hat{u}(z) = [1 - m(k_n)]\, u^{\infty} H^{(n)} \exp(im(k_n)z), \tag{3.91}$$

yielding the final $u(x, z)$ by superposition (3.79) with $\phi = u$.

3.4.1. Sinusoidal Topography

For a topography h composed of the superposition of sine waves of different wave numbers, i.e.

$$h(x) = \sum_{n=1}^{N_x} h_n \sin(k_n x) \tag{3.92}$$

with again $k_n = 2\pi n/L$, the coefficient $A^{(n)}$ in (3.86) for a given n is non-zero only if h_n is non-zero. The transformation of modes from propagating to evanescent with increasing σ is illustrated here for the simple cases of $h_2 \neq 0$ and $h_1, h_2 \neq 0$. Set the stability frequency to $\sqrt{\Theta_z^{(2)}} = 1$ or 0.01 s^{-1} in dimensional terms, the background flow to $u^\infty = 0.1$ or 10 m s^{-1}. The domain is $[0, 2\pi] \times [0, 1]$ in non-dimensional units, multiply the numbers by 10 km for dimensional values.

Single Mode Consider a topography

$$h(x) = h_2 \sin(2x) \tag{3.93}$$

with $h_2 = 0.04$ corresponding to a sinusoidal hill with a maximum height of 400 m. Figure 3.10 shows the real part of the resulting vertical velocity $\bar{w}$ for $\sigma = 0$, $\sigma = 0.02$ and $\sigma = 0.05$. Plotted are isolines of $\bar{w}$ in steps of 0.25 m s^{-1} in dimensional terms, whereas dotted lines represent negative values. In the dry case, no lower cut-off wave number exists and the single excited mode propagates upwards into the direction set by the wave vector $(2, m(2))$. For $\sigma = 0.02$, the lower cut-off is $k_{\text{low}} = \sqrt{0.02} \cdot 1/0.1 \approx 1.4$, so the mode still propagates. However, according to the increase of m pointed out in figure 3.9, the angle between the direction of phase propagation and the horizontal has become slightly steeper. For $\sigma = 0.05$, thus $k_{\text{low}} = \sqrt{0.05} \cdot 10 \approx 2.2$, the mode has become evanescent. Only a very weak wave-response is visible close to the surface.

Two Modes Extending the topography by a $k = 1$ mode, i.e.

$$h(x) = h_1 \sin(x) + h_2 \sin(2x) \tag{3.94}$$

again with $h_1 = h_2 = 0.04$, results in non-zero amplitudes for the modes $k_1 = 1$ and $k_2 = 2$. All other quantities remain unchanged. Figure 3.11 again shows isolines of $\bar{w}$. The first figure corresponds to the dry solution with $\sigma = 0$. The second figure corresponds to $\sigma = 0.02$, where the $k = 1$ mode is evanescent. With only the $k = 2$ mode propagating, the pattern of the solution is very similar to the second figure in 3.10, except for a small contribution from the evanescent mode in the lower regions near the surface. The third figure shows the solution for $\sigma = 0.05$, where now also the second mode is evanescent. Again, there is only a weak wave-response close to the ground.

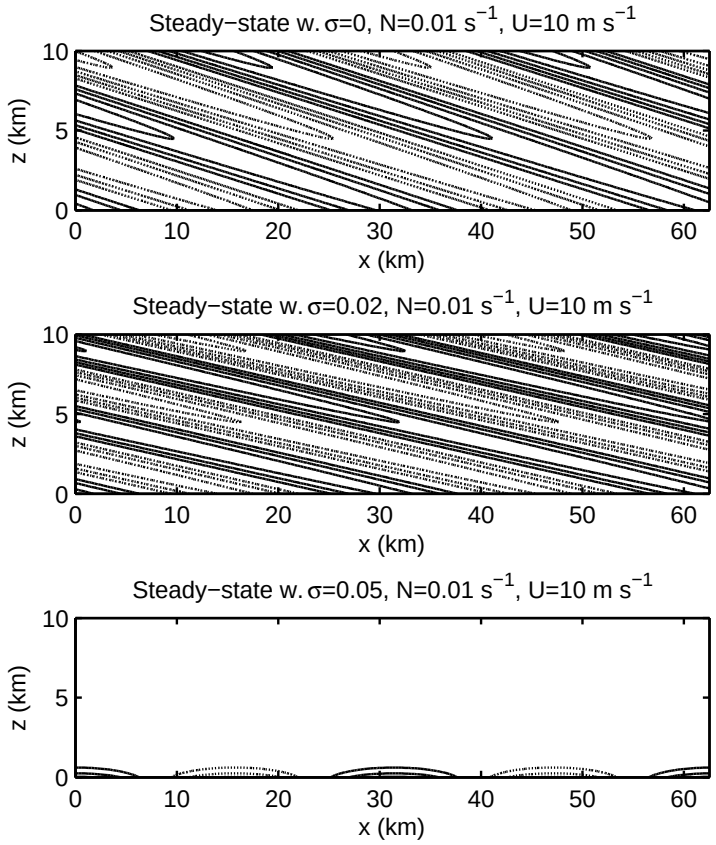

Figure 3.10.: *Steady-state orographic waves excited by a simple sinusoidal topography with single horizontal wave number $k = 2$ for $\sigma = 0$, $\sigma = 0.02$ and $\sigma = 0.05$. The interval between isolines is $0.25\ m\ s^{-1}$. Dotted lines represent negative values.*

3.4.2. Witch of Agnesi Topography

The Witch of Agnesi topography reads

$$h(x) = \frac{h}{1 + \left(\frac{x - x_0}{l}\right)^2} \tag{3.95}$$

whereas h is the height of the hill, l is a measure of its width and x_0 is the middle of the domain, so that the top of the hill is in the center. The domain employed here is $[0, 8] \times [0, 1]$ but the solution is plotted only on $[2, 6] \times [0, 1]$. The topography (3.95) excites waves of all wave numbers, however the amplitude of the modes decreases as k increases. For $n = 100$, the resulting $H^{(n)}$ is of the order of 10^{-7}, so using $N_x = 100$, i.e. 201 modes here and employing (3.87) for modes outside

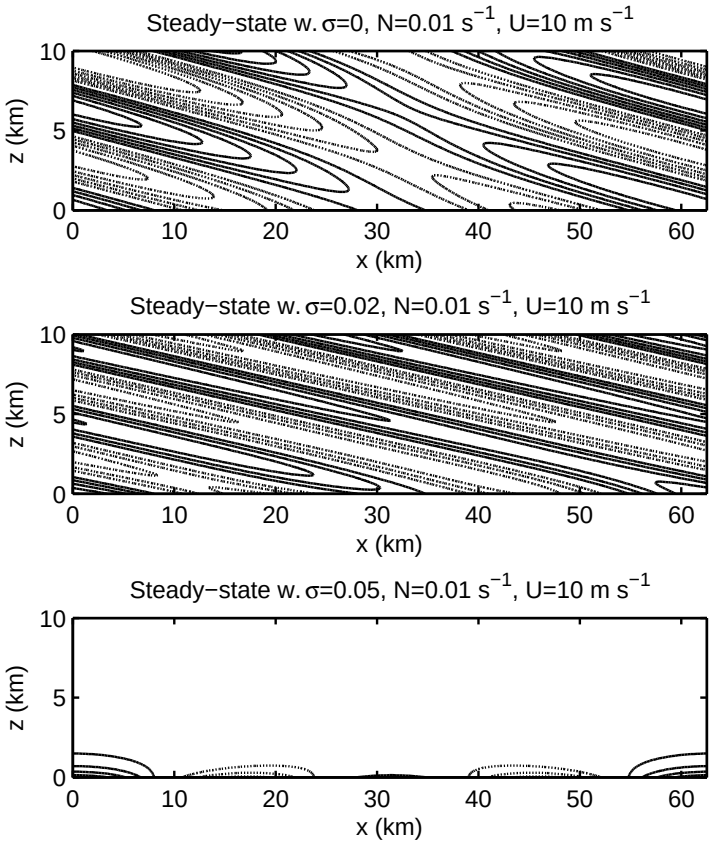

Figure 3.11.: *Steady-state orographic wave excited by a mountain consisting of two sinusoidal modes. Shown are isolines of vertical velocity in steps of* 0.25 $m\ s^{-1}$*, dotted lines represent negative values.*

this range, is sufficient to produce meaningful solutions. No noticeable change in the solution is detectable if N_x is increased. Figure 3.12 shows the contour lines of the dimensionalized vertical velocity $\bar{w}$ in steps of 0.25 m s^{-1} for $\sigma = 0$, $\sigma = 0.1$, $\sigma = 0.5$ and $\sigma = 0.75$. The dashed line visualizes the average slope (3.67) of group velocity computed over all propagating modes, whereas every mode is assigned a weight equal to its amplitude, i.e.

$$\Delta_{\mathrm{g,av}} = \frac{1}{\sum_{n=-N_x}^{n=N_x} |A_*^{(n)}|} \sum_{n=-N_x}^{n=N_x} |A_*^{(n)}| \Delta_{\mathrm{g}} \left(k_n, m(k_n)\right) \tag{3.96}$$

with

$$A_*^{(n)} := \begin{cases} A^{(n)} & : \text{mode is propagating} \\ 0 & : \text{mode is evanescent} \end{cases} . \tag{3.97}$$

The slope of the excited wave pattern is reduced with increasing σ, according to the reduction of (3.96). Additionally, an increasing number of modes become evanescent, resulting in a significant reduction of amplitudes.

The reduced angle of propagation is compatible with the following heuristic: The parameter

$$\mathrm{Fr}_{\mathrm{baroclinic}} = \frac{u^{\infty}}{Nl}, \tag{3.98}$$

denoting the ratio of advection speed to velocity of internal waves, is a measure of how close to hydrostatic balance the flow is, see e.g. [GK00]. It is small if the flow is almost hydrostatic and increases as non-hydrostatic effects become more dominant. As moisture reduces the effective stability $N^2_{\mathrm{eff}} = (1-\sigma)\,\Theta^{(2)}_z$, it increases $\mathrm{Fr}_{\mathrm{baroclinic}}$. Hydrostatic waves travel purely in vertical direction and the horizontal component increases the more non-hydrostatic the flow becomes. Hence it appears reasonable that moisture leads to a more horizontal propagation direction of orographic waves.

As discussed in subsection 2.2.1, an important quantity related to gravity waves is the vertical flux of horizontal momentum (2.34) reading $\rho^{(0)}\,\langle u\bar{w}\rangle$ here. For the steady-state waves presented here the momentum flux is constant. Tabular 3.1 demonstrates that in the presented steady-state mountain wave solution moisture significantly reduces momentum flux, for $\sigma = 0.75$ even about one order of magnitude.

Table 3.1.: *Vertical flux of horizontal momentum for different values of σ in the constant coefficient, steady-state solution with Witch of Agnesi topography.*

σ	*Momentum flux in* Nm^{-2}
0	-0.089
0.1	-0.075
0.5	-0.027
0.75	-0.007

3.5. Critical Layers

The equation for the vertical wave number (3.71) reveals that if there exists a height z_c where

$$\left(u^{\infty}-c\right)^2 k^2 - \sigma(z_{\mathrm{c}})\Theta^{(2)}_z = 0 \Leftrightarrow \sigma_{\mathrm{c}} := \sigma(z_{\mathrm{c}}) = \frac{\left(u^{\infty}-c\right)^2 k^2}{\Theta^{(2)}_z}, \tag{3.99}$$

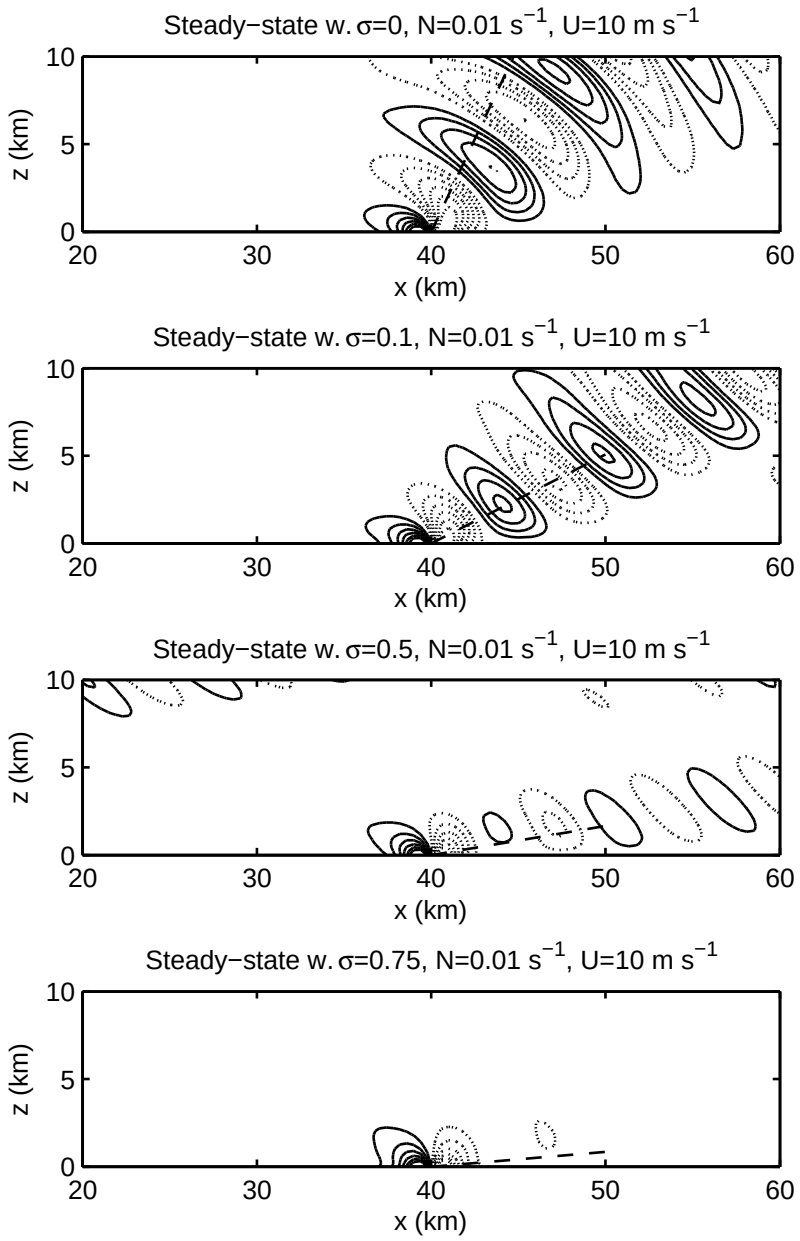

Figure 3.12.: *Steady-state orographic wave excited by a Witch of Agnesi topography. Shown are isolines of vertical velocity in steps of* $0.25\ m\ s^{-1}$*. Dotted lines represent negative values. The dashed line represents the averaged slope of the group velocity.*

then

$$\lim_{z \to z_\mathrm{c}} m(z_\mathrm{c}) \to \infty \tag{3.100}$$

i.e. the vertical wave number diverges to infinity, indicating a critical layer. In the dry case without shear, critical layers arise if at some height the horizontal phase speed c approaches the velocity of the background flow u^∞, see section 7.2 in [Büh09] or section 4.6 in [Lig78] for an analysis of this type of critical layer. In the moist model (2.70) however a critical layer can also arise in case of constant phase velocity $c \neq u^\infty$ if $\sigma \to \sigma_\mathrm{c}$.

Assuming constant stratification $\Theta_z^{(2)}$ allows to derive an approximate solution in the vicinity of z_c, using techniques described for the dry case in section 7.2 in [Büh09]. Introduce a new coordinate

$$s := \frac{z - z_\mathrm{c}}{\nu} \tag{3.101}$$

whereas ν is a measure of the width of the critical layer around z_c. Assuming that σ is linear around the critical layer yields

$$\sigma(z) = \sigma(z_\mathrm{c}) + (z - z_\mathrm{c}) \left.\frac{\partial \sigma}{\partial z}\right|_{z=z_\mathrm{c}} = \frac{\left(u^\infty - c\right)^2 k^2}{\Theta_z^{(2)}} + \nu s \left.\frac{\partial \sigma}{\partial z}\right|_{z=z_\mathrm{c}}. \tag{3.102}$$

In order for the limit

$$\left.\frac{\partial \sigma}{\partial z}\right|_{z=z_\mathrm{c}} = \lim_{z \to z_\mathrm{c}} \frac{\partial \sigma}{\partial z} = \lim_{z \to z_\mathrm{c}} \nu^{-1} \frac{\partial \sigma}{\partial s} \tag{3.103}$$

to exist, require

$$\frac{\partial \sigma}{\partial s} = \mathcal{O}(\nu^\alpha) \quad \text{and} \quad \frac{\partial \sigma}{\partial z} = \mathcal{O}(\nu^{\alpha-1}) \quad \text{for } \nu \to 0 \tag{3.104}$$

for some $\alpha > 1$. For simplicity, set $\alpha = 2$ so

$$\frac{\partial \sigma}{\partial z} = \nu\lambda \quad \text{with} \quad \lambda = \mathcal{O}(1) \quad \text{for } \nu \to 0. \tag{3.105}$$

Note that if $\lambda < 0$, i.e. $\sigma > \sigma(z_\mathrm{c})$ below the critical layer, the horizontal wave number k is below the cut-off k_low in (3.74). Thus the solution is evanescent below the critical layer and propagates above it. For $\lambda > 0$, the solution propagates below the layer and is evanescent above.

By inserting (3.105), (3.102) becomes

$$\sigma(z) = \frac{\left(u^\infty - c\right)^2 k^2}{\Theta_z^{(2)}} + \nu^2 \lambda s \tag{3.106}$$

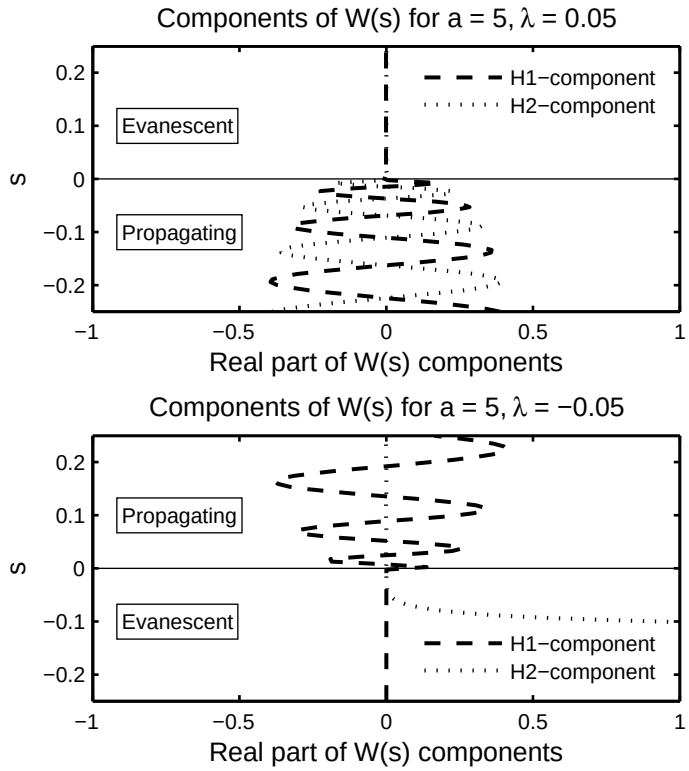

Figure 3.13.: *Qualitative behavior of the two components of* $W(s)$ *for positive* (upper) *and negative* (lower) λ.

and inserting this in the Taylor-Goldstein equation (3.70), employing $\partial_{zz} = \nu^{-2}\partial_{ss}$, yields

$$-\left[\frac{\Theta_z^{(2)} - (u^\infty - c)^2 k^2}{\nu^2 \lambda s \Theta_z^{(2)}} k^2 + \frac{1}{4}\right] \hat{w}(s) + \nu^{-2} \hat{w}_{ss}(s) = 0. \tag{3.107}$$

The leading order equation in the limit $\nu \to 0$ reads

$$\frac{\Theta_z^{(2)} - (u^\infty - c)^2 k^2}{\lambda \Theta_z^{(2)}} k^2 W(s) - s\lambda W_{ss}(s) = 0. \tag{3.108}$$

Abbreviating

$$a := \frac{\Theta_z^{(2)} - (u^\infty - c)^2 k^2}{\lambda \Theta_z^{(2)}} k^2 \tag{3.109}$$

solutions of (3.108), obtained using *dsolve* in MAPLE, read

$$W(s) = C_1 \sqrt{s} H_1^{(1)}\left(2\sqrt{-as}\right) + C_2 \sqrt{s} H_1^{(2)}\left(2\sqrt{-as}\right) \tag{3.110}$$

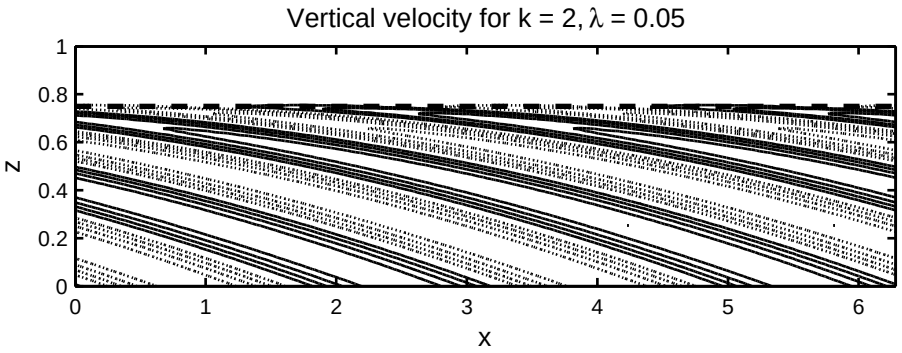

Figure 3.14.: *Vertical velocity in arbitrary units for a* $k = 2$ *sine topography,* $u^\infty = 0.1$*,* $\sqrt{\Theta_z^{(2)}} = 1$ *and a critical layer at* $z_c = 0.75$ *with* $\lambda = 0.05$*.*

whereas $H_1^{(1)}$, $H_1^{(2)}$ are Hankel functions of first and second kind of order one, see [AS65]. Figure 3.13 illustrates the qualitative behavior of the two components of $W(s)$ for positive and negative λ. The coefficients C_1, C_2 are set arbitrarily to obtain identifiable solutions for the employed axes. As discussed above, for $\lambda > 0$ (upper figure) both solution components are oscillatory below the critical height and decay above it, providing a small evanescent contribution. Thus the solution does not "stop" exactly at the layer but decays exponentially in a small region on top of it. For $\lambda < 0$ (lower figure), both components oscillate above the layer. However, for the chosen coefficients the amplitude of the $H^{(2)}$ component is small and not noticeable in the figure. The $H^{(1)}$ (dashed line) has non-zero amplitude at the layer and decays approaching $z = 0$. In contrast, the $H^{(2)}$ component (dotted line) has a non-zero amplitude at $z = 0$ and decays towards the critical layer.

Figure 3.14 shows the x-z-slice solution, obtained by inserting the vertical profile $W(s)$ given by (3.110) into the ansatz (3.79) featuring only a single mode with wave number $k = 2$ for $c = 0$, $u^\infty = 0.1$, $\sqrt{\Theta_z^{(2)}} = 1$ and $\lambda = 0.05$. As the vertical wave number increases towards the critical height set to $z_c = 0.75$, the phase lines are bent towards the horizontal. The critical layer effectively inhibits wave propagation and only a weak and quickly decaying contribution is noticeable in a small region above z_c. The upper figure in 3.16 shows the resulting vertical profile of mean momentum flux, revealing that momentum flux is completely blocked by the critical layer. Both figures use arbitrary units. To obtain a solution with physically meaningful amplitudes, W would have to be matched to far-field solutions above and below the critical layer.

An analogous solution with $\sigma > \sigma(z_c)$ below the critical layer and $\sigma < \sigma(z_c)$ above it, i.e. $\lambda < 0$, is shown in figure 3.15 with $z_c = 0.1$ (upper) and $z_c = 0.75$ (lower). All other values remain unchanged. In the upper figure, an evanescent mode is present below the critical layer. As values of W at z_c are small but non-zero, a

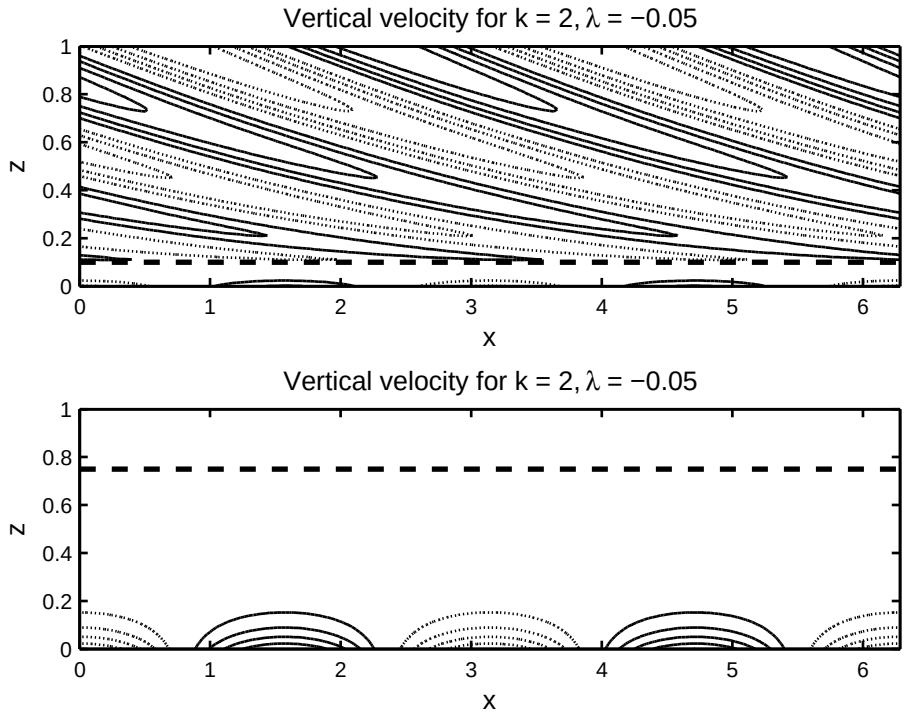

Figure 3.15.: *Vertical velocity in arbitrary units for a solution with a single horizontal mode with wavenumber* $k = 2$, $u^{\infty} = 0.1$, $\sqrt{\Theta_z^{(2)}} = 1$ *and a critical layer at* $z_c = 0.1$ (upper) *and* $z_c = 0.75$ (lower) *with* $\lambda = -0.05$.

noticeable propagating wave response is excited in the region above z_c, with phase lines bending towards the vertical as m decreases away from z_c. The lower figure in 3.16 shows the resulting momentum flux. It is very small in the evanescent region, but not zero. Its magnitude greatly increases above the critical layer in the propagating region.

In the lower figure in 3.15, the critical height is increased to $z_c = 0.75$, enlarging the region where the solution is evanescent. Thus the amplitude of W at z_c decreases, thus reducing the amplitude of the oscillation excited above the layer. In the presented example, the amplitude is too small to occur in the employed isolines.

As stated above, to obtain solutions with physically meaningful amplitudes, the critical layer solution would have to be matched to correct far-field solutions above and below the layer. This is not done here, but the qualitative behavior of solutions in the presence of critical layers described in this paragraph is partly confirmed by non-stationary simulations in chapter 5, using a sinusoidal topography as in subsection 3.4.1 to excite the $k = 2$ mode.

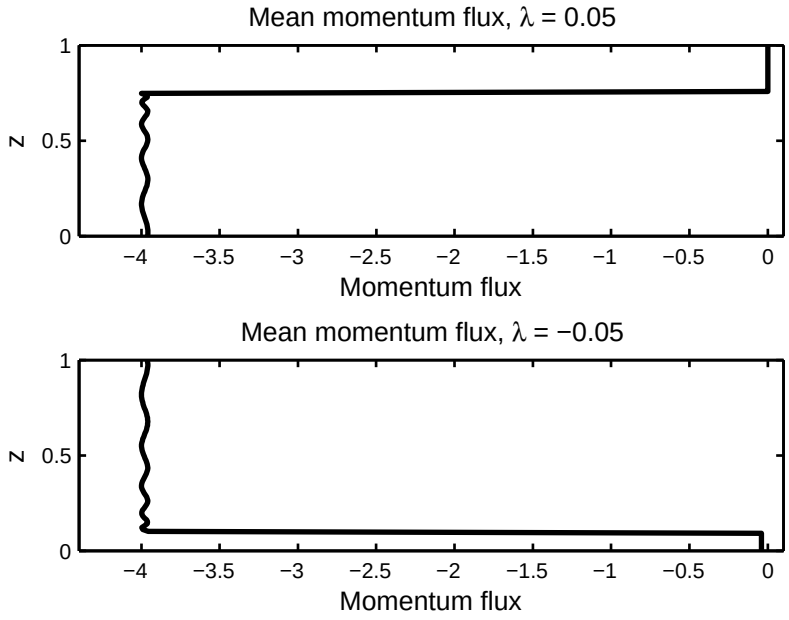

Figure 3.16.: *Mean momentum flux for solution shown in figure 3.14* (upper) *and 3.15 with* $z_c = 0.1$ (lower) *in arbitrary units.*

Chapter 4.

Numerical Scheme

This chapter presents the numerical scheme employed to obtain discrete, approximate solutions of (2.70). Section 4.1 discusses the timestepping scheme, section 4.2 describes the spatial mesh while section 4.3 presents the discrete approximations of the spatial derivatives. To realize a radiation condition at the upper boundary, a damping layer described in section 4.4 is employed. Finally, section 4.5 presents a few test cases.

4.1. Timestepping

Because of the anelastic constraint $(2.70)_4$, (2.70) is not purely hyperbolic, but of mixed hyperbolic-elliptic type. A projection method is employed to compute numerical solutions. Schemes of this type are widely used, see the citations in [VK09], and are based on the fundamental work of [Cho67]. They consist of a predictor step, advancing the velocity field in time neglecting the elliptic constraint, and a projection step, projecting the predicted velocity field onto the space of vector fields satisfying the constraint.

For (2.70), the predictor step advances the non pressure-related terms in time while the projection step yields the pressure gradients. [Dur91] analyzes the applicability of a multi-step Adams-Bashforth scheme in time in combination with a fourth order central difference scheme for spatial derivatives to advection problems and finds it a viable alternative to commonly used leapfrog schemes. Applied to an equation

$$\phi_\tau = F(\phi) \tag{4.1}$$

the Adam-Bashforth-3 scheme reads

$$\phi^{n+1} = \phi^n + \frac{\Delta\tau}{12}\left(23F(\phi^n) - 16F(\phi^{n-1}) + 5F(\phi^{n-2})\right). \tag{4.2}$$

The scheme exhibits slight numerical damping. Applying (4.2) to the oscillation test equation

$$\phi_\tau = i\kappa\phi \tag{4.3}$$

results in an amplification factor of

$$A = 1 - (\kappa \Delta\tau)^4 . \tag{4.4}$$

See [Dur99] for the details. Introducing weak numerical dissipation is considered acceptable here for gaining a higher order in time.

A drawback of a multi-level scheme like (4.2) is the requirement to store data from three time-levels. For the two-dimensional problems investigated in the present thesis however, memory requirements are not an issue.

To streamline notation define

$$\begin{aligned}
F_u^n &:= -u^\infty u_x^n \\
F_{\bar{w}}^n &:= -u^\infty \bar{w}_x^n + \bar{\theta}^n \\
F_{\bar{\theta}}^n &:= -u^\infty \bar{\theta}_x^n - \bar{w}^n (1-\sigma)\, \Theta_z^{(2)} + (w')^n \Theta_z^{(2)} + \bar{C}_-^n \\
F_{w'}^n &:= -u^\infty (w')_x^n + (\theta')^n \\
F_{\theta'}^n &:= -u^\infty (\theta')_x^n - \sigma \Theta_z^{(2)} + \sigma(1-\sigma)\Theta_z^{(2)} \bar{w}^n - \sigma \bar{C}_-^n
\end{aligned} \tag{4.5}$$

whereas the superscript n denotes the approximation of a quantity on some temporal mesh $\{\tau_0, \tau_1, \ldots, \tau_{N_\tau}\}$ at time τ_n. Applying (4.2) to (2.70) yields the semi-discrete system

$$\begin{aligned}
u^{n+1} &= u^n + \frac{\Delta\tau}{12}\left(23F_u^n - 16F_u^{n-1} + 5F_u^{n-2}\right) - \frac{\Delta\tau}{12}\left(23\pi_x^n - 16\pi_x^{n-1} + 5\pi_x^{n-2}\right) \\
\bar{w}^{n+1} &= \bar{w}^n + \frac{\Delta\tau}{12}\left(23F_{\bar{w}}^n - 16F_{\bar{w}}^{n-1} + 5F_{\bar{w}}^{n-2}\right) - \frac{\Delta\tau}{12}\left(23\pi_z^n - 16\pi_z^{n-1} + 5\pi_z^{n-2}\right) \\
\bar{\theta}^{n+1} &= \bar{\theta}^n + \frac{\Delta\tau}{12}\left(23F_{\bar{\theta}}^n - 16F_{\bar{\theta}}^{n-1} + 5F_{\bar{\theta}}^{n-2}\right) \\
(w')^{n+1} &= (w')^n + \frac{\Delta\tau}{12}\left(23F_{w'}^n - 16F_{w'}^{n-1} + 5F_{w'}^{n-2}\right) \\
(\theta')^{n+1} &= (\theta')^n + \frac{\Delta\tau}{12}\left(23F_{\theta'}^n - 16F_{\theta'}^{n-1} + 5F_{\theta'}^{n-2}\right) .
\end{aligned} \tag{4.6}$$

whereas $\Delta\tau$ is the length of one timestep and assumed to be constant, i.e

$$\Delta\tau = \tau_n - \tau_{n-1} \quad \text{for } n = 1, \ldots, N_\tau. \tag{4.7}$$

Further, an equation for the pressure π^n is required. Define the predictor velocity field as

$$\begin{aligned}
u^{*,n} &:= u^n + \frac{\Delta\tau}{12}\left(23F_u^n - 16F_u^{n-1} + 5F_u^{n-2}\right) - \frac{\Delta\tau}{12}\left(-16\pi_x^{n-1} + 5\pi_x^{n-2}\right) \\
w^{*,n} &:= \bar{w}^n + \frac{\Delta\tau}{12}\left(23F_{\bar{w}}^n - 16F_{\bar{w}}^{n-1} + 5F_{\bar{w}}^{n-2}\right) - \frac{\Delta\tau}{12}\left(-16\pi_z^{n-1} + 5\pi_z^{n-2}\right)
\end{aligned} \tag{4.8}$$

so that by construction

$$\begin{aligned} u^{n+1} &= u^{*,n} - \frac{23\Delta\tau}{12}\pi_x^n \\ \bar{w}^{n+1} &= \bar{w}^{*,n} - \frac{23\Delta\tau}{12}\pi_z^n. \end{aligned} \tag{4.9}$$

Denoting $\nabla := (\partial_x, \partial_z)$ and applying $\partial_x\rho^{(0)}$ to $(4.9)_1$, $\partial_z\rho^{(0)}$ to $(4.9)_2$, summing both equations and using that by $(2.70)_4$

$$\nabla \cdot \left(\rho^{(0)}(u^{n+1}, \bar{w}^{n+1})^{\mathrm{T}}\right) = 0 \tag{4.10}$$

results in the elliptic equation

$$\nabla \cdot \left[\rho^{(0)}\nabla\left(\frac{23\Delta\tau}{12}\pi^n\right)\right] = \nabla \cdot \left(\rho^{(0)}(u^{*,n}, \bar{w}^{*,n})^{\mathrm{T}}\right). \tag{4.11}$$

This equation has to be solved in every timestep for π^n to compute the projection step (4.9).

4.2. Description of the Mesh

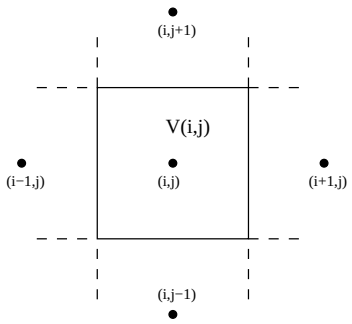

Figure 4.1.: *Indexing of primary cells.*

The two-dimensional Cartesian mesh used in all numerical simulations in this thesis consists of a set of primary and a set of dual cells. The mesh and the discrete spatial operators used in the projection step are described and analyzed in [Vat05, VK09]. Let the full domain be a rectangle in the two-dimensional plane, i.e.

$$\Omega = [x_{\mathrm{l}}, x_{\mathrm{r}}] \times [0, z_{\mathrm{up}}] \subset \mathbb{R}^2. \tag{4.12}$$

The primary discretization consists of rectangular cells with constant width Δx and constant height Δz. The cells are indexed from $(1, 1)$, the lower left cell, to (N_x, N_z), the upper right. N_x is the number of cells in a row, N_z the number of

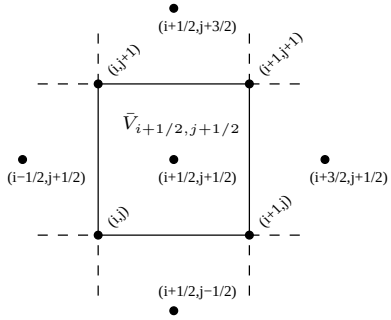

Figure 4.2.: *Indexing of dual cells.*

cells in a column. The coordinates of the center of a cell V with index (i, j) are labeled (x_i, z_j). Thus

$$V_{i,j} = \left[x_i - \frac{\Delta x}{2}, x_i + \frac{\Delta x}{2}\right] \times \left[z_j - \frac{\Delta z}{2}, z_j + \frac{\Delta z}{2}\right]. \tag{4.13}$$

Figure 4.1 sketches a primary cell.

Velocities $u, \bar{w}, w'$ and potential temperatures $\bar{\theta}, \theta'$ "live" on this primary grid. The pressure π, however, "lives" on the dual cells. The discrete gradient operator introduced below maps the pressure π to the discrete gradient $\nabla\pi$, which "lives" again on the primary cells.

Label the coordinates of the four corners of a primary cell $V_{i,j}$ by $(x_{i-1/2}, z_{j-1/2})$, $(x_{i+1/2}, z_{j-1/2})$, $(x_{i-1/2}, z_{j+1/2})$ and $(x_{i+1/2}, z_{j+1/2})$, denoting lower left, lower right, upper left and upper right corner. The dual cell $\bar{V}_{i+1/2,j+1/2}$ is the rectangle

$$\bar{V}_{i+1/2,j+1/2} = [x_i, x_{i+1}] \times [z_j, z_{j+1}] \tag{4.14}$$

with center $(x_{i+1/2}, z_{j+1/2})$, cf. figure 4.2. The discretization consists of the set of all primary cells

$$\mathcal{V} = \{V_{i,j} : 1 \le i \le N_x, 1 \le j \le N_z\} \tag{4.15}$$

and the set of all dual cells

$$\bar{\mathcal{V}} = \left\{\bar{V}_{i+1/2,j+1/2} : 0 \le i \le N_x, 0 \le j \le N_z\right\}. \tag{4.16}$$

An example of a complete mesh is sketched in figure 4.3.

In subsection 4.3.2 discrete operators on these grids are defined that allow to formulate and solve a discrete version of the advection or predictor step consisting of $(4.6)_{3-5}$ to advance $\bar{\theta}$, w' and θ' in time as well as (4.8) to compute the predicted velocity, the elliptic problem (4.11) and finally the correction step (4.9).

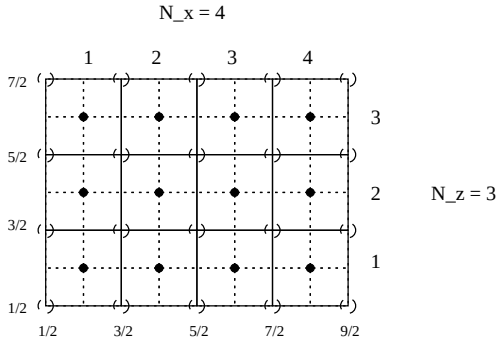

Figure 4.3.: *Example of a full mesh with $N_x = 4$ and $N_z = 3$. Dashed cells form the dual mesh. Numbers at the sides denote the indices of corresponding x and z coordinates.*

4.3. Discrete Spatial Derivatives

4.3.1. Advection

The gradient in the advection part is discretized by a fourth order central difference scheme

$$\frac{\partial \phi(x_i)}{\partial x} \approx \frac{4}{3}\left(\frac{\phi_{i+1} - \phi_{i-1}}{2\Delta x}\right) - \frac{1}{3}\left(\frac{\phi_{i+2} - \phi_{i-2}}{4\Delta x}\right) \tag{4.17}$$

whereas ϕ_i denotes the value of a quantity ϕ at the center of some primary cell $V_{i,j}$ while Δx is the distance $x_{i+1} - x_i = x_i - x_{i-i}$. The presented simulations use equidistant meshes in x and z, respectively, so Δx does not depend on the index i. See [Dur91, Dur99] for a detailed analysis of the properties of this scheme. As the advective step does not involve π, only values "living" on the primary cells occur.

4.3.2. Projection

Ansatz Spaces

As described in section 4.1 to compute the projection (4.9) of the velocity field, the Poisson problem (4.11) has to be solved for π. The Finite-Element discretization analyzed in [Vat05, VK09] is adopted here, with a slight modification to include the density $\rho^{(0)}$. The constant factor arising from the time discretization is included in π to streamline the notation. Multiplying (4.11) by a test function q and integrating over Ω yields the variational equation

$$\int_\Omega \nabla \cdot \left(\rho^{(0)} \nabla \pi\right) q \; dxdz = \int_\Omega \nabla \cdot \left(\rho^{(0)} \mathbf{v}^*\right) q \; dxdz \tag{4.18}$$

whereas $\mathbf{v}^* = (u^*, w^*)$ is the velocity field computed in the predictor step (4.8). Following [VK09], the space of test functions is chosen as the space of all functions that are constant on the *dual* cells $\bar{V}_{i+1/2,j+1/2}$, i.e.

$$q \in \mathcal{T}^h := \left\{ q \in L^2(\Omega) : q|_{\bar{V}} = const.\ \forall\ \bar{V} \in \bar{\mathcal{V}} \right\}. \tag{4.19}$$

The characteristic functions of the dual cells $\mathbf{1}_{\bar{V}}$ constitute a basis of this space. The pressure π is assumed to be bilinear on each primary cell V and globally continuous. For $U \subset \mathbb{R}^2$, denote by $\mathcal{Q}_k(U)$ the space of all polynomials on U of degree $\leq k$ with respect to x and z respectively. Then

$$\pi \in \mathcal{H}^h = \left\{ p \in H^1(\Omega) \backslash \mathbb{R} : p|_V \in \mathcal{Q}_1(V)\ \forall\ V \in \mathcal{V} \right\}. \tag{4.20}$$

Functions differing only by a constant are treated as identical here, to ensure the existence of a unique solution of (4.11) with Neumann boundary conditions. As the essential quantity in the projection (4.9) is the gradient $\nabla\pi$, additive constants are irrelevant. The gradient of functions in $\mathcal{H}^h$ is piecewise linear on each primary cell but discontinuous across the interfaces. The space of functions of this type is used as ansatz space for the velocity fields

$$\mathbf{v} \in \mathcal{U}^h = \left\{ \mathbf{v} = (u, w) \in \left[L^2(\Omega) \right]^2 : u|_V, w|_V \in \mathcal{P}_1(V)\ \forall\ V \in \mathcal{V} \right\} \tag{4.21}$$

whereas $\mathcal{P}_1(V)$ denotes the space of polynomials of order one (=linear functions) on V.

The density $\rho^{(0)}$ given by (3.44) is a prescribed function in (4.11), depending on z only. It is approximated by a function $\rho_{\mathrm{p}}^{(0)}$, piecewise constant on primary cells, whereas the constant value ρ_j for a cell $V_{i,j}$ is obtained by evaluating $\rho^{(0)}$ at the cell center. Thus the products $\rho_{\mathrm{p}}^{(0)} \nabla\pi$ and $\rho_{\mathrm{p}}^{(0)} \mathbf{u}$ are still in the space $\mathcal{U}^h$. For higher order approximations of the density, for example piecewise linear, this would not be the case.

Discrete Operators

Having introduced the ansatz spaces for the different quantities, the discrete Laplacian can be defined

$$L : \mathcal{H}^h \to \mathcal{T}^h\ , \quad L(\pi) := \sum_{\bar{V} \in \bar{\mathcal{V}}} \mathbf{1}_{\bar{V}} \frac{1}{|\bar{V}|} \int_{\partial \bar{V}} \left(\rho_{\mathrm{p}}^{(0)} \nabla\pi \right) \cdot \mathbf{n}\ d\sigma \tag{4.22}$$

as well as the discrete divergence

$$D : \mathcal{U}^h \to \mathcal{T}^h\ , \quad D(\mathbf{v}) := \sum_{\bar{V} \in \bar{\mathcal{V}}} \mathbf{1}_{\bar{V}} \frac{1}{|\bar{V}|} \int_{\partial \bar{V}} \left(\rho_{\mathrm{p}}^{(0)} \mathbf{v} \right) \cdot \mathbf{n}\ d\sigma. \tag{4.23}$$

Functions in $\mathcal{H}^h$ can be represented on a primary cell as

$$\pi(x,z)|_{V_{i,j}} = \pi_{i,j} + (x-x_i)\,\pi_{x,i,j} + (z-z_j)\,\pi_{z,i,j} + (x-x_i)\,(z-z_j)\,\pi_{xz,i,j} \quad (4.24)$$

and thus, their gradient can be computed analytically

$$\nabla\pi(x,z)|_{V_{i,j}} = \begin{pmatrix} \pi_{x,i,j} + (z-z_j)\,\pi_{xz,i,j} \\ \pi_{z,i,j} + (x-x_i)\,\pi_{xz,i,j} \end{pmatrix}. \quad (4.25)$$

As the pressure π is determined by values living at the centers of *dual* cells, the slopes have to be constructed from these values. Defining

$$\begin{aligned} \pi_{x,i,j} &:= \frac{1}{2\Delta x}\left(\pi_{i+1/2,j+1/2} - \pi_{i-1/2,j+1/2} + \pi_{i+1/2,j-1/2} - \pi_{i-1/2,j-1/2}\right) \\ \pi_{z,i,j} &:= \frac{1}{2\Delta z}\left(\pi_{i+1/2,j+1/2} - \pi_{i+1/2,j-1/2} + \pi_{i-1/2,j+1/2} - \pi_{i-1/2,j-1/2}\right) \\ \pi_{xz,i,j} &:= \frac{1}{\Delta x\Delta z}\left(\pi_{i+1/2,j+1/2} - \pi_{i-1/2,j+1/2} - \pi_{i+1/2,j-1/2} + \pi_{i-1/2,j-1/2}\right) \end{aligned} \quad (4.26)$$

allows to introduce a discrete gradient

$$G : \mathcal{H}^h \to \mathcal{U}^h\ , \quad G(\pi) := \nabla\pi. \quad (4.27)$$

As their continuous counterparts, the operators (4.22), (4.23) and (4.27) satisfy

$$L = D \circ G \quad (4.28)$$

so the obtained projection is exactly satisfying the constraint $(2.70)_4$, not only up to the accuracy of the discretization, cf. [VK09].

Stencils

For the Cartesian, two-dimensional mesh described in section 4.2 the integrals in (4.22), (4.23) and (4.27) can be computed analytically. For a function $\mathbf{v} = (u,w) \in \mathcal{U}^h$, represented on a a primary cell $V_{i,j}$ as

$$(u,w)\,|_{V_{i,j}} = (u_{i,j}, w_{i,j}) + (x-x_j)\,(u_{x,i,j}, w_{x,i,j}) + (z-z_j)\,(u_{z,i,j}, w_{z,i,j}) \quad (4.29)$$

the boundary integrals arising in (4.23) can be evaluated by

$$\begin{aligned} &\frac{1}{|\bar{V}_{i+1/2,j+1/2}|}\int_{\partial\bar{V}_{i+1/2,j+1/2}} \left(\rho_{\mathrm{p}}^{(0)}\mathbf{v}\right)\cdot\mathbf{n}\ d\sigma = \\ &\frac{1}{2\Delta z}\left(\rho_{j+1}w_{i,j+1} - \rho_j w_{i,j} + \rho_{j+1}w_{i+1,j+1} - \rho_j w_{i+1,j}\right) \\ +&\frac{\Delta x}{8\Delta z}\left(\rho_{j+1}w_{x,i,j+1} - \rho_j w_{x,i,j} - \rho_{j+1}w_{x,i+1,j+1} + \rho_j w_{x,i+1,j}\right) \\ +&\frac{1}{2\Delta x}\left(\rho_{j+1}\left(u_{i+1,j+1} - u_{i,j+1}\right) + \rho_j\left(u_{i+1,j} - u_{i,j}\right)\right) \\ +&\frac{\Delta z}{8\Delta x}\left(-\rho_{j+1}\left(u_{z,i+1,j+1} - u_{z,i,j+1}\right) + \rho_j\left(u_{z,i+1,j} - u_{z,i,j}\right)\right). \end{aligned} \quad (4.30)$$

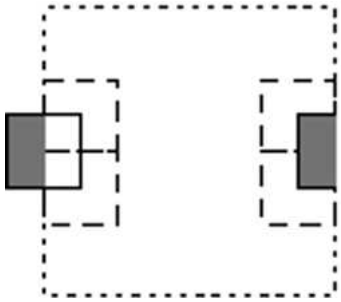

Figure 4.4.: *Periodic boundary conditions: The dotted line is the boundary of the domain Ω. The dashed lines mark two primary cells at the boundary. Solutions coincide on the shaded regions. Approximately redrawn from [Vat05].*

Inserting (4.26) and (4.25) in (4.23) yields a compact, nine point stencil for the discrete Laplacian

$$\begin{aligned}
&\frac{1}{|\bar{V}_{i+1/2,j+1/2}|}\int_{\partial\bar{V}_{i+1/2,j+1/2}}\left(\rho_{\mathrm{p}}^{(0)}\nabla\pi\right)\cdot\mathbf{n}\;d\sigma = \\
&\frac{1}{8}\rho_{j+1}\Delta_{xx,i+1/2,j+3/2}+\frac{6}{8}\left(\frac{\rho_{j+1}+\rho_j}{2}\right)\Delta_{xx,i+1/2,j+1/2} \\
&\quad+\frac{1}{8}\rho_j\Delta_{xx,i+1/2,j-1/2} \\
&+\frac{1}{8}\Delta^{\rho}_{zz,i+3/2,j+1/2}+\frac{6}{8}\Delta^{\rho}_{zz,i+1/2,j+1/2}+\frac{1}{8}\Delta^{\rho}_{zz,i-1/2,j+1/2}
\end{aligned} \tag{4.31}$$

whereas

$$\Delta_{xx,i+1/2,j+1/2} := \frac{1}{\Delta x^2}\left(\pi_{i+3/2,j+1/2}-2\pi_{i+1/2,j+1/2}+\pi_{i-1/2,j+1/2}\right) \tag{4.32}$$

and

$$\begin{aligned}
\Delta^{\rho}_{zz,i+1/2,j+1/2} := \frac{1}{\Delta z^2}\big(&\rho_{j+1}\pi_{i+1/2,j+3/2}-(\rho_{j+1}+\rho_j)\,\pi_{i+1/2,j+1/2} \\
&+\rho_j\pi_{i+1/2,j-1/2}\big)
\end{aligned} \tag{4.33}$$

can be interpreted as approximations to the second order horizontal and vertical derivative. Setting $\rho_j = 1$ for all j reproduces the expressions derived in [Vat05, VK09].

Boundary Conditions

Boundary conditions are required to complete the stencil, as the dual cells at the boundary are partly located outside the domain Ω. In the following, periodic

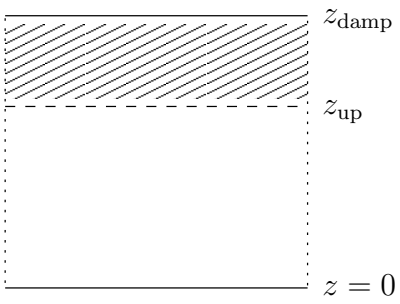

Figure 4.5.: *Addition of a damping layer (striped region) at the top of the domain.*

boundary conditions and homogeneous Neumann boundary conditions are used. Figure 4.4 sketches how periodic boundaries are employed. For Neumann boundary conditions, dual cells at the boundary have only half the size of cells inside the domain. The normal derivative along the boundary is set to zero, possible contributions from inhomogeneous Neumann boundary conditions like (3.78) are included in (4.11) as additional terms on the right hand side.

The damping layer described in section 4.4 emulates a transparent boundary condition, but at the top of the damping layer, a homogeneous Neumann condition is applied.

4.4. Damping Layer

At the upper boundary of the domain a transparent boundary condition allowing energy to leave the domain is required, see [KD82, Bou83]. For the non-hydrostatic case, no exact local formulation of this boundary condition exists, so a Rayleigh damping layer as described and analyzed in [KL78] for the nonlinear, hydrostatic case is employed. The computational domain Ω, given by (4.12), is extended by an additional layer

$$\Omega_{\text{damp}} := [x_{\text{l}}, x_{\text{r}}] \times [z_{\text{up}}, z_{\text{damp}}] \tag{4.34}$$

placed on top of it, i.e. the domain actually used in a computation is

$$\Omega_{\text{Total}} = \Omega \cup \Omega_{\text{damp}} \tag{4.35}$$

see figure 4.5. Inside Ω_{damp}, relaxation terms are incorporated into the five prognostic equations in (2.70), causing a relaxation of the computed solutions to some prescribed background state. The modifications read

$$\phi_\tau = F(\phi) - \nu\,(\phi - \phi_0) \tag{4.36}$$

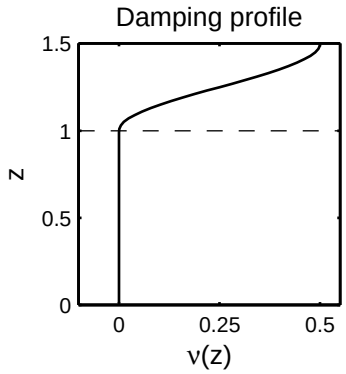

Figure 4.6.: *Vertical profile of the artificial viscosity $\nu(z)$. It is zero inside the original domain Ω and increases smoothly inside Ω_{damp} up to its maximum value $\nu_{\max}$ at z_{damp}.*

with $\phi \in \left\{u, \bar{w}, \bar{\theta}, w'.\theta'\right\}$ and $F(\phi)$ abbreviating remaining terms in the different equations in (2.70). The Rayleigh viscosity ν is a height dependent function, ensuring a smoothly increasing damping inside Ω_{damp} to avoid reflections by a sudden introduction of viscosity at the interface. ϕ_0 are the background states against which the solution is relaxed. As the unknowns in (2.70) denote perturbations, all ϕ_0 are set to zero in the following. For the damping profile, choose the function also used in [KL78]

$$\nu(z) = \begin{cases} 0 & : z < z_{\text{up}} \\ \nu_{\max} \sin^2\left(\frac{\pi}{2} \frac{z - z_{\text{up}}}{z_{\text{damp}} - z_{\text{up}}}\right) & : z \geq z_{\text{up}} \end{cases} . \tag{4.37}$$

This yields a smooth increase of viscosity from zero at z_{up} up to a maximum value of $\nu_{\max}$ at z_{damp}, cf. figure 4.6.

The parameter $\nu_{\max}$ has to be chosen according to the dominant horizontal wavenumber in the solution, cf. [KL78]. In simulations of orographic waves, the spectrum of the solution is determined by the topography, the stratification and the background flow. To find a suitable value $\nu_{\max}$ for waves excited by a Witch of Agnesi topography in (2.70), run the setup described in subsection 4.5.3 for range of different values of $\nu_{\max}$. Comparing the obtained solutions to a reference solution computed on a very high domain with $z_{\text{up}} = 4.5$ in which no waves reach the upper boundary, allows to estimate an optimal value for $\nu_{\max}$. Figure 4.7 shows the maximum error computed over the domain Ω without the damping layer depending on $\nu_{\max}$, suggesting that $\nu_{\max} = 0.5$ is a reasonable value for the given parameters.

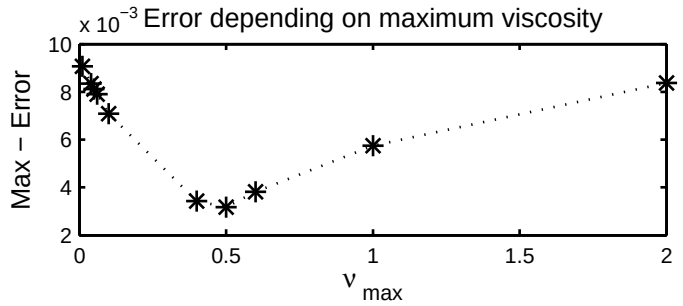

Figure 4.7.: *Maximum error over the computational domain measured against a reference solution depending on* $\nu_{\max}$.

4.5. Test Cases

4.5.1. Advection

In order to validate the implementation of the advection scheme, the projection step is turned off by arbitrarily setting $\pi^n = 0$ in every timestep. All initial data except $\bar{w}$ are set to zero. Choosing a profile for $\bar{w}$ that is constant with height and setting $\Theta_z^{(2)} = 0$ eliminates all vertical coupling, so the code just solves N_z independent horizontal advection problems. The results of the test problem described in [Dur91] are reproduced and the correct convergence order of the time-discretization (4.2) and the spatial discretization (4.17) are verified. The employed domain is $[0, 1]$ and the initial $\bar{w}$, adopted from [Dur91], reads

$$\bar{w}_0(x) = \begin{cases} \left[(8x-4)^2 - 1\right]^2 & : 3/8 \le x \le 5/8 \\ 0 & : \quad \text{otherwise} \end{cases} . \tag{4.38}$$

Initial values for $\bar{w}^{-1}$ and $\bar{w}^{-2}$ are obtained analytically by evaluating (4.38) for $x + u^\infty \Delta\tau$ and $x + 2u^\infty \Delta\tau$. The simulation is run, employing periodic boundary conditions, until $\tau = 12$ with $u^\infty = 0.25$, corresponding to three complete cycles. The exact solution at $\tau = 12$ is again $\bar{w}_0$. $N_z = 5$ independent horizontal advection problems are solved and all produce, as expected, identical results.

Figure 4.8 shows the solution for $N_x = 32$ with Courant numbers of 0.5 and 0.2, while figure 4.9 shows the solution on a refined grid with $N_x = 64$ and identical Courant numbers, i.e. the timesteps are half as long. The generated solutions are identical to the ones shown in figures 5 & 6 in [Dur91].

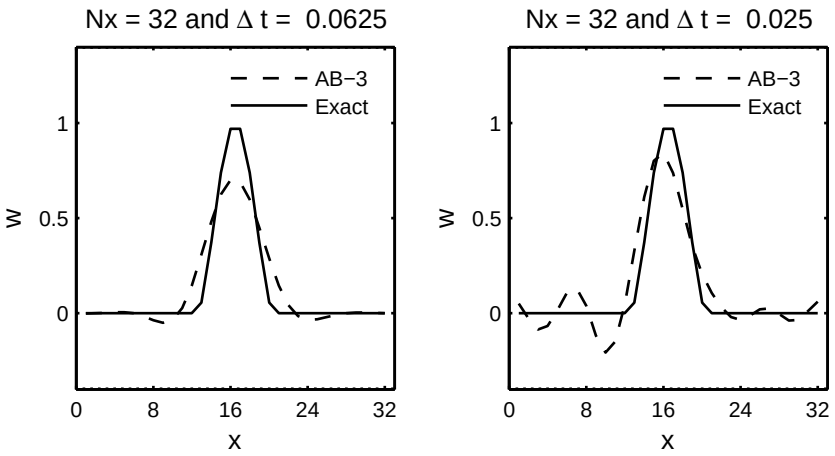

Figure 4.8.: *Advection test case for* $N_x = 32$ *with Courant numbers* 0.5 (left) *and* 0.2 (right).

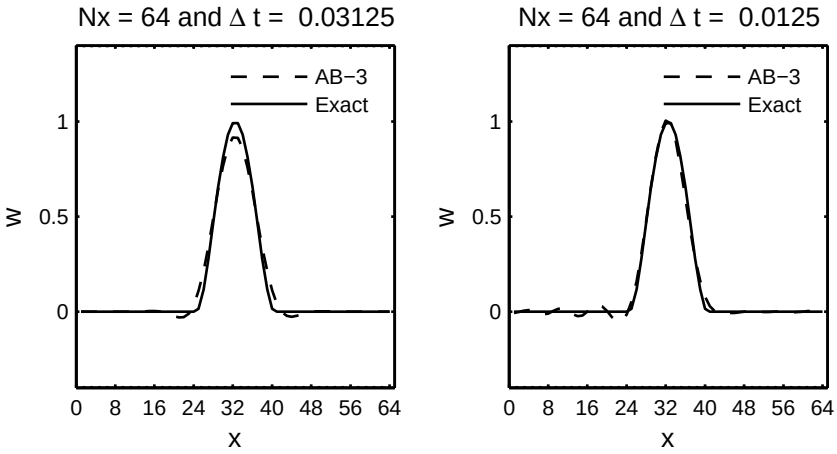

Figure 4.9.: *Advection test case for* $N_x = 64$ *with Courant numbers* 0.5 (left) *and* 0.2 (right).

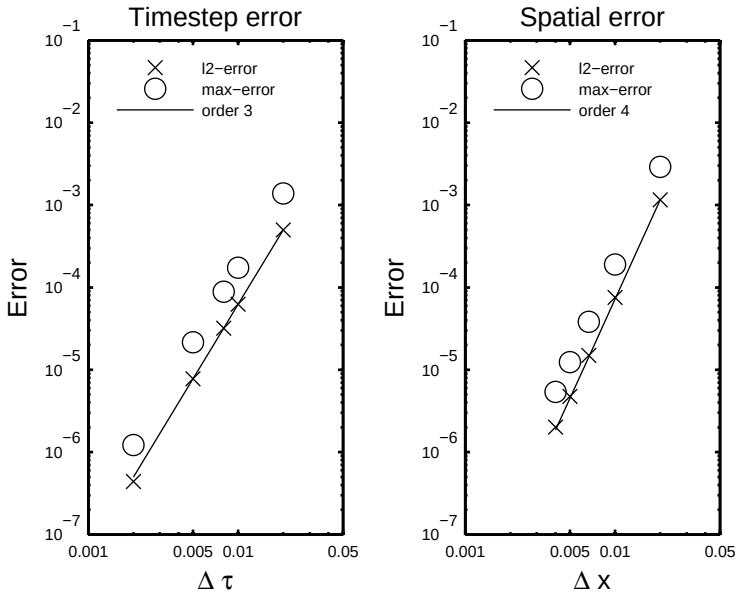

Figure 4.10.: *Convergence of the advection scheme in time* (left) *and space* (right). *The time error is measured against a reference solution on the same spatial grid with* $\Delta\tau = 0.001$ *while the spatial error is measured against the analytical solution.*

Convergence Orders

To verify that the implemented advection scheme features the expected convergence orders in time and space, a smooth initial gauss peak

$$\bar{w}_0(x) = \exp\left(-\frac{1}{2}\frac{(x-0.5)^2}{0.1^2}\right) \tag{4.39}$$

is advected with $u^\infty = 0.25$ until $\tau = 4$ with periodic boundaries in x. The exact analytical solution at $\tau = 4$ is again (4.39). The initial values w^{-1}, w^{-2} required for the multi-step scheme are obtained by evaluating (4.39) for $x + u^\infty\Delta\tau$ and $x + 2u^\infty\Delta\tau$.

In order to asses the rate of convergence in $\Delta\tau$, the simulation is run for timesteps of length $\Delta\tau = 0.02$, 0.01, 0.008, 0.005, 0.002 and compared to a reference solution computed with $\Delta\tau = 0.001$. The Courant-Friedrichs-Lewy (CFL) stability criterion, see e.g. p. 45f in [Dur99], prevents a reasonable comparison against the analytic solution, because either Δx is too large and the spatial error dominates or, if Δx is reduced, the CFL condition is violated and the scheme is unstable.

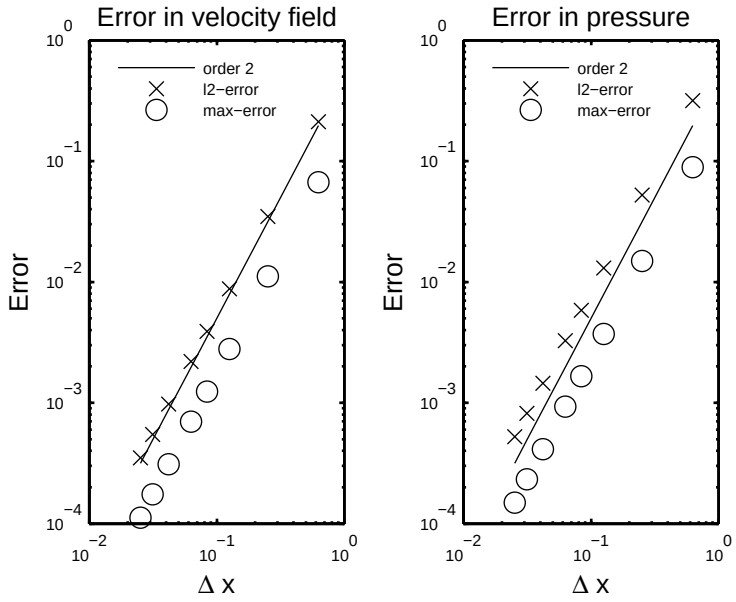

Figure 4.11.: *Convergence order of the projection step in the computed velocity field* (left) *and the computed pressure* (right).

In order to verify the convergence order of the spatial discretization, the advection problem is run for $N_x = 50$, 100, 200, 250 and the final discrete solution is compared to the analytical solution, evaluated on the respective grid points. Figure 4.10 shows l_2- and max-error for both cases. As expected, the advection scheme is third order accurate in time (left) and fourth order accurate in space (right).

4.5.2. Projection

An analytical test case[1] for constant density, i.e. $\rho^{(0)} = 1$, using periodic boundary conditions in all directions is employed to assess the convergence order of a full projection step. It employs a domain $[0, 2\pi] \times [0, 2\pi]$ and a "predicted" velocity field

$$\begin{aligned} u^* &= \sin(x)\sin(z) \\ w^* &= \sin(x)\cos(z). \end{aligned} \tag{4.40}$$

The corresponding Laplace problem reads

$$\nabla \cdot \nabla \pi = \cos(x)\sin(z) - \sin(x)\sin(z) \tag{4.41}$$

[1]Provided by Stefan Vater, private communication.

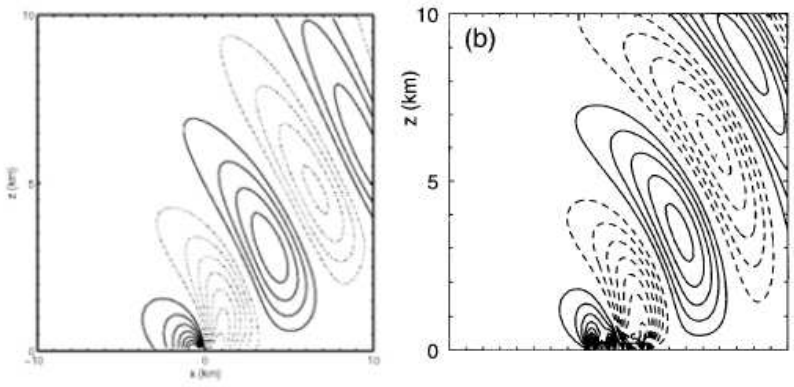

Figure 4.12.: *Vertical velocity* $\bar{w}$. *Interval between isolines is* 0.25 $m\ s^{-1}$, *dashed lines indicate negative values.* Left: *Solution at* $\tau = 21.6$ *computed with the linear code and* $\Delta z = 200$ m. Right: *Linear steady-state solution. Fig. 1b in [GK00].*

with solution

$$\pi(x,z) = \frac{1}{2}\left(\sin(x)\sin(z) - \cos(x)\sin(z)\right). \tag{4.42}$$

The resulting divergence free velocity reads

$$\begin{aligned} u &= \frac{1}{2}\left(\sin(x)\sin(z) - \cos(x)\sin(z)\right) \\ w &= \frac{1}{2}\left(\sin(x)\cos(z) - \cos(x)\cos(z)\right). \end{aligned} \tag{4.43}$$

Figure 4.11 shows the error in the computed velocity field (left) and the computed pressure (right) in the l_2- as well as in the max-norm. As expected, the scheme is second order accurate for velocity as well as pressure.

4.5.3. Mountain Wave Example

Finally, to demonstrate the ability of the code to produce reasonable solutions of the mountain wave problem, a setup described and investigated in [GK00] is solved. The domain in dimensional terms is $[-20\text{ km}, 20\text{ km}] \times [0, 9\text{ km}]$ plus a 6.6 km thick damping layer. The background flow is $U = 10\text{ m s}^{-1}$, the stability frequency is $N = 0.01\text{s}^{-1}$ and the topography reads

$$h(x) = \frac{H}{1 + \frac{x^2}{a^2}} \tag{4.44}$$

with $H = 400$ m and $a = 1$ km. In non-dimensional terms, this equals $u^\infty = 0.1$, $\sqrt{\Theta_z^{(2)}} = 1$ and a domain $[-2, 2] \times [0, 0.9]$ plus a 0.56 high damping layer, while the hill has a non-dimensional height of 0.04 and a width of 0.1. The horizontal and vertical resolution is $\Delta x = \Delta z = 0.02$ or 200 m. No timestep size is indicated in [GK00], for the linear code a timestep of $\Delta\tau = 0.05$ or 5 s is employed.

Figure 4.12 shows for comparison the time-dependent solution obtained with the linear code at time $\tau = 21.6$ and the linear steady-state solution presented in [GK00][2]. The time-dependent model exhibits considerably smaller amplitudes in higher regions. This is also observed for the nonlinear time-dependent solutions shown in 4.13 (right figures), thus partly the underestimation may be attributed to the fact that the solution is unsteady. Also the propagation angle of the wave pattern is slightly shallower. Nevertheless, the transient solution reproduces the qualitative features of the stationary wave pattern comparatively well.

Contrary to (2.70), the model solved in [GK00] is nonlinear and employs a step-terrain approximation of the topography instead of a linearized inflow boundary condition. For the values of N, H and U employed here, the parameter indicating the nonlinearity of the flow equals

$$\frac{NH}{U} = 0.4. \tag{4.45}$$

It is questionable whether 0.4 can be considered an order of magnitude smaller than unity. However, it turns out the effect of the nonlinearity is noticeable, but the linear solution still is in moderately good agreement with the nonlinear result. Figure 4.13 shows the results obtained with the linear code presented in this chapter (left) together with the corresponding results from [GK00] (right)[3]. The linear solutions exhibit noticeably reduced amplitudes, especially in the upper part of the domain. Also the propagation angle appears to be steeper in the nonlinear case. Nevertheless, the general wave pattern and the location of the extrema match reasonably well, confirming the result of the asymptotic derivation that linear leading order dynamics constitute a useful approximation.

[2] (c) American Meteorological Society. Reprinted with permission.
[3] (c) American Meteorological Society. Reprinted with permission.

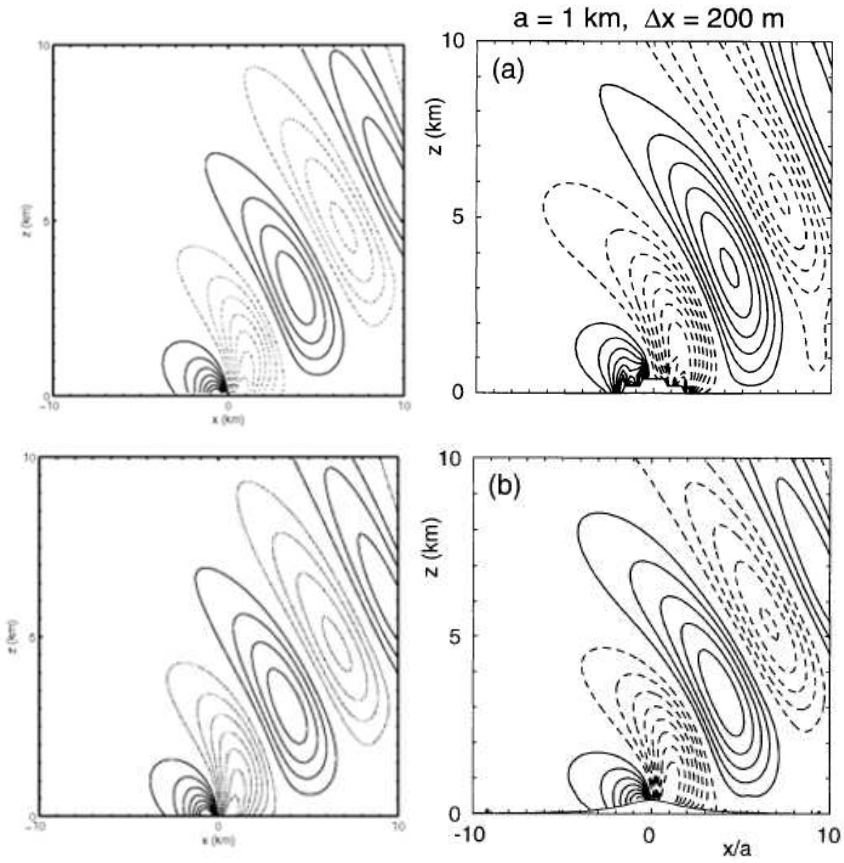

Figure 4.13.: *Isolines of dimensional vertical velocity in steps of* 0.25 $m\ s^{-1}$. *Dashed lines represent negative values.* Left: *Solutions from the linear code with* $\Delta z = 200\ m$ (upper) *and* $\Delta z = 10\ m$ (lower). Right: *Solutions from the nonlinear code analyzed in [GK00] with* $\Delta z = 200\ m$ (upper) *and* $\Delta z = 10\ m$ (lower). *Fig. 7 in [GK00].*

Chapter 5.

Numerical Results

This chapter presents several approximate solutions of the non-stationary model (2.70), computed with the scheme introduced and validated in chapter 4. Section 5.1 demonstrates for a simple example the ability of the non-stationary code to reproduce essential patterns of the stationary solutions analyzed in 3.4. The existence of a lower cut-off wave-number introduced by moisture, pointed out analytically for stationary solutions in subsection 3.3.5 and section 3.4, is confirmed for non-stationary solutions in section 5.2. Section 5.3 presents the simulation of a cloud-pattern advected through a mountain wave pattern. The inhibition of wave-propagation by moisture and the reduction of momentum flux are confirmed, as well as an amplification of up- and downdrafts inside the cloud-pattern. Section 5.4 confirms the qualitative behavior of solutions in the presence of critical layers, derived analytically in section 3.5. Section 5.6 demonstrates how large-scale gravity waves are excited by net tower-scale dynamics, including the generation of momentum flux. Evaporating rain also emits waves as shown in section 5.5. The modulation of waves excited by an initial wave-scale potential temperature perturbation inside clouds is investigated in section 5.7. Section 5.8 gives a brief introduction into a code featuring a full bulk micro-physics model and presents simulations to validate some results of the analysis of the reduced model.

5.1. Witch of Agnesi Topography

In order to further validate the employed scheme, the ability of the time-dependent code to produce essential patterns of the steady-state solutions discussed in 3.4 is demonstrated. The domain is $[0, 8] \times [0, 1.5]$, whereas the region from $z = 1$ to $z = 1.5$ constitutes the damping layer. The background flow is increased linearly from $\tau = 0$ to $\tau = 0.25$ to a maximum of $u^\infty = 0.1$. The stratification is $\sqrt{\Theta_z^{(2)}} = 1$ and the topography a Witch of Agnesi hill, see (3.95), with $h = 0.04$ and $l = 0.1$. The employed spatial resolutions are $\Delta x = 0.04$ and $\Delta z = 0.02$.

Figure 5.1 shows isolines of the dimensional vertical velocity at $\tau = 50$. Comparison to the analytical steady-state solution for $\sigma \equiv 0.5$ in figure 3.12 reveals

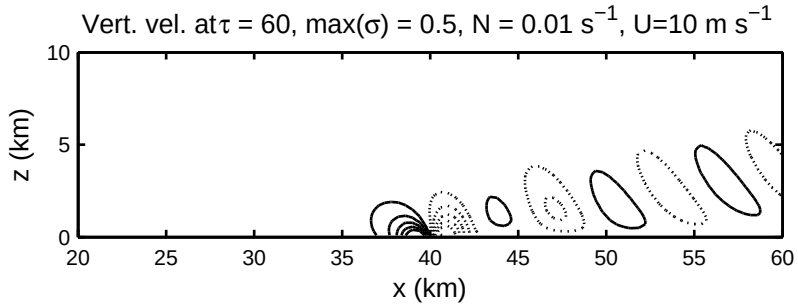

Figure 5.1.: *Isolines of dimensional $\bar{w}$ for a Witch of Agnesi topography and constant $\sigma \equiv 0.5$. The interval between isolines is 0.25 $m\ s^{-1}$, dotted lines show negative values.*

that the weak extrema at the top of the domain are not reproduced by the time-dependent code, presumably because of numerical dissipation. The main wave pattern excited from the hill, however, matches very well.

5.2. Cut-off in a Non-Stationary Solution

To demonstrate the existence of a lower cut-off wave-number in non-stationary solutions, adopt the setup from subsection 3.3.5 and solve the corresponding time-dependent problem numerically. The employed domain is $[0, 2\pi] \times [0, 1.5]$, whereas the damping layer is located between $z = 1$ and $z = 1.5$. A sinusoidal topography with $k = 2$ and height $h = 0.04$ is used, the background flow is increased linearly from zero at $\tau = 0$ to $u^\infty = 0.1$ at $\tau = 0.25$ and remains constant thereafter. The horizontal resolution is $\Delta x = 2\pi/200$, the vertical $\Delta z = 0.02$. Two solutions are computed, one with $\sigma = 0.05$ everywhere and a reference solution with $\sigma \equiv 0$.

Figure 5.2 shows the resulting vertical velocities at $\tau = 50$. Comparing 5.2_1 and 5.2_2 clearly demonstrates the cut-off.

5.3. Orographic Waves Disturbed by an Advected Cloud Envelope

This section presents an investigation of how a cloud-packet advected through the domain disturbs a wave pattern excited from a Witch of Agnesi hill. The cloud packet is described by a Gaussian distributed σ, the employed domain is $[-3, 3] \times [0, 1.5]$, whereas the region from $z = 1$ to $z = 1.5$ constitutes the damping layer. In the following, solutions are shown on a $[-2, 2] \times [0, 1]$ subset. The

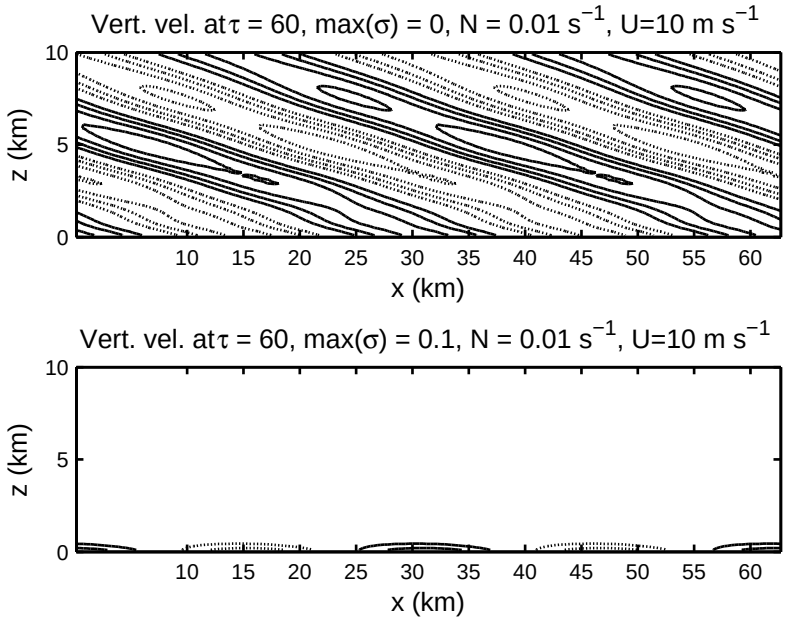

Figure 5.2.: *Isolines of $\bar{w}$, the difference between two lines is* 0.25 *m* s^{-1}. *Shown are the dry reference solution with* $\sigma \equiv 0$ (upper) *and the solution with* $\sigma = 0.05$ (lower).

topography is (3.95) with $h = 0.04$ and $l = 0.1$. Spatial and vertical resolution equal $\Delta x = \Delta z = 0.02$ or 200 m in dimensional units. The background flow is increased linearly from zero at $\tau = 0$ to a maximum of $u^\infty = 0.1$ at $\tau = 0.25$. In order to avoid a sudden introduction of clouds into the simulation, σ is set to zero until $\tau_\sigma = 3$. For $\tau \geq \tau_\sigma$, σ is set to

$$\sigma(x, z, \tau) = \sigma_{\max} \exp\left(-\frac{1}{2}\left[\frac{(x - x_c - u^\infty[\tau - \tau_\sigma])^2}{s_x^2} + \frac{(z - z_c)^2}{s_z^2}\right]\right) \tag{5.1}$$

with $s_x = 0.1$, $s_z = 0.25$ and $z_c = 0.4$. Further set

$$x_c = x_{\text{shift}} - 2 \cdot s_x \quad \text{with} \quad x_{\text{shift}} = -4 \tag{5.2}$$

so at τ_σ the maximum of σ is outside the actual domain of computation at $x = -4$ and subsequently advected into and through the domain. For comparison, a dry reference solution with $\sigma \equiv 0$ is computed, too.

Figure 5.3 shows contours of $\bar{w}$ for the dry reference simulation at $\tau = 42.5$. The mountain in the center of the domain excites waves. At $\tau = 42.5$ an almost steady pattern has formed, resembling the steady-state solution shown in the upper figure in 3.12.

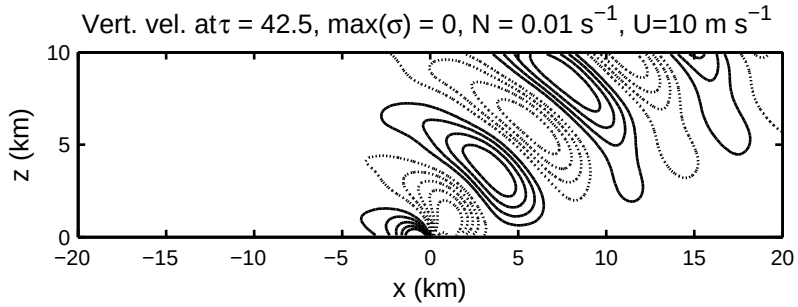

Figure 5.3.: *Contour lines of the dimensional vertical velocity* $\bar{w}$ *at* $\tau = 42.5$ *for the dry reference simulation. The interval between contour lines is* 0.25 *m* s^{-1}. *Dotted contours represent negative values.*

Figure 5.4 visualizes the actual solution with the advected cloud-packet at times $\tau = 27.5$, $\tau = 35$, $\tau = 42.5$ and $\tau = 50$ (top to bottom). Shown are isolines of dimensionalized $\bar{w}$ in steps of 0.25 m s^{-1}. The position of the cloud-packet is indicated by thin $\sigma = 0.05$ and $\sigma = 0.25$ contour lines.

At $\tau = 27.5$, the cloud packet has entered the depicted domain from the left. It has not yet noticeably affected the wave pattern, but a weak updraft has formed inside it. The packet starts passing through the wave pattern at about $\tau = 35$ and slightly damps the downdraft right above the hill. Comparing the solution at $\tau = 42.5$ with the reference solution in figure 5.3 reveals strong damping of $\bar{w}$ in the upper regions behind the packet. A strong downdraft exists in the lower part of the cloud-packet. Updrafts in front of the packet are amplified and a new maximum of $\bar{w}$ has formed in the lower region. In the last figure, showing the solution at $\tau = 50$, the downdraft inside the packet has almost vanished while the wave pattern over the hill starts to regenerate, but its angle of propagation appears to be slightly reduced.

In order to point out damping and amplification of up- and downdrafts by the cloud-packet more concisely, figure 5.5 visualizes the difference between the absolute values of $\bar{w}$ in the moist and dry simulation, i.e. $|\bar{w}_{\text{moist}}| - |\bar{w}_{\text{dry}}|$. The interval between contour lines is 0.2 m s^{-1}. Solid lines correspond to positive values, i.e. areas where moisture amplified either an up- or a downdraft while dotted lines correspond to negative values, i.e. regions where wave amplitudes in the moist simulation are smaller than in the dry reference solution.

At $\tau = 35$, strong amplification at the center of the packet is accompanied by significant damping in its upper and lower regions. The second figure, comparing the solutions at $\tau = 42.5$, demonstrates damping behind and in the center of the cloud-packet, accompanied by amplification in front of the cloud and inside its lower part. Finally at $\tau = 50$, the wave pattern appears to have been bent towards the horizontal by the passing cloud-packet, as amplitudes in higher regions

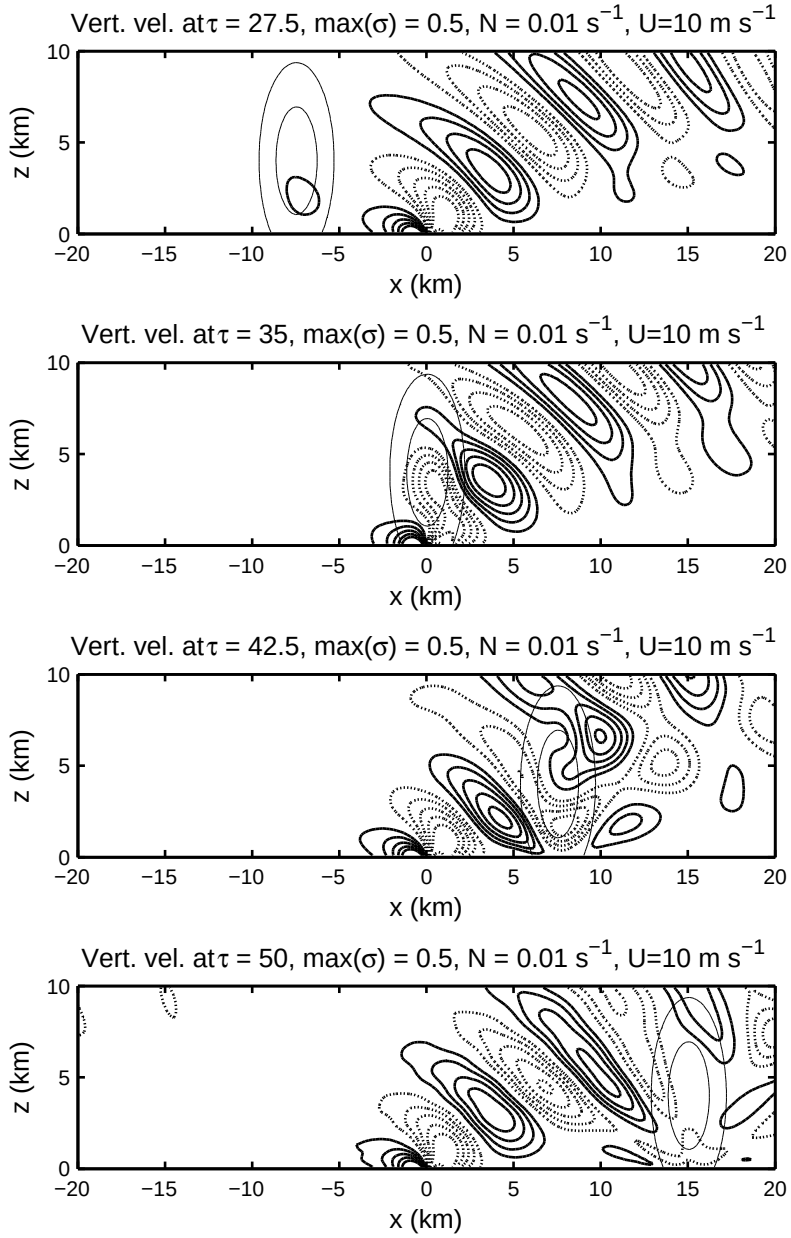

Figure 5.4.: *Contour lines of dimensionalized $\bar{w}$ at different times for the moving cloud packet with $\sigma_{\max} = 0.5$. The interval between contours is $0.25\ m\ s^{-1}$. Dotted contours represent negative values. The two thin circles indicate the $\sigma = 0.05$ and $\sigma = 0.25$ isoline.*

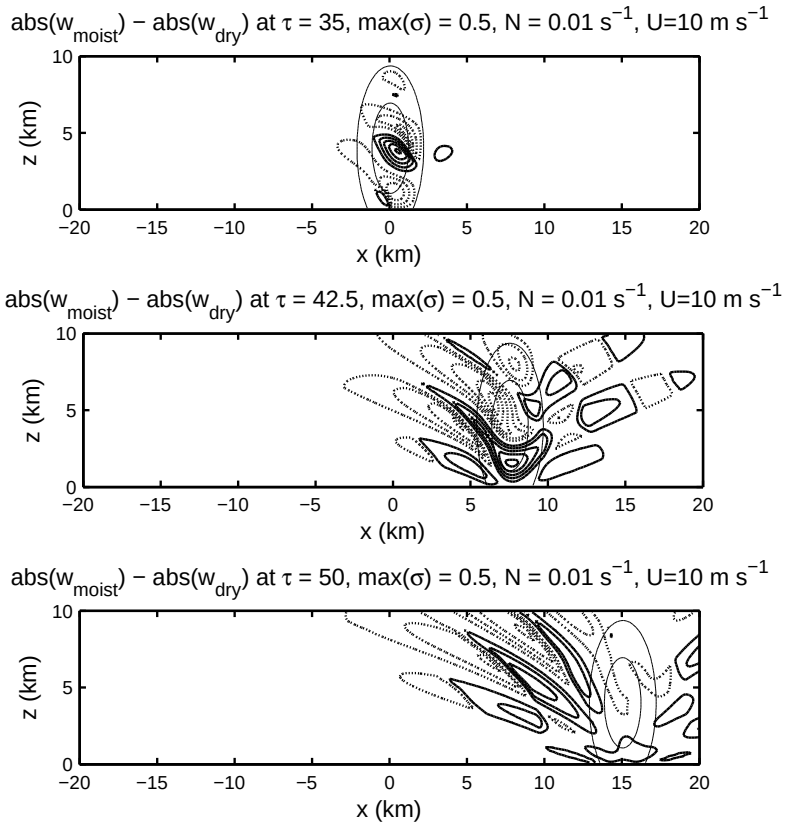

Figure 5.5.: *Contour lines of the difference of* $|\bar{w}_{\text{moist}}|-|\bar{w}_{\text{dry}}|$*, where* $\bar{w}_{\text{moist}}$ *is the vertical velocity from the* $\sigma_{\max} = 0.5$ *cloud-packet simulation and* $\bar{w}_{\text{dry}}$ *from the dry reference simulation. The interval between isolines is* $0.2\ m\ s^{-1}$*, dotted lines indicate negative values. The two thin circles show the* $\sigma = 0.05$ *and* $\sigma = 0.25$ *isoline from the cloudy simulation.*

above the hill are damped, while amplitudes further in the mountains lee side are amplified, consistent with the reduced height of the extrema behind the cloud-packet in 5.4_4.

Figure 5.6 shows the net vertical flux of horizontal momentum (2.34) along the height $z = 1$ over time. Values derived from an additional simulation are added, whereas the only modification is setting $\sigma_{\max} = 0.2$. The passing cloud-envelope leads to a strong decrease of momentum flux, with a larger reduction obtained for $\sigma_{\max} = 0.5$ than for $\sigma_{\max} = 0.2$. This is in line with the findings for stationary solutions in 3.4.2, also indicating that moisture inhibits flux of momentum.

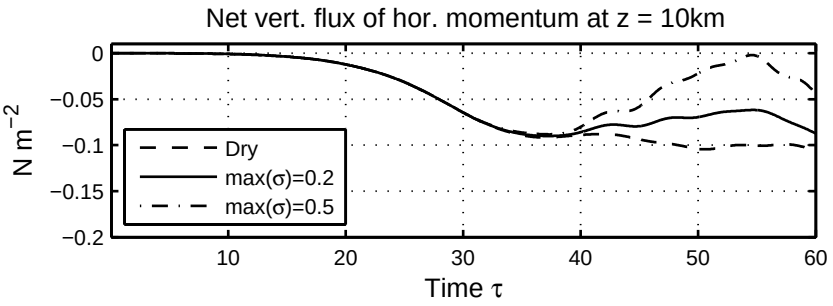

Figure 5.6.: *Net momentum flux over time at $z = 10$ km for the advected cloud-envelope simulation.*

5.4. Critical Layers

Section 3.5 demonstrates how σ can cause critical layers in steady-state flows. Two types of critical layers are distinguished. If σ increases with height up to its critical value, the solution propagates below the layer and turns into evanescent. In the approximate solutions derived in section 3.5, this causes a complete inhibition of wave-propagation and momentum flux. Non-stationary solutions for this type of critical layer are presented in subsection 5.4.1. In contrast, if σ is decreasing down to its critical value with height, solutions in section 3.5 are evanescent below the layer but propagate above it. It is found that, in principle, the contribution at the critical height from the decaying mode can excite noticeable oscillations above the layer. An increase of the critical height results in strongly reduced amplitudes in the excited oscillation. Subsection 5.4.2 presents non-stationary solutions obtained for this type of critical layer.

The domain for the simulation is $[0, 2\pi] \times [0, 1.5]$ and, as before, the region from $z = 1$ to $z = 1.5$ constitutes the damping layer. The topography is set to

$$h(x) = \sin(2x) \tag{5.3}$$

so only a single mode with $k = 2$ is excited, in agreement with the structure of the solutions shown in section 3.5. The background flow is $u^\infty = 0.1$, again linearly increasing from $\tau = 0$ to $\tau = 0.25$ and the stratification is set to $\sqrt{\Theta_z^{(2)}} = 1$. These parameters are identical to those in section 5.2, so the dry solution presented there can serve as reference solution for this section, too.

According to (3.99), the critical value for σ in stationary solutions equals

$$\sigma_{\text{crit}} = \frac{0.1^2 2^2}{1} = 0.04. \tag{5.4}$$

Three different profiles for σ are introduced here. One features an increasing σ and critical height $z_c = 0.75$, and two feature decreasing σ with either $z_c = 0.25$

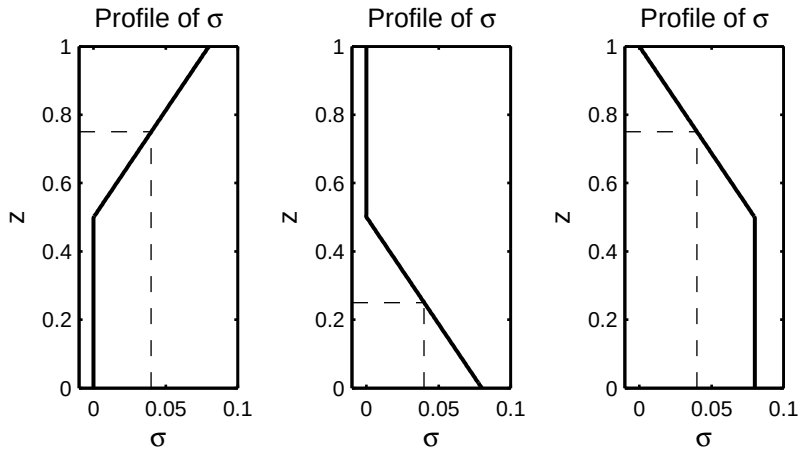

Figure 5.7.: *Three different profiles of σ leading to a critical layer: Increasing σ with $z_c = 0.75$* (left)*, decreasing σ with $z_c = 0.25$* (center) *and $z_c = 0.75$* (right)*. The dashed line marks the critical height and the critical value σ_{crit}.*

or $z_c = 0.75$. All three profiles are sketched in figure 5.7. Note that in the figures below, the solution as well as the axis are converted into dimensional units and $z_c = 0.25$ and $z_c = 0.75$ correspond to heights of $z_c^* = 2.5$ km and $z_c^* = 7.5$ km.

5.4.1. Increasing σ

Figure 5.8 shows the solution for the increasing σ profile at $\tau = 60$. The horizontal line indicates $\sigma_{crit} = 0.04$. As expected, the solution propagates below the layer, but is quickly decaying above it. Some wave activity can be noticed beyond the critical height $z_c^* = 7.5$ km, compatible with the analysis in section 3.5 revealing exponential decay of the solution in a thin layer above z_c. Further, (5.4) obtains for the steady-state solution, hence in the presented non-stationary solution some transient contributions above the critical layer are also possible.

5.4.2. Decreasing σ

Figure 5.9 shows the solution at $\tau = 60$ for decreasing σ with $z_c^* = 2.5$ km (upper) and $z_c^* = 7.5$ km (lower). Because the amplitude of the excited wave in the upper figure is small, the scaling is changed to an interval between the isolines of 0.05 m s^{-1}, in order to ensure the propagating part of the solution is recognizable. Both simulations confirm the qualitative behavior predicted in section 3.5. The evanescent mode below the critical layer excites a propagating wave above it. According to the densely packed isolines near the ground, the

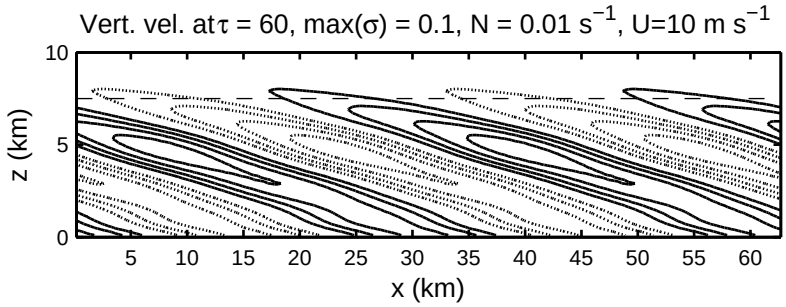

Figure 5.8.: *Wave excited by a sinusoidal topography in presence of a critical layer at* $z_c^* = 7.5$ *km.* σ *increases linearly, cf. figure 5.7. The difference between isolines is* 0.25 $m\ s^{-1}$*, dotted contours indicate negative values.*

amplitude of the propagating wave is noticeable smaller than the amplitude excited by the topography at the bottom.

The lower figure exhibits four extrema located in the lower region, that are incompatible with an exponentially decaying evanescent mode. Reckoning a full series of figures of the evolution of the transient simulation suggests this to be a transient effect of the time-dependent solution.

5.4.3. Momentum Flux

Figure 5.10 shows vertical profiles of momentum flux (2.34) at $\tau = 60$, expressed as a fraction of the value obtained from the dry reference simulation. For increasing σ (left figure), the momentum flux is approximately equal to the dry reference value up to a height of $z^* = 5$ km. It then decreases down to zero over a broad region around the critical height $z_c^* = 7.5$ km. Hence as in the qualitative analytical solution derived in section 3.5, the presence of the critical layer shuts down the flux of momentum but in the transient, discrete simulation the momentum flux does not sharply drop to zero but decays over a larger region.

The results in section 3.5 suggest that for the case of decreasing σ the evanescent mode below the layer can excite a noticeable propagating response above it and thus induce a significant flux of momentum. However, the solutions there only employ arbitrary coefficients and the middle and right figure in 5.10 suggest that this is not the case for realistic amplitudes. The overall momentum flux is strongly inhibited in both cases. A small and supposedly transient contribution is visible at about $z^* = 1$ km. Also a very weak non-zero momentum flux is noticeable above the critical layer, but only on the order of a few percent of the flux obtained in the dry case.

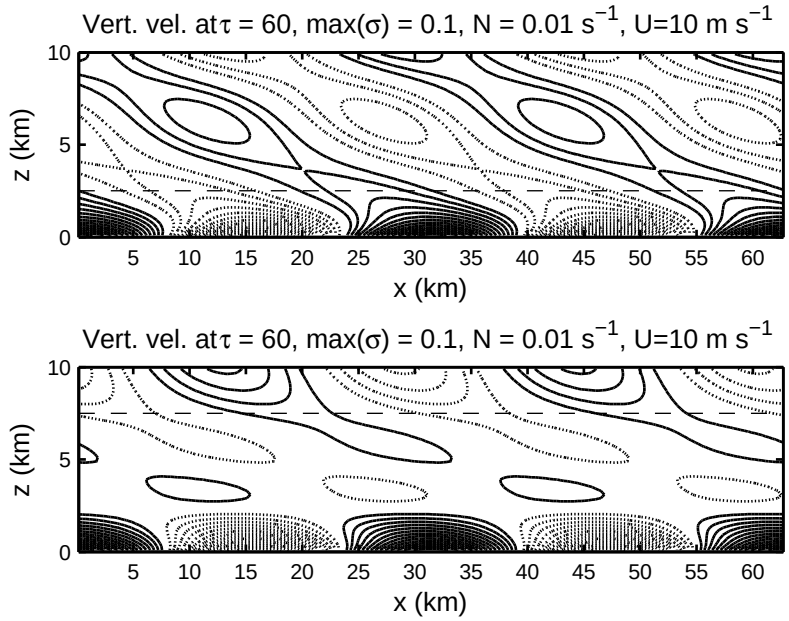

Figure 5.9.: *Wave excited by a sinusoidal topography in presence of a critical layer at* $z_c^* = 2.5$ *km* (upper) *and* $z_c^* = 7.5$ *km* (lower) *with decreasing* σ*, cf. figure 5.7. The difference between isolines is* $0.05\ m\ s^{-1}$*, dotted contours indicate negative values.*

5.5. Evaporating Rain

Evaporation of rain water in non-saturated regions results in the constant source term $\bar{C}_-$ in (2.70). To demonstrate how such cooling generates waves, employ a domain $[-5, 5] \times [0, 1.25]$, no background flow, i.e. $u^\infty = 0$ and a background stratification of $\sqrt{\Theta_z^{(2)}} = 1$. The resolution is set to $\Delta x = \Delta z = 0.025$, the timestep to $\Delta\tau = 0.05$ and the simulation is run until $\tau = 60$. A cloud-packet is placed into the middle of the domain, represented by

$$\sigma = 0.2 \exp\left(-\frac{1}{2}\left(\left(\frac{x}{0.2}\right)^2 + \left(\frac{z-0.5}{0.05}\right)^2\right)\right). \tag{5.5}$$

A concentrated spot of "rain" described as

$$\bar{C}_- = -\exp\left(-\frac{1}{2}\left(\left(\frac{x}{0.1}\right)^2 + \left(\frac{z-0.35}{0.025}\right)^2\right)\right) \tag{5.6}$$

is placed below the cloud. Figure 5.11 sketches this setup. Figure 5.12 shows the generated dimensionalized vertical velocity $\bar{w}$ at $\tau = 60$. The interval between

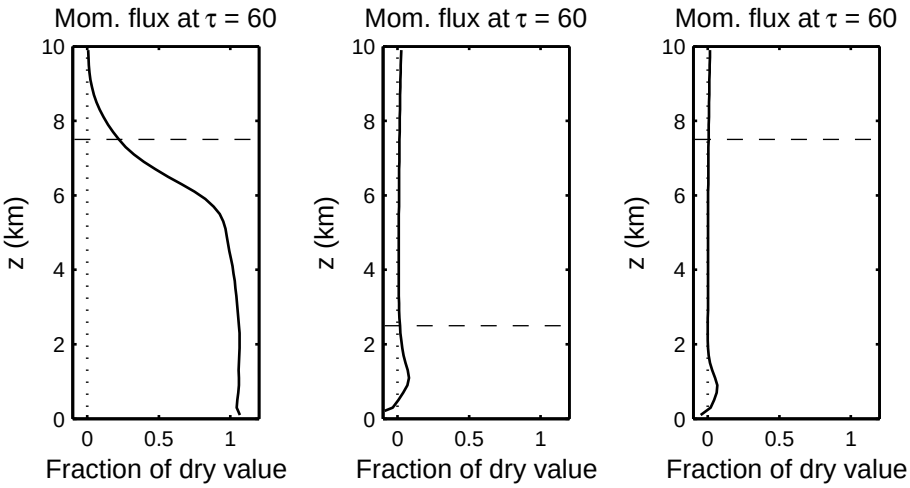

Figure 5.10.: *Vertical profile of momentum flux at $\tau = 60$ as a fraction of the value from the dry reference simulation. The dashed line indicates the critical height.* Left: *Increasing σ with $z_c^* = 7.5$ km.* Center: *Decreasing σ with $z_c^* = 2.5$ km.* Right: *Decreasing σ with $z_c^* = 7.5$ km.*

isolines is 0.2 m s^{-1}. Numerous small waves have emerged, propagating away from the rain spot. The depletion by evaporation as well as the downfall of rain is not included in the model, hence the source term $\bar{C}_-$ is constant in time and excites not a single set of waves, but launches waves continuously. For the times used in the simulation this is not realistic, but it suffices to demonstrate how waves are excited by cooling through evaporating rain in the model.

5.6. Waves Excited by Tower-Scale Dynamics

As pointed out in subsection 3.1.5, tower-scale processes in (2.70) excite waves on the large-scale. To demonstrate this, place a concentrated perturbation of tower-scale potential temperature θ' inside a cloud-packet. Set

$$\theta'(x, z, \tau = 0) = \exp\left(-\frac{1}{2}\left(\left(\frac{x}{0.1}\right)^2 + \left(\frac{z - 0.5}{0.05}\right)^2\right)\right) \tag{5.7}$$

and w' as well as the large-scale quantities to zero. Place a "cloud" around the θ'-perturbation

$$\sigma(x, z) = 0.2 \exp\left(-\frac{1}{2}\left(\left(\frac{x}{0.25}\right)^2 + \left(\frac{z - 0.5}{0.25}\right)^2\right)\right) \tag{5.8}$$

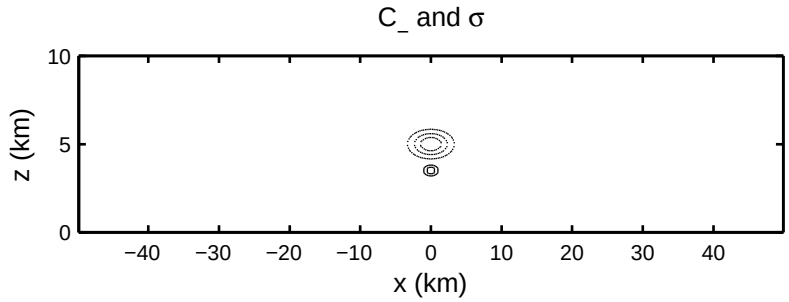

Figure 5.11.: *"Cloud" described by σ, visualized by the $\sigma = 0.05, 0.1, 0.15$ isolines (upper structure) and the negative, evaporating rain source term $\bar{C}_-$, visualized by isolines $\bar{C}_- = -0.3, -0.6, -0.9$ (lower structure) below it.*

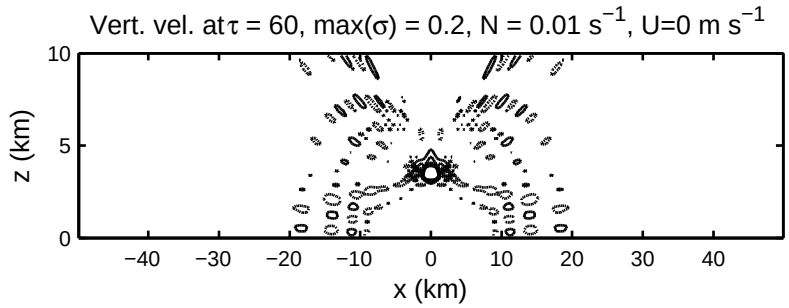

Figure 5.12.: *Waves excited by evaporating rain. Shown are isolines of $\bar{w}$, the difference between two lines is 0.2 m s^{-1}. Dotted lines correspond to negative values.*

and set $\sqrt{\Theta_z^{(2)}} = 1$, $u^\infty = 0.05$ or 0.01 s^{-1}, 5 m s^{-1} respectively. The domain is $[-5, 5] \times [0, 1.25]$ with the damping layer located between $z = 1$ and $z = 1.25$. The resolution is $\Delta x = \Delta z = 0.025$, the timestep $\Delta\tau = 0.05$ and the simulation is run until $\tau = 60$.

Figure 5.13 shows the large-scale vertical velocity $\bar{w}$ at $\tau = 60$. It reveals a pronounced pattern of waves travelling away from the cloud-packet in up- and downstream direction. The wave pattern as well as the cloud have been advected downstream by u^∞. The phase lines are slanted from the vertical, indicating vertical propagation. From a qualitative point of view, the pattern resembles the stratospheric waves generated by a mechanical oscillator model in [FDH91].

Figure 5.14 demonstrates that the generated waves induce a net momentum flux across the top of the domain. Although the momentum flux is about two orders of magnitude smaller than in the orographic wave example presented in section 5.3, this demonstrates that in principle the model also includes a mechanism for the generation of momentum flux by tower-scale dynamics. Besides momentum

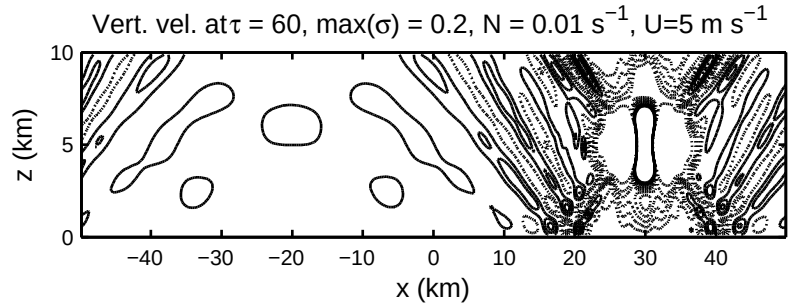

Figure 5.13.: *Waves excited by tower-scale dynamics. Shown are isolines of $\bar{w}$, the interval between two lines is 0.25 $m\ s^{-1}$. Dotted lines represent negative values.*

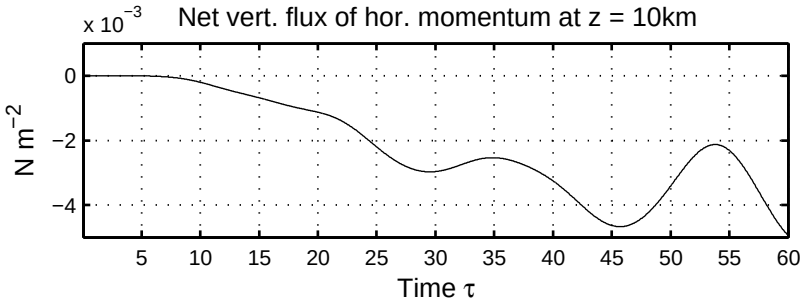

Figure 5.14.: *Net momentum flux at $z = 10$ km over time, caused by waves excited by tower-scale dynamics.*

flux caused by orographically generated waves, convectively generated momentum flux is also an important source of overall gravity wave drag, see e.g. [KEC03] and numerous citations therein.

5.7. Modulation of Waves Inside Cloud-Packets

To analyze the modulation of waves entering cloudy regions, a localized distribution of negative large-scale potential temperature $\bar{\theta}$ is placed between two cloud-packets. The initial buoyancy induces downdrafts and excites wave, which subsequently propagate through the cloud-packets. Employ a domain $[-5, 5] \times [0, 1.25]$, again with a damping layer between $z = 1$ and $z = 1.25$. Set $\sqrt{\Theta_z^{(2)}} = 1$ and $u^\infty = 0$. The spatial resolution is $\Delta x = \Delta z = 0.025$ and the timestep $\Delta\tau = 0.1$. The initial $\bar{\theta}$ is a concentrated Gaussian peak, the two cloud packets are located between $x = -30$ and $x = -1$ as well as $x = 1$ and $x = 3$, figure 5.15 sketches the initial setup.

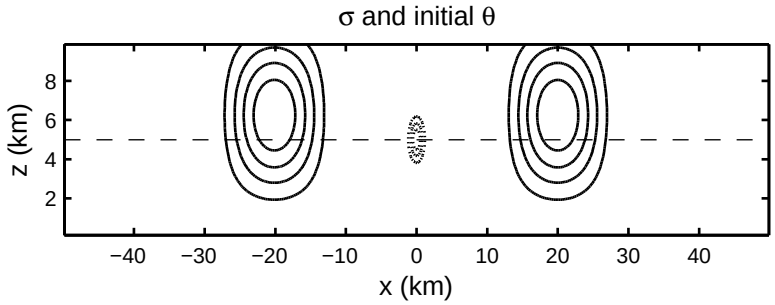

Figure 5.15.: *Initial distribution of $\bar{\theta}$ (dotted) in steps of -0.025. The solid lines indicate σ, the interval between isolines being 0.1. The dashed line marks the cross section along which figure 5.16 shows the vertical velocity.*

Figure 5.16 shows three horizontal cross sections through $\bar{w}$ at $z^* = 5$ km, cf. the dashed lines in figure 5.15, at $\tau = 7$, $\tau = 9$ and $\tau = 14$. The cross section through σ is indicated by the dotted lines, but values are scaled, so that the line is recognizable. For comparison, a reference solution with $\sigma \equiv 0$ is computed, the resulting $\bar{w}$ is depicted by the dashed line in figure 5.15.

At $x = 0$, the initial $\bar{\theta}$ causes oscillations of $\bar{w}$. Waves radiate outwards in both directions and have propagated into the cloud-packet at $\tau = 7$. The updrafts inside the clouds are amplified. The propagation speed of the waves is reduced inside the clouds, causing a steepening of gradients in front of them and leading to an amplification of the downdrafts located at ± 10 km. Note how at $\tau = 9$ the distance between the extrema in the cloudy case is reduced inside the cloud-packet compared to the reference simulation. The solution at $\tau = 14$ reveals noticeable damping of the wave amplitudes behind the cloud-packets, confirming the inhibition of wave-packet propagation by moisture, as well as the generation of steeper gradients in front of them, pointing to the reduced propagation speed.

5.8. Comparison with ASAM Simulations

The "All-Scale Atmospheric Model" ASAM developed at IfT[1] solves the moist compressible Euler equations combined with a full bulk micro-physics model using high order, linear implicit Rosenbrock-Wanner timestepping. The model includes a concise treatment of cut-cells arising for example from topography at the bottom. Details on the implementation of the code as well as the documentation of several test cases can be found in [HK05, IfTiL].

[1] Leibniz-Institut für Troposphärenforschung, Leipzig

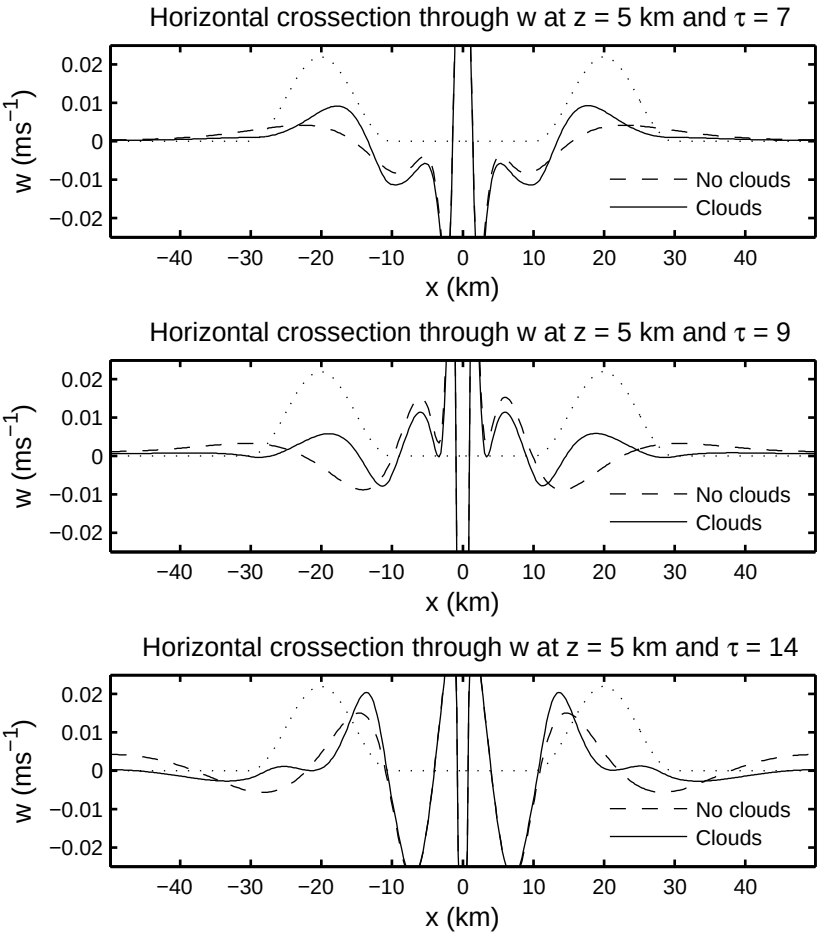

Figure 5.16.: *Cross section through $\bar{w}$ at $z^* = 5$ km at different times. The dotted line sketches σ.*

5.8.1. Initial Thermodynamic Profiles

The model is non-hydrostatic, but requires hydrostatically balanced initial profiles. These are generated by column-wise vertical integration of a system of differential-algebraic equations

$$\begin{aligned} p_z &= -\left(\rho_\mathrm{d} + \rho_\mathrm{vl}\right) g \\ p &= \left(\rho_\mathrm{d} R_\mathrm{d} + \rho_\mathrm{v} R_\mathrm{v}\right) T \\ \theta &= \theta_0 \exp(10^{-5} z) \\ \theta &= T \left(\frac{p_0}{p}\right)^{\Xi} \\ \rho_\mathrm{v} &= \min\left(\rho_\mathrm{vl}, \frac{p_\mathrm{vs}}{R_\mathrm{v} T}\right) \\ \rho_\mathrm{vl} &= f(x,z) \frac{p_\mathrm{vs}}{R_\mathrm{v} T} \end{aligned} \tag{5.9}$$

with

$$\Xi = \frac{R_\mathrm{d}\rho_\mathrm{d} + R_\mathrm{v}\rho_\mathrm{vl}}{C_\mathrm{pd}\rho_\mathrm{d} + C_\mathrm{pv}\rho_\mathrm{v} + C_\mathrm{pl}\left(\rho_\mathrm{vl} - \rho_\mathrm{v}\right)}. \tag{5.10}$$

Equation $(5.9)_1$ is the hydrostatic balance with pressure p, dry density ρ_d, density of vapor and liquid water ρ_vl and gravity $g = 9.81$. Equation $(5.9)_2$ is the ideal gas law for the air-vapor mixture, R_d and R_v are the gas constants for dry air and vapor. ρ_v is the density of vapor while T denotes sensible temperature. Equation $(5.9)_3$ prescribes a profile for the potential temperature θ, starting from a given value θ_0 at $z = 0$. Note that $(5.9)_3$ yields a stability frequency of approximately

$$N = \sqrt{\frac{g}{\theta}\frac{\partial\theta}{\partial z}} \approx 10^{-2}. \tag{5.11}$$

Equation $(5.9)_4$ is the definition of potential temperature. Ξ is the isentropic exponent R/c_p, but the gas constant R as well as the specific heat c_p vary depending on the amount of vapor and liquid water, so Ξ is not constant but computed from (5.10). Equation $(5.9)_5$ defines the vapor density ρ_v. In the used bulk microphysics model, no over-saturation and no liquid water in non-saturated regions occur, i.e. condensation and evaporation are instantaneous, so either $\rho_\mathrm{v} = \rho_\mathrm{vl}$ in non-saturated regions or $\rho_\mathrm{v} = \rho_\mathrm{vs}$, where ρ_vs is the saturation density. According to the ideal gas law, $\rho_\mathrm{vs} = p_\mathrm{vs}/(R_\mathrm{v}T)$ obtains where $p_\mathrm{vs} = p_\mathrm{vs}(T)$ is the saturation pressure. Finally, $(5.9)_6$ prescribes the initial density of total water, i.e. vapor and liquid. It is defined by the function $f(x,z)$ as a fraction of saturation density, given by $p_\mathrm{vs}/(R_\mathrm{v}T)$. Thus setting $f(x,z) > 1$ results in $\rho_\mathrm{vl} > \rho_\mathrm{vs}$ corresponding to saturated air. According to $(5.9)_5$ it holds that $\rho_\mathrm{v} = \rho_\mathrm{vs}$ and thus the difference $\rho_\mathrm{vl} - \rho_v$ indicates liquid water. For $f(x,z) < 1$ the air is under-saturated, so

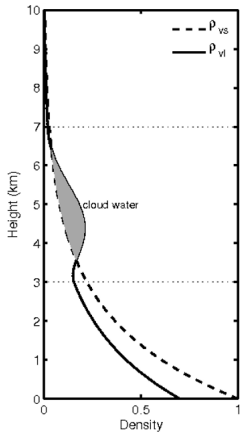

Figure 5.17.: *General shape of profiles for* ρ_{vl} *and* ρ_{vs} *with* $f = 0.7$ *below* 3 *km and above* 7 *km, corresponding to a relative humidity of* 70 %. *In between, a* $\cos^2$*-shaped perturbation with maximum amplitude* 1.5 *is added, resulting in the sketched profile of* ρ_{vl}. *Cloud water exists where* $\rho_{\mathrm{vl}} > \rho_{\mathrm{vs}}$ *obtains. The amount of cloud water is indicated by the gray area.*

$\rho_{\mathrm{vl}} = \rho_{\mathrm{v}}$ obtains and $100 \cdot f(x, z)$ denotes the relative humidity in percent. Figure 5.17 sketches the general structure of ρ_{vl} and ρ_{vs}.

5.8.2. Sub-Column Representation of σ

As ASAM is not explicitly separating scales, an implementable representation of σ in terms of single-scale distributions of cloud water has to be derived. This is achieved by considering a coarse mesh, consisting of relatively wide cells suitable to resolve large-scale dynamics. Each cell is then partitioned into a number of sub-columns as sketched in figure 5.18, generating a refined mesh, consisting of rectangular cells with increased horizontal resolution. By defining distributions of cloud water on this fine mesh, distributions of σ on the coarser mesh can be emulated. The vertical resolution of the mesh is not enhanced, as the asymptotic model contains no vertical micro-scale.

Figure 5.19 sketches how a value of $\sigma = 0.6$ on a coarse-mesh cell can be represented using ten sub-columns. Note that using N sub-columns per cell allows to represent σ with a resolution of $1/N$, i.e. for $N = 10$ sub-columns, σ can vary between zero and unity in steps of $\Delta\sigma = 0.1$. Because all distributions are constant in z over the extend of a single cell, a simple horizontal cut is shown in figure 5.19.

The continuous distribution of ρ_{v} is approximated by a cell-centered, piecewise constant function. The saturation density ρ_{vs} does depend only on height and is

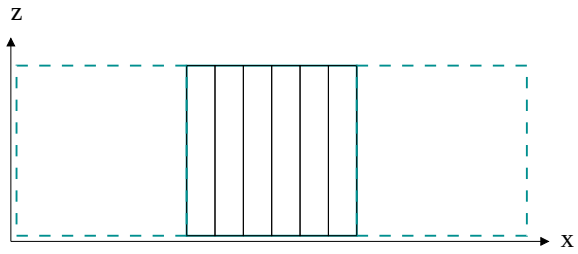

Figure 5.18.: *The large, dashed boxes are coarse grid cells. All cells are divided into a number of sub-columns, as sketched for the middle cell. Those rectangular, small cells form the "fine" mesh, suitable of resolving small-scale horizontal distributions of moisture.*

thus a constant line. Every sub-column, corresponding to a rectangular fine-mesh cell, where the approximation of ρ_v is larger than ρ_vs is considered saturated. There are six of such cells out of ten, so the saturated area fraction for the coarse-grid cell is $\sigma = 6/10 = 0.6$. Note that this distinction of coarse cells and sub-columns is a thought construct to establish a connection between σ and the initial value for ρ_v and the code does not feature this distinction explicitly.

Naturally, there are many other possible distributions of how a value of $\sigma = 0.6$ could be represented and a detailed investigation has to check, whether the obtained results are robust to variations at this point. Further, the hypothesis that, at least on short timescales, the most influential quantity is the saturated area fraction and not the actual amount of cloud water, has to be scrutinized. This section, however, focusses only on a qualitative confirmation of two effects of moisture found in the analysis of the asymptotic model: (i) modulation of wave amplitudes and (ii) reduction of momentum flux, postponing a more detailed analysis.

5.8.3. Orographic Waves Disturbed by Travelling Cloud-Packet

This section presents a simulation trying to confirm the results in section 5.3 for the cloud-packet disturbing an established pattern of orographic waves. The domain is $[-25\ \mathrm{km}, 20\ \mathrm{km}] \times [0, 15\ \mathrm{km}]$, whereas a damping layer is located between $z = 10$ km and $z = 15$ km. The topography is the dimensional counterpart of the Witch of Agnesi (3.95) with $h = 400$ m and $l = 1000$ m. The initial horizontal velocity is $u = 10\ \mathrm{m\ s^{-1}}$. The mesh consists of 1500 cells in the horizontal and 75 in the vertical, whereas each 5 horizontally consecutive cells are considered to be sub-columns with respect to the representation of σ.

To emulate the wave-packet employed in (5.3), set

$$f(x,z) = 0.9 + 0.1 \exp\left(-\frac{1}{2}\left(\frac{(x-x_0)^2}{\sigma_x^2} + \frac{(z-z_0)^2}{\sigma_z^2}\right)\right) - 0.05 \cos\left(\frac{2\pi x}{\Delta x_\mathrm{c}}\right) \quad (5.12)$$

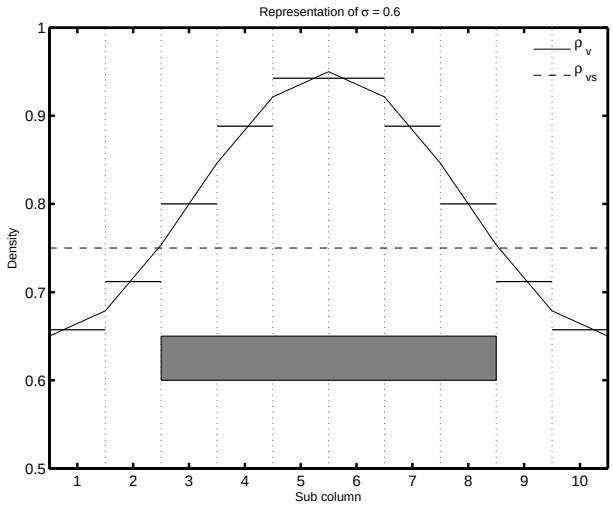

Figure 5.19.: *Representation of $\sigma = 0.6$ over ten sub-columns. The solid line is the continuous, horizontal distribution of ρ_{v}. The model uses a cell-centered approximation, sketched by horizontal lines in every sub-column. The dashed line is the saturation density ρ_{vs}. Each column, where the constant value is above ρ_{vs} is saturated. There are six saturated sub-columns, marked by the gray bar, representing a saturated area fraction of $\sigma = 0.6$. The vertical axis is scaled in arbitrary units.*

with $\sigma_x = 2000$ m, $\sigma_z = 5000$ m, $\Delta x_{\mathrm{c}} = 150$ m and $x_0 = -22.5$ km. Figure 5.20 shows the resulting initial distribution of cloud water mixing ratio (upper) as well as the corresponding equivalent to σ, obtained by counting the saturated sub-columns, cf. figure 5.19.

The cloud-packet is advected across the domain by a horizontal velocity set to 10 m s^{-1} initially. It approaches the center of the hill at about $t = 2250$ s. A well established wave pattern exists at this time.

The sub-column distributed cloud water however is rapidly diffusing and the small-scale pattern generated by (5.12) is smeared out. It is thus questionable whether the details of the small-scale distribution do affect the result in any way or if similar results are obtained by a simple bulk cloud. A more systematic investigation of the representation of σ in a model without explicit scale separation is not pursuit further here but left for future work. Nevertheless, the presented simulation confirms the results obtained from the reduced model in section 5.3, namely damping of waves behind and above the passing cloud, amplification of up- and downdrafts inside the cloud-pattern and reduction of momentum flux at the top of the domain.

Figure 5.21 shows the vertical velocity field at four different times, employing the

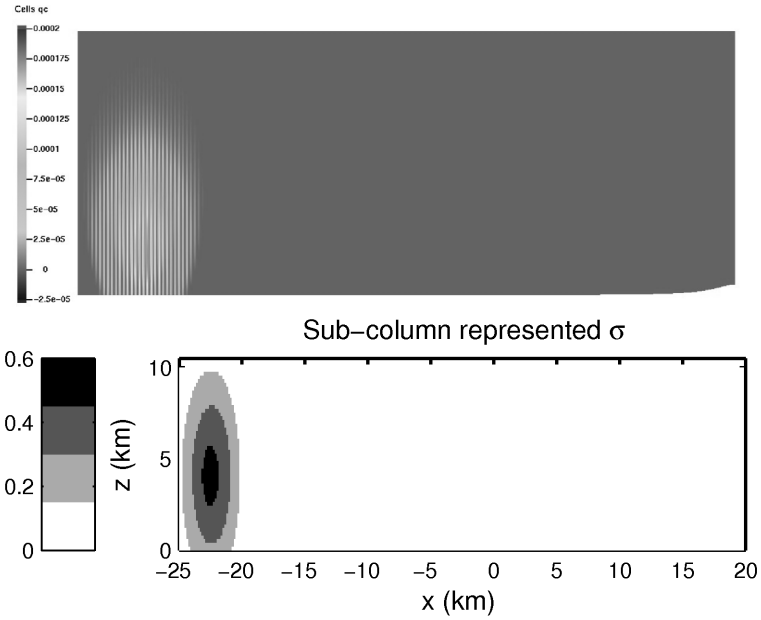

Figure 5.20.: Upper: *Initial q_c in ASAM in kg kg^{-1}.* Lower: *Effective σ resulting from sub-column representation by ρ_{vl} for 5 sub-columns per cell.*

same isolines as figure 5.4, i.e. an interval of 0.25 m s^{-1}. The black dots are inserted manually and give an estimate of the horizontal position of the cloud-pattern. For comparison, figure 5.22 shows the solution of the reference simulation, with no initial clouds and an initial relative humidity of 90 % throughout the domain.

At $t = 1500$ s the cloud-packet is located about 7.5 km before the hill and has not yet noticeably affected the excited waves. The small updraft generated by the cloud in 5.4_1 is not observable in 5.21_1. In the second figure at $t = 2250$ s, the cloud-packet is located directly above the hill just as in 5.4_2. The downdraft right above the hill is noticeably damped in the rear part of the cloud and weakly amplified in the front. Damping behind the cloud is also seen in 5.5_1, but the strong amplification in the center of the cloud is not reproduced in 5.21_2. The solution at $t = 3750$ s is shown in figure 5.21_3. Comparison with $(5.22)_3$ reveals strong damping in the higher regions behind the cloud packet. This is in quite good agreement with 5.5_3. However, 5.21_3 shows a strong updraft inside the cloud, completely absent in 5.4_3. The strong downdraft located in the lower region of the cloud in 5.4_3 is also found in 5.21_3, but rather at medium height in front of the cloud. At $t = 3750$ s the wave pattern over the hill in 5.21_4 has partly reformed, but a noticeably damping is still seen in the higher regions behind the cloud. The updraft inside the cloud-packet has further amplified and reaches vertical velocities of about 8 m s^{-1}. It coincides with large amounts of condensated cloud

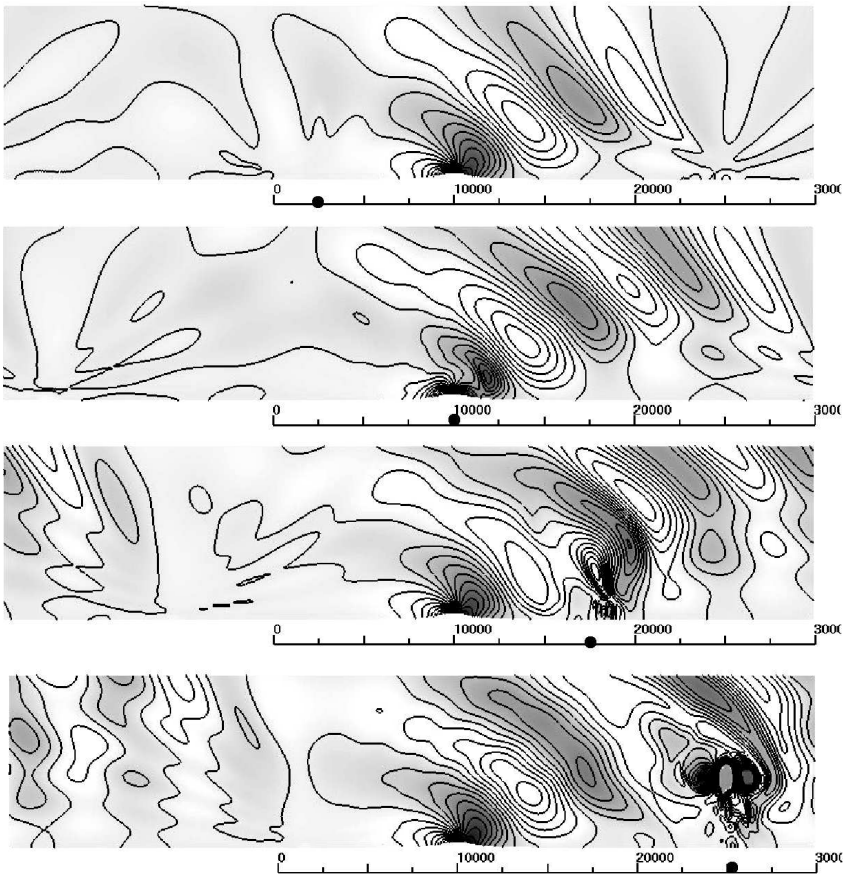

Figure 5.21.: *Vertical velocity in ASAM solution. Isoline interval is* 0.25 $m\ s^{-1}$. *Gray regions indicate negative values. The black circles indicate approximately the horizontal position of the cloud-packet.* From top to bottom: $t = 1500\ s$, $t = 2250\ s$, $t = 3000\ s$, $t = 3750\ s$.

water ($\sim$ 4 g kg^{-1}) and thus is likely due to onsetting moist convection. The reduced model (2.70) does not capture this regime, so its inability to model these effects is to be expected.

Figure 5.23 shows the net vertical flux of horizontal momentum at $z = 10$ km. Also shown is the momentum flux for two reference simulations with $f \equiv 0.9$ and $f \equiv 0$, cf. (5.9), i.e. no clouds and initial relative humidity of 90 % and 0 % respectively. The strongest momentum flux is observed in the completely dry case. It is somewhat reduced in the simulation with 90 % initial relative humidity. The presence of the advected cloud-packet further reduces the overall values of momentum flux. Further, an additional temporary decrease of about 20 % related

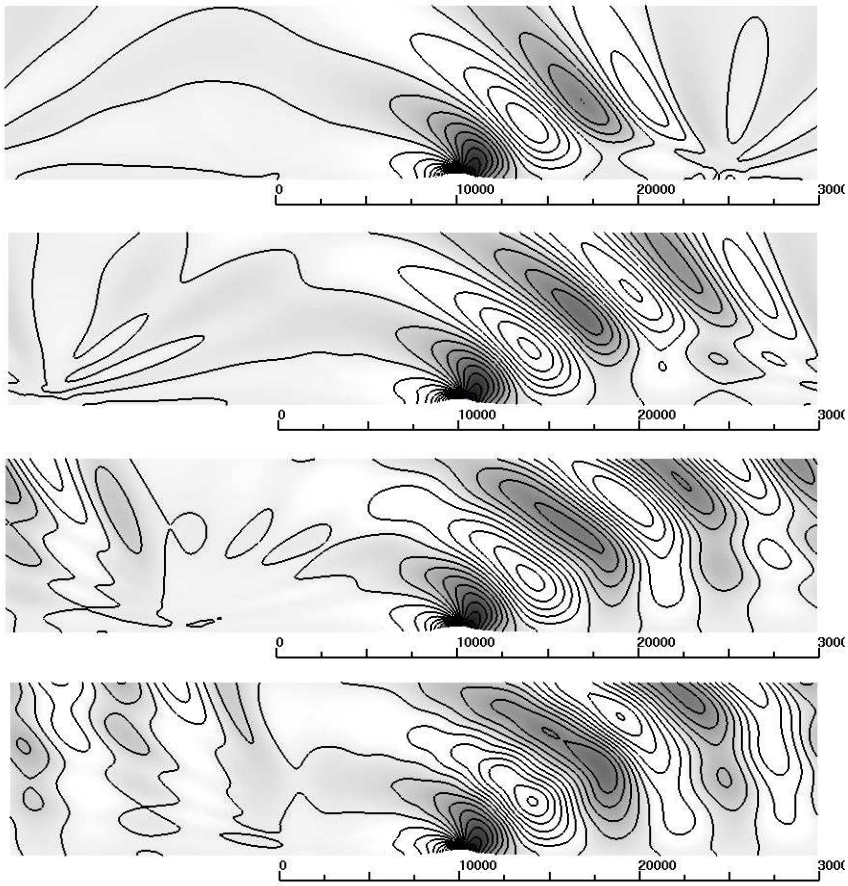

Figure 5.22.: *Vertical velocity in reference simulation with no initial clouds. Isoline interval is* 0.25 $m\ s^{-1}$. *Gray regions indicate negative values.* From top to bottom: $t = 1500\ s$, $t = 2250\ s$, $t = 3000\ s$, $t = 3750\ s$.

to the passing of the cloud through the main part of the wave pattern is observed at about $t = 4500$ s. This reduction is likewise found in figure 5.6, although being much more pronounced there, especially in the case of $\max(\sigma) = 0.5$.

Summarized, the simulations with ASAM, featuring full bulk micro-physics, provide some justification for the results obtained from the study of the reduced model. As discussed above, there are important issues to address about the correspondence between σ and the initial data for ρ_{vl}. Notwithstanding these problems, the preliminary results presented in this section show noteworthy similarities between the results from the reduced and the full model, although naturally the inherent limitations of the reduced model do not allow it to capture the dynamics in areas where moist convection is triggered. It is confirmed that a passing cloud-

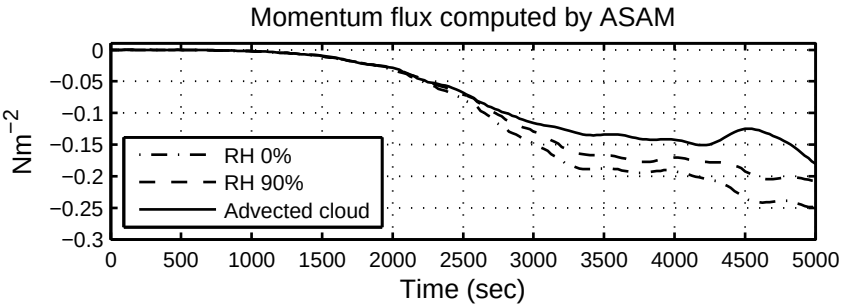

Figure 5.23.: *Net momentum flux over time at* $z = 10$ *km for the passing cloud-packet and reference simulations with* $f \equiv 0.9$ *and* $f \equiv 0$*, corresponding to* 90 % *and* 0 % *relative humidity initially.*

packet significantly alters the wave pattern and, most importantly, that it reduces the generated momentum flux.

Chapter 6.

Weakly Under-Saturated Regime

This chapter presents a modification of the ansatz to address the regime of weak under-saturation. By systematically assuming a small saturation deficit, the higher order displacements indicated by the employed scales can condensate/evaporate enough vapor to affect the saturated area fraction at leading order. Thus in the resulting model σ is a prognostic quantity, leading to nonlinear tower-scale dynamics.

Section 6.1 sketches the modified ansatz. In section 6.2, the same closure strategy as in chapter 2 is employed, but additional approximations are required. The evolution of plane wave amplitudes is analyzed numerically in section 6.3 and the dynamics of the model in terms of energy are discussed. By application of an operator splitting strategy, the numerical scheme described in chapter 4 is extended in section 6.4 and numerical results are presented.

6.1. Leading Order Equations

6.1.1. Dynamic Equations

The expansions of the dynamic quantities as well as rain water and cloud water are identical to those in chapter 2, cf. (2.40), (2.41) and (2.42). Only the expansion of water vapor

$$q_\mathrm{v} = q_\mathrm{vs}^{(0)} + \varepsilon q_\mathrm{v}^{(1)} + \mathcal{O}(\varepsilon^2) \tag{6.1}$$

differs as all-over saturation at leading order is assumed. For simplicity, set $\mathbf{u}^\infty = 0$ for the purpose of this chapter. Following the derivation in chapter 2, all quantities are split into averages and perturbations, see (2.43), (2.44). The resulting leading order equations are the same as in chapter 2, namely (2.45) and (2.47) with $\mathbf{u}^\infty = 0$.

As shown in (2.75) and (2.76), for the employed scales, vertical displacements and hence the amount of condensating or evaporating water are of order $\mathcal{O}(\varepsilon)$. In the presence of a leading order saturation deficit (2.77), this amount is not sufficient to

significantly alter the size of saturated areas. In the derivation at hand, however, according to (6.1), the saturation deficit is of order

$$\delta q_{\mathrm{vs}} \sim \mathcal{O}(\varepsilon), \tag{6.2}$$

so condensation and evaporation of $\mathcal{O}(\varepsilon)$ amounts can exert a leading order influence on the size of saturated regions, cf. figure 2.3.

6.1.2. Micro-Scale Equations

The expansion of the bulk micro-scale equation $(2.14)_1$ yields for $\mathcal{O}(\varepsilon^n)$ and $\mathcal{O}(\varepsilon^{-n+1})$

$$\begin{aligned} C_{\mathrm{d}}^{(-n)} &= 0 \\ C_{\mathrm{d}}^{(-n+1)} &= 0. \end{aligned} \tag{6.3}$$

From (6.1) conclude $\delta q_{\mathrm{vs}}^{(0)} = 0$ so that $(6.3)_1$ is automatically satisfied. Thus $(6.3)_2$ yields

$$C_{\mathrm{d}}^{(-n+1)} = C_{\mathrm{d}}^{**} H_{\circ} \delta q_{\mathrm{vs}}^{(1)} q_{\mathrm{c}}^{(0)} = 0, \tag{6.4}$$

hence two different micro-physical regimes can be distinguished:

- Regime I : $\delta_{\mathrm{v}}^{(1)} = q_{\mathrm{vs}}^{(1)}$, thus $\delta q_{\mathrm{vs}}^{(1)} = 0$
- Regime II: $\delta q_{\mathrm{vs}}^{(1)} > 0$ and $q_{\mathrm{c}}^{(0)} = 0$

While in the original derivation the two micro-physical regimes are saturation / non-saturation at leading order, cf. appendix A.1, assuming $\delta q_{\mathrm{vs}}^{(0)} = 0$ in advance leads to the distinction of saturation / non-saturation at order $\mathcal{O}(\varepsilon)$.

Expanding the micro-scale equations $(2.14)_{2,3}$ yields
$\mathcal{O}(\varepsilon^{-1})$:

$$\begin{aligned} q_{\mathrm{v},\tau}^{(0)} + \mathbf{u}^{(0)} \cdot \nabla_{\eta} q_{\mathrm{v}}^{(0)} &= -C_{\mathrm{d}}^{(-1)} \\ q_{\mathrm{c},\tau}^{(0)} + \mathbf{u}^{(0)} \cdot \nabla_{\eta} q_{\mathrm{c}}^{(0)} &= C_{\mathrm{d}}^{(-1)} - C_{\mathrm{cr}}^{(-1)} \\ q_{\mathrm{r},\tau}^{(0)} + \mathbf{u}^{(0)} \cdot \nabla_{\eta} q_{\mathrm{r}}^{(0)} &= C_{\mathrm{cr}}^{(-1)} \end{aligned} \tag{6.5}$$

$\mathcal{O}(\varepsilon^{0})$:

$$\begin{aligned} q_{\mathrm{v},\tau}^{(1)} + \mathbf{u}^{(1)} \cdot \nabla_{\eta} q_{\mathrm{v}}^{(0)} + \mathbf{u}^{(0)} \cdot \nabla_{\eta} q_{\mathrm{v}}^{(1)} + \mathbf{u}^{(0)} \cdot \nabla_{x} q_{\mathrm{v}}^{(0)} + w^{(0)} q_{\mathrm{v},z}^{(0)} &= -C_{\mathrm{d}}^{(0)} + C_{\mathrm{ev}}^{(0)} \\ q_{\mathrm{c},\tau}^{(1)} + \mathbf{u}^{(1)} \cdot \nabla_{\eta} q_{\mathrm{c}}^{(0)} + \mathbf{u}^{(0)} \cdot \nabla_{\eta} q_{\mathrm{c}}^{(1)} + \mathbf{u}^{(0)} \cdot \nabla_{x} q_{\mathrm{c}}^{(0)} + w^{(0)} q_{\mathrm{c},z}^{(0)} &= C_{\mathrm{d}}^{(0)} - C_{\mathrm{cr}}^{(0)} - C_{\mathrm{ac}}^{(0)} \\ q_{\mathrm{r},\tau}^{(1)} + \mathbf{u}^{(1)} \cdot \nabla_{\eta} q_{\mathrm{r}}^{(0)} + \mathbf{u}^{(0)} \cdot \nabla_{\eta} q_{\mathrm{r}}^{(1)} + \mathbf{u}^{(0)} \cdot \nabla_{x} q_{\mathrm{r}}^{(0)} + w^{(0)} q_{\mathrm{r},z}^{(0)} &= C_{\mathrm{cr}}^{(0)} - C_{\mathrm{ev}}^{(0)} + C_{\mathrm{ac}}^{(0)} \end{aligned} \tag{6.6}$$

It turns out a lot of the source terms on the right hand side vanish, resulting in a noticeably simplified set of equations.

1. Using in $(6.5)_1$ that $q_{\mathrm{v}}^{(0)} = q_{\mathrm{vs}}^{(0)}(z)$ depends only on height yields
$$C_{\mathrm{d}}^{(-1)} = 0. \tag{6.7}$$

2. Also, as $\delta q_{\mathrm{vs}}^{(0)} = 0$ everywhere, the source term related to evaporation rain vanishes
$$C_{\mathrm{ev}}^{(0)} = C_{\mathrm{ev}}^{**} \delta q_{\mathrm{vs}}^{(0)} \sqrt{q_{\mathrm{r}}^{(0)}} = 0. \tag{6.8}$$

3. Adding $(6.5)_2$ and $(6.5)_3$ and employing (6.7) indicates, that the leading order amount of total liquid water $q_{\mathrm{l}}^{(0)} = q_{\mathrm{c}}^{(0)} + q_{\mathrm{r}}^{(0)}$ is conserved
$$q_{\mathrm{l},\tau}^{(0)} + \mathbf{u}^{(0)} \cdot \nabla_\eta q_{\mathrm{l}}^{(0)} = 0. \tag{6.9}$$
By assuming $q_{\mathrm{l}}^{(0)}(\tau = 0) = 0$, it follows that $q_{\mathrm{l}}^{(0)} \equiv 0$ and thus
$$C_{\mathrm{cr}}^{(-1)} = C_{\mathrm{cr}}^{**} q_{\mathrm{c}}^{(0)} q_{\mathrm{r}}^{(0)} = 0. \tag{6.10}$$

4. From (2.16) and $q_{\mathrm{l}}^{(0)} \equiv 0$ conclude
$$C_{\mathrm{ac}}^{(0)} \sim q_{\mathrm{c}}^{(0)} = 0 \Rightarrow C_{\mathrm{ac}}^{(0)} = 0, \tag{6.11}$$

5. as well as
$$C_{\mathrm{cr}}^{(0)} = C_{\mathrm{cr}}^{**} \left(q_{\mathrm{c}}^{(0)} q_{\mathrm{r}}^{(1)} + q_{\mathrm{c}}^{(1)} q_{\mathrm{r}}^{(0)} \right) = 0. \tag{6.12}$$

With the simplifications 1-5, (6.6) becomes

$$\begin{aligned} q_{\mathrm{v},\tau}^{(1)} + \mathbf{u}^{(0)} \cdot \nabla_\eta q_{\mathrm{v}}^{(1)} + w^{(0)} q_{\mathrm{vs},z}^{(0)} &= -C_{\mathrm{d}}^{(0)} \\ q_{\mathrm{c},\tau}^{(1)} + \mathbf{u}^{(0)} \cdot \nabla_\eta q_{\mathrm{c}}^{(1)} &= C_{\mathrm{d}}^{(0)} \\ q_{\mathrm{r},\tau}^{(1)} + \mathbf{u}^{(0)} \cdot \nabla_\eta q_{\mathrm{r}}^{(1)} &= 0 \end{aligned} \tag{6.13}$$

Note that rain water $q_{\mathrm{r}}^{(1)}$ is passively advected by the horizontal flow.

According to [KM06], $q_{\mathrm{vs}}^{(1)} = q_{\mathrm{vs}}^{(1)}(z)$ depends on height only. In regime II it holds that $C_{\mathrm{d}}^{(0)} = 0$, so the final equations read

- Regime I (saturation):

$$\begin{aligned} w^{(0)} q_{\mathrm{vs},z}^{(0)} &= -C_{\mathrm{d}}^{(0)} \\ q_{\mathrm{c},\tau}^{(1)} + \mathbf{u}^{(0)} \cdot \nabla_\eta q_{\mathrm{c}}^{(1)} &= C_{\mathrm{d}}^{(0)}, \end{aligned} \tag{6.14}$$

- Regime II (weak under-saturation):

$$\begin{aligned} q_{\mathrm{v},\tau}^{(1)} + \mathbf{u}^{(0)} \cdot \nabla_\eta q_{\mathrm{v}}^{(1)} &= -w^{(0)} q_{\mathrm{vs},z}^{(0)} \\ q_{\mathrm{c},\tau}^{(1)} + \mathbf{u}^{(0)} \cdot \nabla_\eta q_{\mathrm{c}}^{(1)} &= 0. \end{aligned} \tag{6.15}$$

6.1.3. Total Water Content

Define the first-order total water content as

$$q_{\mathrm{T}}^{(1)} := q_{\mathrm{v}}^{(1)} + q_{\mathrm{c}}^{(1)}. \tag{6.16}$$

By (6.14) and (6.15), $q_{\mathrm{T}}^{(1)}$ satisfies

$$\frac{D^{(\eta)} q_{\mathrm{T}}^{(1)}}{D\tau} = -w^{(0)} q_{\mathrm{vs},z}^{(0)} \tag{6.17}$$

with the micro-scale material derivative defined as

$$\frac{D^{(\eta)}}{D\tau} = \frac{\partial}{\partial \tau} + \mathbf{u}^{(0)} \cdot \nabla_\eta. \tag{6.18}$$

Integration of (6.17) in time yields

$$\begin{aligned} q_{\mathrm{T}}^{(1)}(\tau, \eta) &= q_{\mathrm{T}}^{(1)}(0, \eta) + \int_0^\tau \frac{D^{(\eta)} q_{\mathrm{T}}^{(1)}}{D\tau} \, d\tau' \\ &= q_{\mathrm{T}}^{(1)}(0, \eta) - q_{\mathrm{vs},z}^{(0)} \int_0^\tau w^{(0)}(\tau', \eta) \, d\tau' \\ &= q_{\mathrm{T}}^{(1)}(0, \eta) - q_{\mathrm{vs},z}^{(0)} \xi(\tau, \eta) \end{aligned} \tag{6.19}$$

whereas ξ denotes the vertical displacement, defined as the solution of

$$\frac{D^{(\eta)} \xi}{D\tau} = w^{(0)} \quad \text{with} \quad \xi(0) = 0. \tag{6.20}$$

According to (6.19), $q_{\mathrm{vs}}^{(0)}$ acts as an infinite reservoir from which, in rising parcels, $\mathcal{O}(\varepsilon)$ amounts [cf. (2.76)] are converted either into cloud water $q_{\mathrm{c}}^{(1)}$ in saturated regions [Regime I, cf. (6.14)] or into water vapor $q_{\mathrm{v}}^{(1)}$ in non-saturated regions [Regime II, cf. (6.15))]. If $q_{\mathrm{v}}^{(1)}$ reaches the saturation threshold $q_{\mathrm{vs}}^{(1)}$, the region becomes saturated and further displacement produces $q_{\mathrm{c}}^{(1)}$, i.e. clouds start to form. In a descending parcel, $q_{\mathrm{v}}^{(1)}$ and $q_{\mathrm{c}}^{(1)}$ are deposited back into $q_{\mathrm{vs}}^{(0)}$. If $q_{\mathrm{c}}^{(1)}$ is depleted, the region becomes non-saturated and $q_{\mathrm{v}}^{(1)}$ starts to decrease.

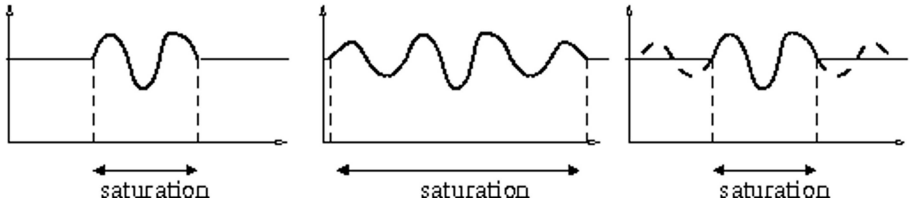

Figure 6.1.: *General structure of micro-scale vertical velocity $\tilde{w}$ at three different times: Initially, $\tilde{w}^{(0)}$ varies only in the small, saturated area* (left)*. As the saturated area enlarges, variations in $\tilde{w}^{(0)}$ can emerge in the now saturated areas* (center)*. As saturated regions become non-saturated again and the saturated spot shrinks* (right)*, variations in $\tilde{w}^{(0)}$ found in formerly saturated areas (dashed line) are neglected and the constant value $\tilde{w}_{\mathrm{us}}$ (thin, solid line) is employed.*

Displacement in Non-Saturated Areas

As explained in section 3.1, the perturbation vertical velocity $\tilde{w}^{(0)}$ and the perturbation potential temperature $\tilde{\theta}^{(3)}$ are constant in non-saturated areas. There, this statement holds for any point η initially located in a non-saturated area, i.e. $H_{\mathrm{q_v}}(\eta) = 0$. Here, in the weakly under-saturated case however, these areas are no longer constant but can become saturated and non-saturated again. Thus the counterpart to (3.10) can now only state

$$\nabla_\eta \tilde{w}^{(0)}(\tau,\eta) = \nabla_\eta \tilde{\theta}^{(3)}(\tau,\eta) = 0 \quad \text{if} \quad H_{\mathrm{q_v}}(\tau',\eta) = 0 \quad \forall \tau' \leq \tau, \tag{6.21}$$

i.e. the gradients are zero in regions that have never reached saturation until time τ.

Neglecting the effect that a non-zero gradient can emerge in regions that are initially non-saturated and become saturated at some point, assume

$$\nabla_\eta \tilde{w}^{(0)}(\tau,\eta) = \nabla_\eta \tilde{\theta}^{(3)}(\tau,\eta) = 0 \; \forall \tau \geq 0 \quad \text{if} \quad H_{\mathrm{q_v}}(0,\eta) = 0, \tag{6.22}$$

cf. figure 6.1. By this approximation, just as in section 3.1, it holds that

$$\begin{aligned} \tilde{w}^{(0)}(\eta,\tau) &= \tilde{w}_{\mathrm{us}} = const. \\ \tilde{\theta}^{(3)}(\eta,\tau) &= \tilde{\theta}_{\mathrm{us}} = const. \; \forall \tau \geq 0 \quad \text{if} \quad H_{\mathrm{q_v}}(0,\eta) = 0. \end{aligned} \tag{6.23}$$

Let the displacement in non-saturated regions ξ_{us} again be defined by (3.13). Employing approximation (6.23), by continuity of $\tilde{w}^{(0)}$,

$$\xi(\eta,\tau) = \xi_{\mathrm{us}}(\tau) \;\; \forall \tau \geq 0 \quad \text{if} \quad H_{\mathrm{q_v}}(0,\eta) = 0. \tag{6.24}$$

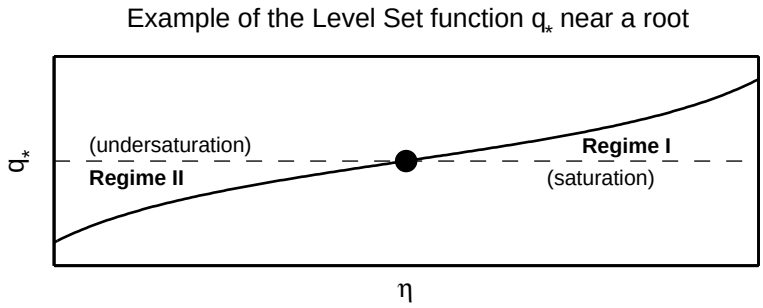

Figure 6.2.: *General structure in the 1-D case of the level set function q_* in the vicinity of a root, indicating the interface between the saturated and the non-saturated regime.*

Level Set Interface Tracking

Define the function

$$q_* := q_{\mathrm{T}}^{(1)} - q_{\mathrm{vs}}^{(1)}. \tag{6.25}$$

By (6.14), (6.15), (6.16) it reads

$$q_* = \begin{cases} q_{\mathrm{c}}^{(1)} \geq 0 : \text{ Regime I} \\ q_{\mathrm{v}}^{(1)} - q_{\mathrm{vs}}^{(1)} \leq 0 : \text{Regime II} \end{cases}. \tag{6.26}$$

So q_* can be interpreted as a level set function, tracking the interface between saturated and non-saturated regions. The interface corresponds to the set of roots of q_*. See [OF02] for an introduction into level set methods. Figure 6.2 sketches q_* for the case of an x-z-slice, where $\eta \in \mathbb{R}$.

By (6.19), q_* satisfies

$$q_*(\tau, \eta) = q_*(0, \eta) - q_{\mathrm{vs},z}^{(0)} \xi(\tau, \eta). \tag{6.27}$$

Employing (6.24), (6.27) can be written

$$q_*(\tau, \eta) = q_*(0, \eta) - q_{\mathrm{vs},z}^{(0)} \xi_{\mathrm{us}}(\tau). \tag{6.28}$$

Applying ∇_η to (6.28) and using that both $q_{\mathrm{vs},z}^{(0)}$ and $q_{\mathrm{vs},z}^{(1)}$ do not depend on η, see [KM06], yields

$$\nabla_\eta q_*(\tau, \eta) = \nabla_\eta q_*(0, \eta). \tag{6.29}$$

Thus the shape of the level set function does not change in time. q_* only moves up- and downward by constant values $q_{\mathrm{vs},z}^{(0)} \xi_{\mathrm{us}}(\tau)$ according to (6.28) as sketched in figure 6.3. In the following, saturated regions are identified with regions where $q_* > 0$. However, because in (6.28) the exact displacement ξ is replaced by ξ_{us}, this involves some degree of approximation, as ξ and ξ_{us} do not exactly coincide in regions that reached saturation and became non-saturated again.

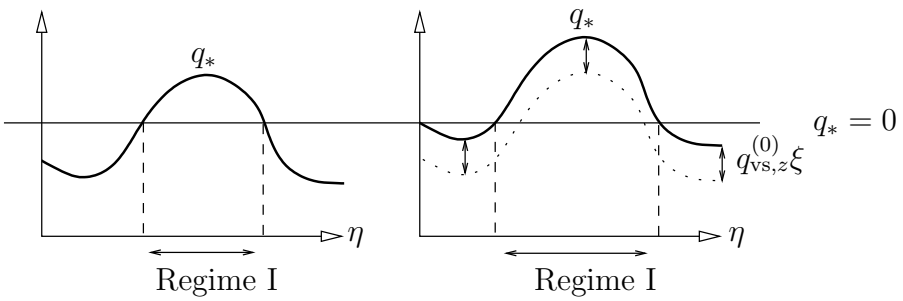

Figure 6.3.: *Change of q_* by upward displacement ξ_{us}. The whole function increases by $q^{(0)}_{vs,z}\xi_{\mathrm{us}}$, but the gradient $\nabla_\eta q_*$ does not change.*

6.2. Closing the Model

In order to close the nonlinear model, analyze first the evolution of a single saturated spot. In a second step, the balance over a finite number of such spots located in one finite interval is computed. The final model is obtained by letting the boundaries of the interval approach $\pm\infty$.

6.2.1. Evolution of an Individual Saturated Spot

Let A_i denote a single saturated spot. Further denote its boundary, i.e. the interface between saturation and non-saturation, by ∂A_i and by $\mathbf{v}_i$ the velocity at which the interface is advected. The evolution equation for the level set function, cf. [OF02], reads

$$\frac{\partial q_*}{\partial \tau} + \mathbf{v}_i \cdot \nabla_\eta q_* = 0. \tag{6.30}$$

Employing (3.13), (6.24) and (6.28), the temporal derivative can be reformulated as

$$\begin{aligned} \frac{\partial q_*}{\partial \tau} &= -q^{(0)}_{\mathrm{vs},z} \frac{\partial \xi_{\mathrm{us}}}{\partial \tau} \\ &= -q^{(0)}_{\mathrm{vs},z} \frac{D\xi_{\mathrm{us}}}{D\tau} \\ &= -q^{(0)}_{\mathrm{vs},z} \left(\bar{w} + \tilde{w}_{\mathrm{us}}\right). \end{aligned} \tag{6.31}$$

Because q_* is positive inside saturated regions and negative outside, the gradient $\nabla_\eta q_*$ on ∂A_i points in the opposite direction of the outer normal vector $\mathbf{n}$ on the interface ∂A_i, thus

$$-\frac{\nabla_\eta q_*}{|\nabla_\eta q_*|} = \mathbf{n}. \tag{6.32}$$

By using (6.31) and (6.32), (6.30) becomes

$$\begin{aligned} \mathbf{v}_i \cdot \nabla_\eta q_* &= q^{(0)}_{\mathrm{vs},z} \left(\bar{w} + \tilde{w}_{\mathrm{us}}\right) \\ \Rightarrow (\mathbf{v}_i \cdot \mathbf{n}) \left|\nabla_\eta q_*\right| &= -q^{(0)}_{\mathrm{vs},z} \left(\bar{w} + \tilde{w}_{\mathrm{us}}\right) \\ \Rightarrow \mathbf{v}_i \cdot \mathbf{n} &= -q^{(0)}_{\mathrm{vs},z} \frac{\bar{w} + \tilde{w}_{\mathrm{us}}}{\left|\nabla_\eta q_*\right|}. \end{aligned} \tag{6.33}$$

According to (6.28), points at the interface are characterized by

$$q_*(\eta, \tau) = 0 \Leftrightarrow q^{(0)}_{\mathrm{vs},z} \xi_{\mathrm{us}} = q_*(\eta, 0) \tag{6.34}$$

and thus solely by the displacement ξ_{us} and the initial distribution of q_*. So for given $q_*(\tau = 0)$, define

$$\Psi_i(\xi_{\mathrm{us}}) := -q^{(0)}_{\mathrm{vs},z} \oint_{\partial A_i} \frac{1}{\left|\nabla_\eta q_*\right|} \, dS. \tag{6.35}$$

Note that $q^{(0)}_{\mathrm{vs},z} < 0$, hence

$$\Psi_i \geq 0. \tag{6.36}$$

The total change of the area of A_i can be evaluated, using (6.33) and (6.35), by

$$\begin{aligned} \frac{D}{D\tau} \int_{A_i} \mathbf{1} \, dV &= \oint_{\partial A_i} \mathbf{v}_i \cdot \mathbf{n} \, dS \\ &= \Psi_i(\xi_{\mathrm{us}}) \left(\bar{w} + \tilde{w}_{\mathrm{us}}\right). \end{aligned} \tag{6.37}$$

6.2.2. Closure of the Micro-Scale Model

According to (2.40), $\mathbf{u}^{(0)}$ does not depend on η and (2.47) can be written as

$$\begin{aligned} \tilde{w}^{(0)}_\tau + \nabla_\eta \cdot \left(\mathbf{u}^{(0)} \tilde{w}^{(0)}\right) &= \tilde{\theta}^{(3)} \\ \tilde{\theta}^{(3)}_\tau + \nabla_\eta \cdot \left(\mathbf{u}^{(0)} \tilde{\theta}^{(3)}\right) + \tilde{w}^{(0)} \Theta^{(2)}_z &= \hat{L} \left(C^{(0)} - \overline{C^{(0)}}\right) \end{aligned} \tag{6.38}$$

with $\mathbf{u}^\infty = 0$. Drop the superscripts of $\mathbf{u}^{(0)}$, $\tilde{w}^{(0)}$ and $\tilde{\theta}^{(3)}$ to streamline notation. Integrating (6.38) over a volume A_i moving at velocity $\mathbf{v}_i$ results in

$$\begin{aligned} \frac{\partial}{\partial \tau} \int_{A_i} \tilde{w} \, d\eta + \oint_{\partial A_i} \tilde{w} \left(\mathbf{u} - \mathbf{v}_i\right) \cdot \mathbf{n} \, dS &= \int_{A_i} \tilde{\theta} \, d\eta \\ \frac{\partial}{\partial \tau} \int_{A_i} \tilde{\theta} \, d\eta + \oint_{\partial A_i} \tilde{\theta} \left(\mathbf{u} - \mathbf{v}_i\right) \cdot \mathbf{n} \, dS + \Theta^{(2)}_z \int_{A_i} \tilde{w} \, d\eta & \\ = \int_{A_i} \hat{L} C^{(0)} \, d\eta - \left|A_i\right| \hat{L} \overline{C^{(0)}}, & \end{aligned} \tag{6.39}$$

see e.g. [TL79]. According to (6.23), $\tilde{w} = \tilde{w}_{\mathrm{us}}$ and $\tilde{\theta} = \tilde{\theta}_{\mathrm{us}}$ are constant in non-saturated regions and thus, by continuity, also on the interface between regime I and II. Thus the surface integrals involving $\mathbf{u}^{(0)}$ vanish and by using (6.37), (6.39) can be reformulated as

$$\begin{aligned} \frac{\partial}{\partial \tau} \int_{A_i} \tilde{w}\, d\eta - \tilde{w}_{\mathrm{us}} \left(\bar{w} + \tilde{w}_{\mathrm{us}}\right) \Psi_i &= \int_{A_i} \tilde{\theta}\, d\eta \\ \frac{\partial}{\partial \tau} \int_{A_i} \tilde{\theta}\, d\eta - \tilde{\theta}_{\mathrm{us}} \left(\bar{w} + \tilde{w}_{\mathrm{us}}\right) \Psi_i + \Theta_z^{(2)} \int_{A_i} \tilde{w}\, d\eta & \\ = \int_{A_i} \hat{L} C^{(0)}\, d\eta - |A_i| \hat{L} \overline{C^{(0)}}. & \end{aligned} \tag{6.40}$$

Summate (6.40) for a finite number of saturated spots $A_1, \ldots, A_n$, all contained in some domain $D(\eta_0) := [-\eta_0, \eta_0]^d$. As in (2.73), it is $d = 1$ for the case of a x-z-plane and $d = 2$ for the full three-dimensional case. Using that $H_{\mathrm{q_v}}|_{D(\eta_0)}$ is the characteristic function of $\bigcup_{i=1}^n A_i \subset D(\eta_0)$ and thus

$$\sum_{i=1}^{n} \int_{A_i} f d\eta = \int_{D(\eta_0)} H_{\mathrm{q_v}} f d\eta \tag{6.41}$$

for any integrable function f, the overall balance reads

$$\begin{aligned} \frac{\partial}{\partial \tau} \int_{D(\eta_0)} H_{\mathrm{q_v}} \tilde{w}\, d\eta - \tilde{w}_{\mathrm{us}} \left(\bar{w} + \tilde{w}_{\mathrm{us}}\right) \sum_{i=1}^{n} \Psi_i &= \int_{D(\eta_0)} H_{\mathrm{q_v}} \tilde{\theta}\, d\eta \\ \frac{\partial}{\partial \tau} \int_{D(\eta_0)} H_{\mathrm{q_v}} \tilde{\theta}\, d\eta - \tilde{\theta}_{\mathrm{us}} \left(\bar{w} + \tilde{w}_{\mathrm{us}}\right) \sum_{i=1}^{n} \Psi_i + \Theta_z^{(2)} \int_{D(\eta_0)} H_{\mathrm{q_v}} \tilde{w}\, d\eta = & \\ \int_{D(\eta_0)} H_{\mathrm{q_v}} \hat{L} C^{(0)}\, d\eta - \hat{L} \overline{C^{(0)}} \int_{D(\eta_0)} H_{\mathrm{q_v}}\, d\eta. & \end{aligned} \tag{6.42}$$

Employing (6.8), the source term in (A.13) simplifies to

$$C^{(0)} = H_{\mathrm{q_v}} C_{\mathrm{d}}^{(0)}. \tag{6.43}$$

By multiplying $(6.14)_1$ first by $\hat{L}$, cf. (2.54), then by $H_{\mathrm{q_v}}$ and employing the moist adiabat equation (2.53), (6.43) becomes

$$\hat{L} C^{(0)} = H_{\mathrm{q_v}} \hat{L} C_{\mathrm{d}}^{(0)} = -H_{\mathrm{q_v}} \left(\bar{w} + \tilde{w}\right) \hat{L} q_{\mathrm{vs},z}^{(0)} = H_{\mathrm{q_v}} \left(\bar{w} + \tilde{w}\right) \Theta_z^{(2)}. \tag{6.44}$$

Define the weighted averages

$$\begin{aligned} w' &:= \lim_{\eta_0\to\infty} \frac{\int_{D(\eta_0)} H_{\mathrm{q_v}}\tilde{w}\ d\eta}{\int_{D(\eta_0)} \mathbf{1}\ d\eta} = \overline{H_{\mathrm{q_v}}\tilde{w}} \\ \theta' &:= \lim_{\eta_0\to\infty} \frac{\int_{D(\eta_0)} H_{\mathrm{q_v}}\tilde{\theta}\ d\eta}{\int_{D(\eta_0)} \mathbf{1}\ d\eta} = \overline{H_{\mathrm{q_v}}\tilde{\theta}} \\ \sigma &:= \lim_{\eta_0\to\infty} \frac{\int_{D(\eta_0)} H_{\mathrm{q_v}}\ d\eta}{\int_{D(\eta_0)} \mathbf{1}\ d\eta} = \overline{H_{\mathrm{q_v}}} \\ \Psi &:= \lim_{n\to\infty} \frac{\sum_{i=1}^{n}\Psi_i}{\int_{[-n,n]^d}\mathbf{1}\ d\eta}. \end{aligned} \tag{6.45}$$

Dividing (6.42) by $\int_{D(\eta_0)}\mathbf{1}\ d\eta$, employing $H_{\mathrm{q_v}}^2 = H_{\mathrm{q_v}}$ and applying the limit $\eta_0\to\infty$ yields after rearranging terms

$$\begin{aligned} w'_\tau - \tilde{w}_{\mathrm{us}}\left(\bar{w}^{(0)} + \tilde{w}_{\mathrm{us}}\right)\Psi &= \theta' \\ \theta'_\tau - \tilde{\theta}_{\mathrm{us}}\left(\bar{w}^{(0)} + \tilde{w}_{\mathrm{us}}\right)\Psi + \sigma\Theta_z^{(2)}w' &= \sigma(1-\sigma)\Theta_z^{(2)}\bar{w}^{(0)} \end{aligned} \tag{6.46}$$

whereas arbitrary permutability of integrals and limits is assumed. Using (3.12) finally yields

$$\begin{aligned} w'_\tau &= \theta' + \frac{w'}{1-\sigma}\left(\frac{w'}{1-\sigma} - \bar{w}^{(0)}\right)\Psi \\ \theta'_\tau + \sigma\Theta_z^{(2)}w' &= \sigma(1-\sigma)\Theta_z^{(2)} + \frac{\theta'}{1-\sigma}\left(\frac{w'}{1-\sigma} - \bar{w}^{(0)}\right)\Psi. \end{aligned} \tag{6.47}$$

Further compute, using (6.37) and $(6.45)_3$,

$$\begin{aligned} \frac{D\sigma}{D\tau} &= \lim_{\eta_0\to\infty}\frac{D}{D\tau}\frac{\int_{D(\eta_0)} H_{\mathrm{q_v}}\ d\eta}{\int_{D(\eta_0)}\ d\eta} \\ &= \lim_{n\to\infty}\frac{1}{\int_{[-n,n]^d}\mathbf{1}\ d\eta}\sum_{i=1}^{n}\frac{D}{D\tau}\int_{A_i}\mathbf{1}\ d\eta \\ &= \lim_{n\to\infty}\frac{1}{\int_{[-n,n]^d}\mathbf{1}\ d\eta}\sum_{i=1}^{n}\oint_{\partial A_i}\mathbf{v}_i\cdot\mathbf{n}\ dS \\ &= \lim_{n\to\infty}\frac{1}{\int_{[-n,n]^d}\mathbf{1}\ d\eta}\sum_{i=1}^{n}\left(\bar{w}^{(0)} + \tilde{w}_{\mathrm{us}}\right)\Psi_i \\ &= -\left(\frac{w'}{1-\sigma} - \bar{w}\right)\Psi \end{aligned} \tag{6.48}$$

Thus (6.47) can be compactly written as

$$\begin{aligned} w'_\tau + \frac{\sigma_\tau}{1-\sigma} w' &= \theta' \\ \theta'_\tau + \sigma\Theta_z^{(2)} w' + \frac{\sigma_\tau}{1-\sigma}\theta' &= \sigma(1-\sigma)\Theta_z^{(2)}. \end{aligned} \tag{6.49}$$

By employing $(6.45)_3$, averaging (6.44) yields

$$\overline{\hat{L}C^{(0)}} = \sigma\Theta_z^{(2)}\bar{w}^{(0)} + \Theta_z^{(2)} w'. \tag{6.50}$$

6.2.3. Summary

The full nonlinear model with unknowns $u, \bar{w}, \bar{\theta}, \pi, w', \theta', \sigma, \xi_{\text{us}}$ consists of the large-scale equations $(2.70)_{1-4}$ with $\mathbf{u}^\infty = 0$, (3.13), (6.48) and (6.49).

Linearized anelastic moist dynamics:

$$\begin{aligned} \mathbf{u}_\tau + \nabla_x \pi &= 0 \\ \bar{w}_\tau + \pi_z &= \bar{\theta} \\ \bar{\theta}_\tau + (1-\sigma)\Theta_z^{(2)}\bar{w} &= \Theta_z^{(2)} w' \\ \rho^{(0)}\nabla_x \cdot \mathbf{u} + \left(\rho^{(0)}\bar{w}\right)_z &= 0 \end{aligned}$$

Averaged nonlinear tower-scale dynamics: (6.51)

$$\begin{aligned} w'_\tau + \frac{\sigma_\tau}{1-\sigma} w' &= \theta' \\ \theta'_\tau + \sigma\Theta_z^{(2)} w' + \frac{\sigma_\tau}{1-\sigma}\theta' &= \sigma(1-\sigma)\Theta_z^{(2)}\bar{w} \\ \sigma_\tau &= \xi_{\text{us},\tau}\Psi \\ \xi_{\text{us},\tau} &= \bar{w} - \frac{w'}{1-\sigma} \end{aligned}$$

Note that in the limit of infinitely steep gradients of the level set function q_*, by (6.35), $\Psi \to 0$ and the original linear model (2.70) with $\mathbf{u}^\infty = 0$ and $\bar{C}_- = 0$ is retrieved.

According to (6.36) and (6.45) $\Psi \geq 0$ obtains. Thus for an upward moving parcel, i.e. $\xi_{\text{us},\tau} > 0$, the saturated area fraction σ increases. This corresponds to the increase of q_* indicated by (6.28), enlarging the area where $q_* > 0$.

The other way round, in a descending parcel with $\xi_{\text{us},\tau} < 0$, σ decreases, corresponding to reducing q_* and thus diminishing size of areas where $q_* > 0$.

6.3. Properties of the Nonlinear Model

This section points out some properties of the nonlinear model (6.51). In order to avoid double subscripts denote ξ_{us} simply as ξ in the following and refer to it as displacement.

6.3.1. The Function $\Psi(\xi)$

The functions Ψ_i and Ψ defined in (6.35) and (6.45) would have to be computed from some initial distribution of cloud water and water vapor. However, the purpose of the analysis presented here is not to deliver precise quantitative results, but to explore the qualitative behavior of (6.51). Thus an idealized function Ψ is derived ensuring that σ adopts values between zero and unity for all displacements ξ.

Denote by G the antiderivative of Ψ, then by $(6.51)_{7,8}$

$$\begin{aligned}\sigma(\tau) &= \sigma(0) + \int_0^\tau \sigma_\tau d\tau \\ &= \sigma(0) + \int_0^\tau \Psi(\xi)\xi_\tau d\tau \\ &= \sigma(0) + \int_0^\tau \frac{DG(\xi)}{D\tau} d\tau \\ &= \sigma(0) + G(\xi(\tau)) - G(0),\end{aligned} \tag{6.52}$$

as $\xi(0) = 0$.

Set G to

$$G(\xi) = \alpha \left(\operatorname{erf}\left(\frac{\xi - \xi_0}{\beta} \right) \right) + \gamma, \tag{6.53}$$

whereas erf is the antiderivative of the Gaussian distribution. It holds that

$$\operatorname{erf}\left(\frac{\xi - \xi_0}{\beta} \right) \approx 1 \quad \text{for} \quad \frac{\xi - \xi_0}{\beta} >> 0 \tag{6.54}$$

and

$$\operatorname{erf}\left(\frac{\xi - \xi_0}{\beta} \right) \approx -1 \quad \text{for} \quad \frac{\xi - \xi_0}{\beta} << 0. \tag{6.55}$$

Requiring

$$\begin{aligned}\sigma(0) + \alpha\,(1 + \gamma) - G(0) &\stackrel{!}{=} 1 \\ \sigma(0) + \alpha\,(-1 + \gamma) - G(0) &\stackrel{!}{=} 0\end{aligned} \tag{6.56}$$

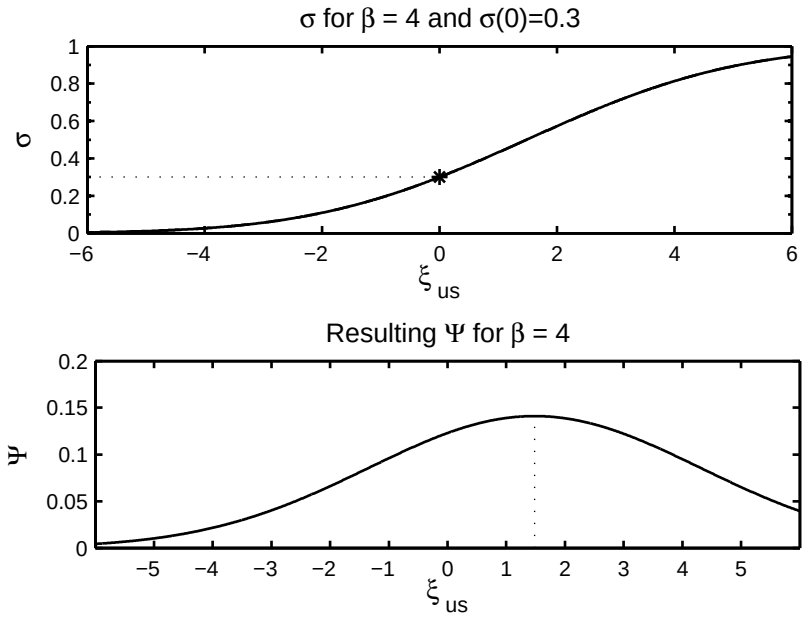

Figure 6.4.: *The antiderivative* $G(\xi) = \sigma$ (upper)*, as well as the resulting coupling function* Ψ (lower) *for* $\beta = 4$*. The horizontal dashed line in the upper figures indicates the initial value* $\sigma(0) = 0.3$*.*

leads to

$$\alpha = \gamma = \frac{1}{2} \quad \text{and} \quad \xi_0 = -\beta \, \text{erf}^{-1}\left(2\sigma(0) - 1\right). \tag{6.57}$$

Thus

$$G(\xi) = \frac{1}{2}\left(\text{erf}\left(\frac{\xi - \xi_0}{\beta}\right)\right) + \frac{1}{2}, \tag{6.58}$$

resulting in

$$G(0) = \sigma(0) \tag{6.59}$$

and by (6.52)

$$\sigma(\tau) = G(\xi(\tau)) = \frac{1}{2}\,\text{erf}\left(\frac{\xi - \xi_0}{\beta}\right) + \frac{1}{2} \Longrightarrow 0 \leq \sigma \leq 1. \tag{6.60}$$

Further, (6.58) yields

$$\Psi(\xi) = \frac{1}{\sqrt{\pi}\beta} \exp\left(-\left(\frac{\xi - \xi_0}{\beta}\right)^2\right). \tag{6.61}$$

As demonstrated by (6.60), choosing Ψ according to (6.61) yields values of σ between zero and unity for arbitrary displacements ξ.

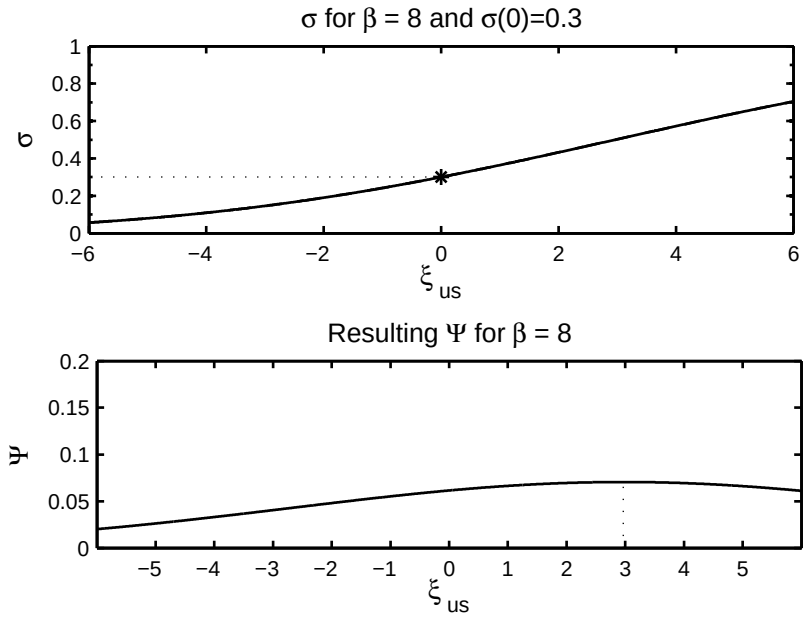

Figure 6.5.: *The antiderivative* $G(\xi) = \sigma$ (upper)*, as well as the resulting coupling function* Ψ (lower) *for* $\beta = 8$*. The horizontal dashed line in the upper figures indicates the initial value* $\sigma(0) = 0.3$*.*

The validity of approximation (6.24) is based upon the assumption that non-zero gradients $\nabla_\eta \tilde{w}$ emerging in regions initially non-saturated but becoming saturated at some time and non-saturated again have negligible effect. To justify this assumption set $\beta \gg 1$ here, resulting in small overall variations of the size of saturated regions.

Figure 6.4 sketches σ (upper figure) as well as the corresponding Ψ (lower figure) for $\beta = 4$, $\sigma(0) = 0.3$. Figure 6.5 sketches the same for $\beta = 8$. As required, σ varies between zero and unity depending on ξ_{us}. For $\beta = 4$, the dependence of σ on the displacement is stronger and smaller values of ξ_{us} suffice to bring σ close to zero and unity, respectively. For $\beta = 4$ and $\xi_{\text{us}} \approx -3$, σ reduces to about 16% of its initial value, so there assuming small variations becomes questionable, but for displacements of about $\xi_{\text{us}} \pm 1$, σ changes by about 30% compared to $\sigma(0)$. This can reasonably be considered a small variation.

Note that Ψ also depends on the large-scale coordinates x and z. Thus β is not required to be constant over the domain, but can depend on x and z. The derivation of the nonlinear model assumes all-over weak under-saturation, however letting $\beta(x, z)$ adopt sufficiently large values in specific regions allows to effectively include the original linear dynamics in (6.51), because the nonlinear dependence of σ on ξ is then negligible.

6.3.2. Energy

The tower-scale potential and kinetic energy defined in (3.41) and discussed for the linear model in section 3.2 can also be defined and analyzed for the nonlinear model. As σ depends on τ, the derivative of E'_{pot} reads

$$\begin{aligned}\frac{\partial E'_{\text{pot}}}{\partial \tau} &= \frac{\rho^{(0)}}{2}\left[\frac{2\theta'\theta'_\tau\sigma\Theta_z^{(2)} - (\theta')^2\sigma_\tau\Theta_z^{(2)}}{(\sigma\Theta_z^{(2)})^2}\right] \\ &= \frac{\rho^{(0)}\theta'\theta'_\tau}{\sigma\Theta_z^{(2)}} - \frac{\rho^{(0)}}{2}\frac{(\theta')^2}{2\sigma\Theta_z^{(2)}}\frac{\sigma_\tau\Theta_z^{(2)}}{\sigma\Theta_z^{(2)}} \\ &= \frac{\rho^{(0)}\theta'\theta'_\tau}{\sigma\Theta_z^{(2)}} - E'_{\text{pot}}\frac{\sigma_\tau}{\sigma}.\end{aligned} \tag{6.62}$$

Multiplying $(6.51)_6$ with $\rho^{(0)}\theta'$ and using (6.62) results in

$$\frac{\partial E'_{\text{pot}}}{\partial \tau} + \frac{\sigma_\tau}{\sigma}E'_{\text{pot}} + \frac{2\sigma_\tau}{1-\sigma}E'_{\text{pot}} = -\rho^{(0)}\theta'w' + (1-\sigma)\,\rho^{(0)}\theta'\bar{w}. \tag{6.63}$$

Multiplication of $(6.51)_6$ with $\rho^{(0)}w'$ and further simplification of (6.63) yields

$$\begin{aligned}\partial_\tau E'_{\text{kin}} + \sigma_\tau\left[\frac{2}{1-\sigma}\right]E'_{\text{kin}} &= \rho^{(0)}w'\theta' \\ \partial_\tau E'_{\text{pot}} + \sigma_\tau\left[\frac{1+\sigma}{\sigma\,(1-\sigma)}\right]E'_{\text{pot}} &= -\rho^{(0)}w'\theta' + (1-\sigma)\,\rho^{(0)}\theta'\bar{w}.\end{aligned} \tag{6.64}$$

The right hand side terms represent conversion between tower-scale potential and kinetic energy plus the potential energy generated from large-scale displacements as discussed in section 3.2.

Two new terms arise, that are not present in the energy equations (3.42), (3.43) in the linear model. Depending on the sign of the coefficient, the new terms cause either an exponential growth or decay of E'_{kin} and E'_{pot}. Because the terms in squared brackets are always positive, the sign solely depends on the sign of σ_τ, which itself depends solely on ξ_τ. If $\sigma_\tau < 0$, i.e. the parcel descends, energy is generated, while if $\sigma_\tau > 0$, i.e. the parcel is rising, energy is consumed. As shown in subsection 6.3.3, the nonlinearity leads to a disparity between the energy generated and consumed over the course of one oscillation resulting in a net increase of energy over time.

Analogously to the computation in (6.62) it can be shown that the large-scale potential energy $(3.35)_2$ satisfies

$$\frac{\partial E_{\text{pot}}}{\partial \tau} = \rho^{(0)}\frac{\bar{\theta}\bar{\theta}_\tau}{(1-\sigma)\,\Theta_z^{(2)}} + \frac{\sigma_\tau}{1-\sigma}E_{\text{pot}} \tag{6.65}$$

and thus, multiplying $(6.51)_3$ with $\rho^{(0)}\bar{\theta}$,

$$\partial_\tau E_{\text{pot}} - \frac{\sigma_\tau}{1-\sigma} E_{\text{pot}} = -\rho^{(0)}\bar{\theta}\bar{w} + \rho^{(0)}\frac{\bar{\theta}w'}{1-\sigma}. \tag{6.66}$$

Contrary to the mechanism for micro-scale potential energy, the additional term in (6.66) generates potential energy if a parcel rises, i.e. $\sigma_\tau > 0$ and consumes E_{pot} if it descends, i.e. $\sigma_\tau < 0$. The equation for the large-scale kinetic energy $(3.35)_1$ is not altered by the time-dependence of σ, so E_{kin} satisfies (3.36).

6.3.3. Evolution of a Plane Wave

Likewise to the analysis presented in subsection 3.3.2, seek solutions of the form

$$\phi(x,z,\tau) = \hat{\phi}(\tau)\exp\left(i(kx+mz)\right)\exp(\mu z) \tag{6.67}$$

for the nonlinear model (6.51) whereas $\phi \in \left\{u, \bar{w}, \bar{\theta}, \pi, w', \theta', \sigma, \xi\right\}$. As in subsection 3.3.1, $\exp(\mu z)$ with $\mu = 0.5$ describes the amplitude increase with height caused by decreasing density. For the purpose of simpler notation, the hats in the $\hat{\phi}$ terms are dropped in this subsection. For example, σ denotes $\hat{\sigma}$.

Insert (6.67) into (6.51) and combine $(6.51)_1$ to $(6.51)_4$ into a single equation

$$\left(k^2+m^2+0.25\right)\bar{w}_{\tau\tau} + (1-\sigma)\,\Theta_z^{(2)}k^2\bar{w} = \Theta_z^{(2)}k^2 w'. \tag{6.68}$$

Note that this is identical to $(3.55)_1$ obtained for $\bar{w}$ in subsection 3.3.2. By introducing the auxiliary variable $\chi := \bar{w}_\tau$, (6.68) can be rewritten as a first order system and combined with the micro-scale equations $(6.51)_{5-8}$ into a closed system of ordinary differential equations

$$\begin{aligned}
\bar{w}_\tau &= \chi \\
\chi_\tau &= \left(k^2+m^2+0.25\right)^{-1}\left(-(1-\sigma)\Theta_z^{(2)}k^2\bar{w} + \Theta_z^{(2)}k^2 w'\right) \\
w'_\tau &= \theta' - \frac{w'}{1-\sigma}\xi_\tau\Psi \\
\theta'_\tau &= -\sigma\Theta_z^{(2)}w' + \sigma(1-\sigma)\Theta_z^{(2)}\bar{w} - \frac{\theta'}{1-\sigma}\xi_\tau\Psi \\
\sigma_\tau &= \xi_\tau\Psi \\
\xi_\tau &= -\left(\frac{w'}{1-\sigma} - \bar{w}\right).
\end{aligned} \tag{6.69}$$

For $\Psi = 0$ (6.69) reduces to the first order system corresponding to (3.55). The system (6.69) is solved employing the ode solver *ode45* in MATLAB, but identical solutions are obtained by other MATLAB solvers like *ode23tb* or *ode15s*.

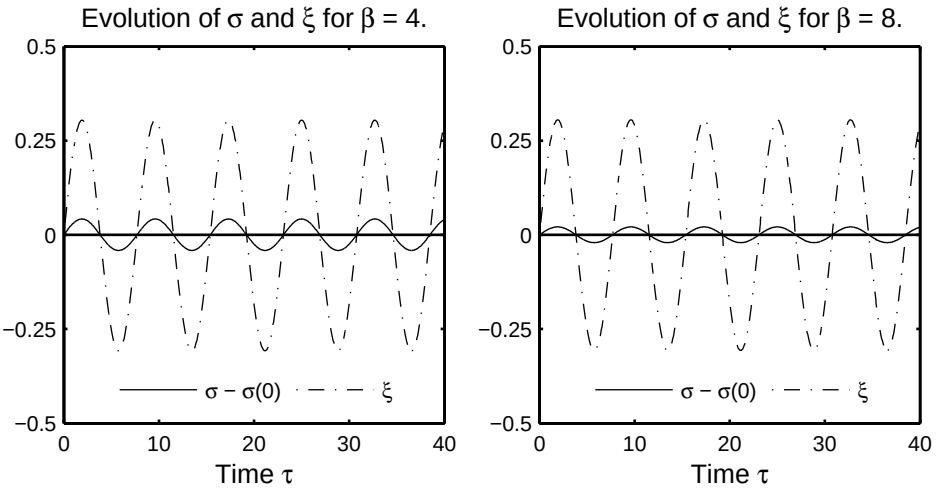

Figure 6.6.: *Evolution of the amplitudes of the saturated area fraction σ and the displacement ξ for $\beta = 4$* (left) *and $\beta = 8$* (right).

Set $\chi(0) = w'(0) = \theta'(0) = \xi(0) = 0$. Set $\sigma(0) = 0.4$ and prescribe an initial large-scale induced velocity of $\bar{w} = 0.25$. Two solutions are computed, one for $\beta = 4$ and one for $\beta = 8$. Denote the vertical velocity inside saturated towers by

$$w_{\mathrm{I}} = \bar{w} + w' \tag{6.70}$$

and the vertical velocity in non-saturated areas between the towers as

$$w_{\mathrm{II}} = \bar{w} + w_{\mathrm{us}} = \bar{w} - \frac{w'}{1-\sigma}, \tag{6.71}$$

cf. (3.12).

Figure 6.6 shows the difference $\sigma - \sigma(0)$ and the displacement ξ over time for $\beta = 4$ (left) and $\beta = 8$ (right). The displacement performs identical oscillations between about ± 0.3 in both simulations. σ oscillates around its initial value $\sigma(0)$ in both figures, but with larger amplitude for $\beta = 4$. In both cases, the amplitudes are constant in τ.

A different picture arises in figure 6.7, displaying the vertical velocity w_{I} inside the convective towers and the velocity w_{II} in the non-saturated regions between them. While w_{II} oscillates with constant amplitude for both values of β, the vertical velocity w_{I} amplifies over time. The amplification is stronger for $\beta = 4$ and in general increases as β decreases.

Identical solutions computed over a very long time interval are shown in figure 6.8 and confirm constant amplitudes for ξ, σ and w_{II} as well as a seemingly linear

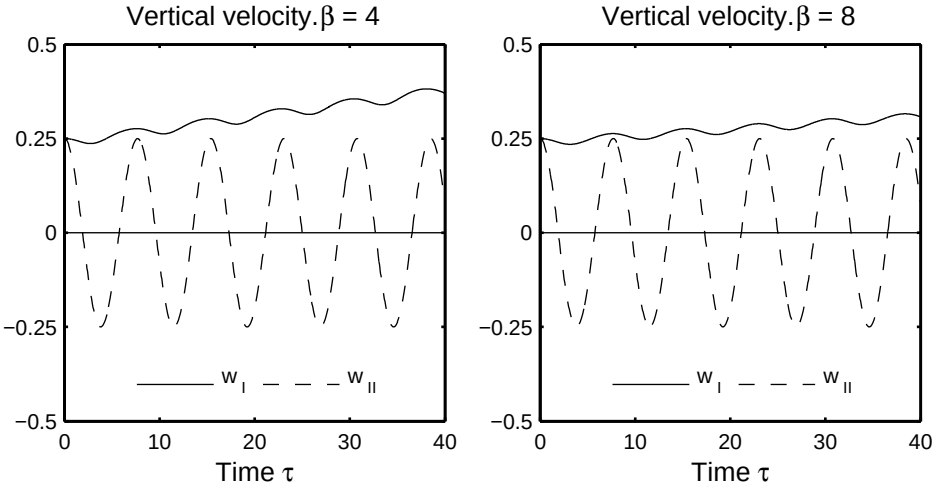

Figure 6.7.: *Evolution of the vertical velocities* w_{I} *(saturated regions) and* w_{II} *(non-saturated regions) for* $\beta = 4$ (left) *and* $\beta = 8$ (right).

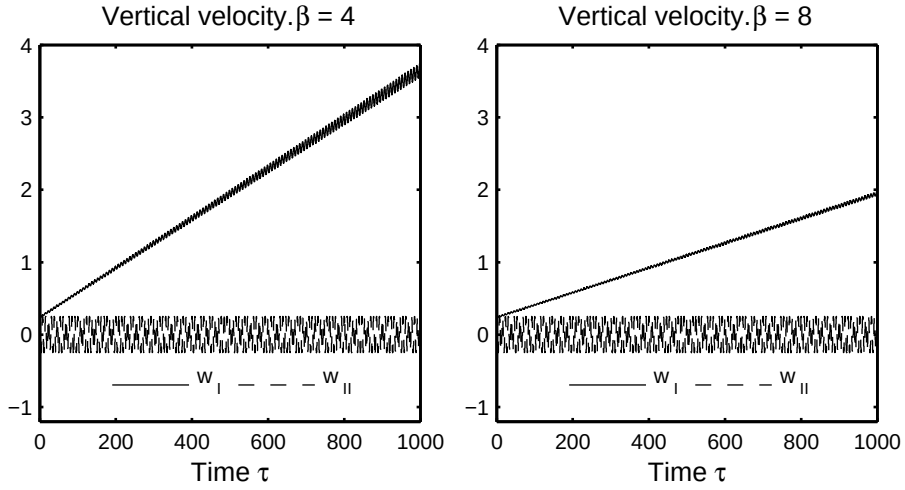

Figure 6.8.: *Evolution of the vertical velocities* w_{I} *(saturated regions) and* w_{II} *(non-saturated regions) for* $\beta = 4$ (left) *and* $\beta = 8$ (right) *until* $\tau = 1000$.

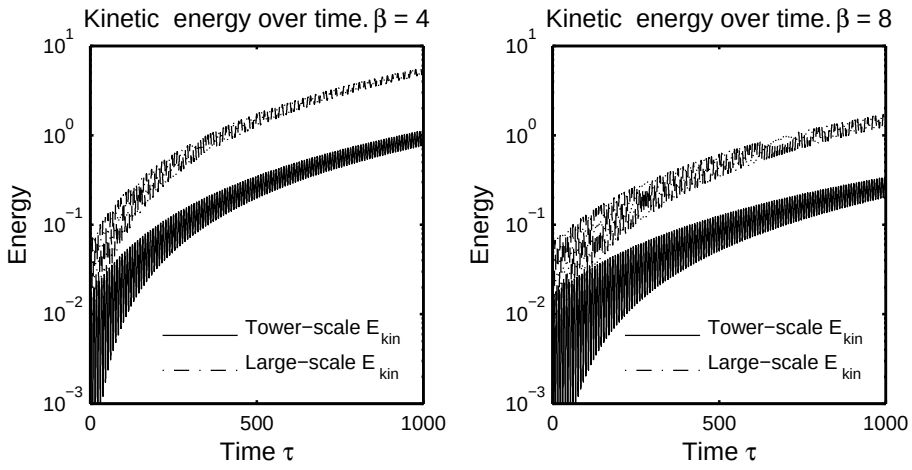

Figure 6.9.: *Evolution large-scale kinetic energy* E_{kin} *and tower-scale kinetic energy* E'_{kin} *for* $\beta = 4$ (left) *and* $\beta = 8$ (right). *The vertical axis is scaled logarithmically.*

increase in w_{I} over time. Thus the nonlinear model features a weak instability, where interactions of up- and downdrafts with saturated areas lead to amplification of updrafts inside convective towers.

Figure 6.9 reveals that the amplification of w_{I} is accompanied by growing values of large-scale and tower-scale kinetic energy. The corresponding potential energies (not shown), however, remain bounded.

Generation of Tower-Scale Energy

The weak instability can be linked to the energy equations (6.64). Denote

$$F_{\text{kin}} = -\sigma_\tau \left[\frac{2}{1-\sigma}\right] E'_{\text{kin}} \ , \quad F_{\text{pot}} = -\sigma_\tau \left[\frac{1+\sigma}{\sigma(1-\sigma)}\right] E'_{\text{pot}} + (1-\sigma)\,\rho^{(0)}\bar{w}\theta'. \tag{6.72}$$

Let τ_0 denote the starting time of one oscillation, i.e. $\xi(\tau_0) = 0$ and increasing. Figure 6.10 shows how F_{kin} contributes to E'_{kin} and F_{pot} to E'_{pot} over the course of one oscillation for $\beta = 4$ (left) and $\beta = 8$ (right). The dashed and dashed-dotted curves denote values of the cumulative integrals

$$\int_{\tau_0}^{\tau} F_{\text{kin}}\, dt \quad \text{and} \quad \int_{\tau_0}^{\tau} F_{\text{pot}}\, dt \tag{6.73}$$

respectively. After completing the oscillation, both terms provide a small but non-zero contribution. Hence with every completed oscillation the total energy increases a little bit, leading to a noticeable growth of the vertical velocity w_{I}

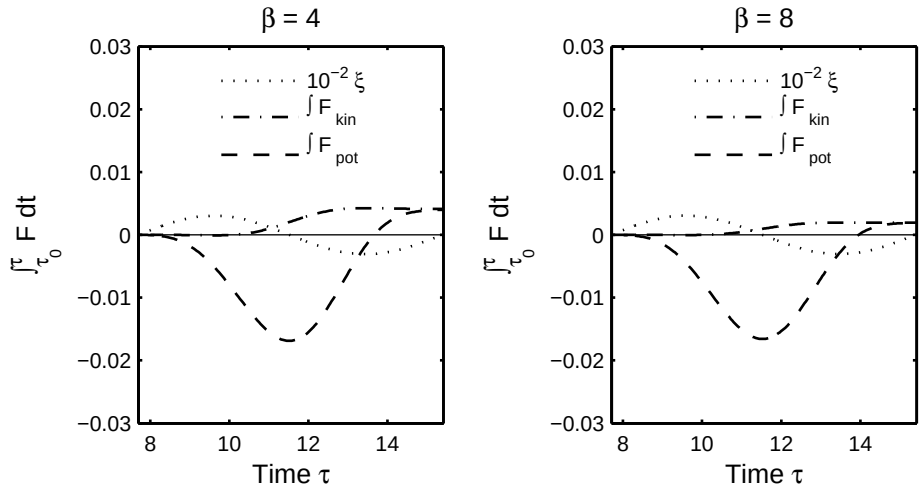

Figure 6.10.: *Contribution of F_{kin} and F_{pot} over one oscillation for $\beta = 4$* (left) *and $\beta = 8$* (right). *The dotted line shows the displacement ξ, scaled by 10^{-2}. The dashed line shows the cumulative integral $\int_{\tau_0}^{\tau} F_{\mathrm{kin}}(t)\,dt$, the dash-dotted line shows $\int_{\tau_0}^{\tau} F_{\mathrm{pot}}(t)\,dt$. τ_0 is the minimum value on the τ-axis and corresponds to the starting time of the oscillation.*

over longer periods of time. As the potential energies E_{pot} and E'_{pot} remain both bounded while E'_{kin} as well as E_{kin} grow, the surplus potential energy is apparently converted into kinetic energy. Note that the surplus in figure 6.10 reduces with increasing β and appears to vanish as $\beta \to \infty$. A similar plot for the linear problem presented in subsection 3.3.2 (not shown) confirms that the contributions at the end of the oscillation are zero there.

Parameters Governing the Instability

As figure 6.8 suggests a linear growth of w_{I}, a rough measure of the growth rate of w_{I} can be obtained fitting a linear model to the calculated values using linear regression. This is achieved employing the MATLAB function *regress*. Tabular 6.1 lists the slopes of the obtained linear fit for different initial values of σ and different values of β multiplied by 10^3. The initial large-scale velocity is always $\bar{w} = 0.25$ while $\chi = w' = \theta' = \xi = 0$ initially. Again the solution is computed over a large time interval until $\tau = 1000$.

In general, a more sensitive dependence of σ on ξ, i.e. reduced β, leads to larger slopes. There is some "optimal" initial value of about $\sigma = 0.2$ for $\beta = 2$, $\beta = 4$ and $\sigma = 0.3$ for $\beta = 8$, leading to a maximum slope with decreased slopes for initial values of σ above or below. Further tests not documented here indicate, that the

Initial σ	est. slope, $\beta = 2$	est. slope, $\beta = 4$	est. slope, $\beta = 8$
0.1	6.672	3.415	1.779
0.2	8.223	4.248	2.247
0.3	8.062	4.197	2.256
0.4	7.190	3.775	2.068
0.5	6.040	3.208	1.798
0.7	3.626	2.011	1.209
0.9	1.464	0.926	0.659

Table 6.1.: *Slope of linear functions fitted to values of w_{I}, obtained using the linear regression* regress *in MATLAB. Values are multiplied by 10^3 and rounded to three digit numbers for easier comparison.*

initial value for σ causing the strongest growth depends on the initial $\bar{w}$, but more involved dependencies may also exist. In the time-dependent numerical solution presented in subsection 6.4.2 however, the observed effect of the nonlinearity is weak but in line with the order of magnitude to be expected from the growth rates in table 6.1 over the length of time of the presented simulation.

6.4. Non-Stationary Solutions of the Nonlinear System

6.4.1. Extending the Numerical Scheme

By using an operator splitting technique, see section 7.3 in [Dur99], the scheme presented in chapter 4 for the solution of the linear system can be extended to also solve the nonlinear model. Because the operator splitting is not compatible with a multi-step method, the Adams-Bashforth-3 timestepping (4.2) is replaced by a one-step Runge-Kutta-4 scheme, while the spatial discretization remains (4.17). This combination is investigated in [Dur91] too, and also found to be viable, but to produce stronger artificial dissipation and to be less efficient than the multi-step version. Denote by ϕ the vector

$$\phi := \left(u, \bar{w}, \bar{\theta}, w', \theta', \sigma, \xi\right)^{\mathrm{T}} \tag{6.74}$$

containing the prognostic unknowns from model (6.51). Further define

$$\mathcal{L}_1(\phi) := -\begin{pmatrix} 0 \\ 0 \\ 0 \\ \frac{w'}{1-\sigma}\Psi \\ \frac{\theta'}{1-\sigma}\Psi \\ \Psi \\ 1 \end{pmatrix} \left(\frac{w'}{1-\sigma} - \bar{w}\right) \tag{6.75}$$

and

$$\mathcal{L}_2(\phi) := \begin{pmatrix} 0 \\ \bar{\theta} \\ -(1-\sigma)\,\Theta_z^{(2)}\bar{w} + \Theta_z^{(2)}w' \\ \theta' \\ -\sigma\Theta_z^{(2)}w' + \sigma(1-\sigma)\bar{w}\Theta_z^{(2)} \\ 0 \\ 0 \end{pmatrix} \tag{6.76}$$

so that the prognostic part of the full nonlinear model (6.51) can compactly be written as

$$\frac{D\phi}{D\tau} = \mathcal{L}_1(\phi) + \mathcal{L}_2(\phi) \tag{6.77}$$

As in the linear case, an equation for the pressure π is derived employing the anelastic constraint $(6.51)_4$. First, the discrete nonlinear micro-scale problem approximating

$$\frac{D\phi}{D\tau} = \mathcal{L}_1(\phi) \tag{6.78}$$

is integrated by an implicit midpoint rule from τ to $\tau + \Delta\tau$, using the initial value ϕ^n and delivering an intermediate value ϕ^s. Using ϕ^s as initial value, the discrete linear problem approximating

$$\frac{D\phi}{D\tau} = \mathcal{L}_2(\phi) \tag{6.79}$$

is updated from τ to $\tau + \Delta\tau$, employing an explicit, fourth-order Runge-Kutta scheme. The obtained predicted solution $\phi^{n,*}$ is then corrected by the pressure π^n, obtained by solving an elliptic equation similar to (4.11). Summarized, the sequence of steps reads

$$\phi^n \xrightarrow{\mathcal{L}_1} \phi^s \xrightarrow{\mathcal{L}_2} \phi^{n,*} \xrightarrow{\text{projection}} \phi^{n+1}. \tag{6.80}$$

In detail, the steps of the numerical scheme read

Nonlinear step:

$$\begin{aligned} k_1^{(1)} &= \mathcal{L}_1(\phi^n + \frac{\Delta\tau}{2}k_1) \\ \phi^s &= \phi^n + \Delta\tau k_1^{(1)} \end{aligned} \tag{6.81}$$

Linear step:

$$\begin{aligned} k_1^{(2)} &= \phi^s \\ k_2^{(2)} &= \phi^s + \frac{\Delta\tau}{2}\mathcal{L}_2(k_1^{(2)}) \\ k_3^{(2)} &= \phi^s + \frac{\Delta\tau}{2}\mathcal{L}_2(k_2^{(2)}) \\ k_4^{(2)} &= \phi^s + \Delta\tau\mathcal{L}_2(k_3^{(2)}) \\ \phi^{n,*} &= \phi^s + \Delta t\left(\frac{1}{6}k_1^{(2)} + \frac{1}{3}k_2^{(2)} + \frac{1}{3}k_3^{(2)} + \frac{1}{6}k_4^{(2)}\right) \end{aligned} \tag{6.82}$$

Poisson problem:

$$\left(\rho^{(0)}\pi_x\right)_x + \left(\rho^{(0)}\pi_z\right)_z = \left(\rho^{(0)}u^{n,*}\right)_x + \left(\rho^{(0)}\bar{w}^{n,*}\right)_z$$

Correction:

$$\begin{aligned} u^{n+1} &= u^{n,*} - \pi_x^n \\ w^{n+1} &= w^{n,*} - \pi_z^n \end{aligned} \tag{6.83}$$

The nonlinear equation for $k_1^{(1)}$ is solved by an exact Newton iteration, run until the change in the solution is below a prescribed threshold or until a set number of maximum iteration steps is reached. The Jacobian of $\mathcal{L}_1$ is computed analytically and evaluated in every iteration step.

6.4.2. Wave-Cloud Interactions

Similar to section 5.7, the presented simulation places a perturbation of large-scale potential temperature between two cloud-packets. The domain is $[-4,4]\times[0,1.25]$ with the damping layer located between $z=1$ and $z=1.25$. The initial value for the large-scale potential temperature is

$$\bar{\theta}(x,z,\tau=0) = \bar{\theta}_0 \exp\left(-\left[\left(\frac{x}{\sigma_x}\right)^2 + \left(\frac{z-0.5}{\sigma_z}\right)^2\right]\right) \tag{6.84}$$

with $\bar{\theta}_0 = 2.5$, $\sigma_x = \sigma_z = 0.01$, while the initial value for σ reads

$$\sigma(x,z,0) = \sigma_0 \sin\left(\pi\left(z-0.5\right)\right)^2 \begin{cases} \sin\left(\pi\left(x+2\right)\right)^2 & : x \in [-2.5,-1.5] \\ \sin\left(\pi\left(x-2\right)\right)^2 & : x \in [1.5,2.5] \\ 0 & : \text{otherwise} \end{cases} \tag{6.85}$$

with $\sigma_0 = 0.2$. Both distributions are sketched in figure 6.11. The distribution of $\beta(x,z)$ is chosen such, that β reaches a set minimum value $\beta_{\min}$ inside the clouds, i.e. where $\sigma > 0$, but adopts values of $\beta \approx 100$ outside.

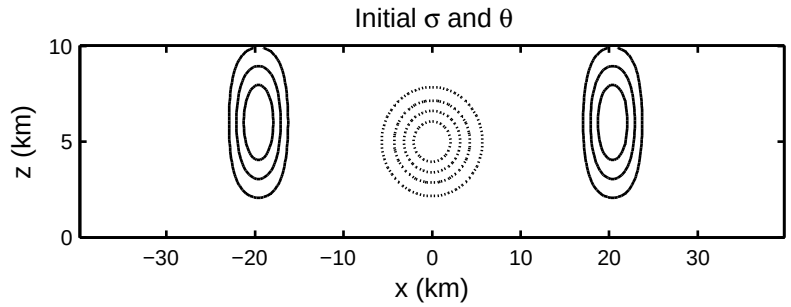

Figure 6.11.: *Initial distribution of σ (solid lines) and $\bar{\theta}$ (dotted lines). The intervals between isolines are* 0.05 *for σ and* 0.5 *for $\bar{\theta}$.*

The timestep is $\Delta\tau = 0.02$, the horizontal resolution is $\Delta x = 0.04$, the vertical $\Delta z = 0.02$ corresponding to 200×60 nodes. Two simulations are run, one with $\beta_{\min} = 8$, the other with $\beta_{\min} = 4$, i.e. a more sensitive dependence of the saturated area fraction on displacement inside the cloud packets. Additionally, to asses the influence of a varying σ, a reference simulation is run, where the nonlinear part in the micro-scale dynamics is turned off, i.e. the nonlinear step (6.81) is skipped.

Figure 6.12 shows the evolution of σ over time at the center of the right cloud, i.e. approximately at $(2, 0.7)$. It demonstrates how σ is perturbed from its initial value of $\sigma(0) = 0.2$ by the incoming waves. The amplitudes are larger for the more sensitive dependence with $\beta_{\min} = 4$ than for $\beta_{\min} = 8$. In the reference simulation without nonlinear micro-physics, σ remains constant over time.

Figure 6.13 shows the difference Δw_{I} between the moduli of the saturation vertical velocities w_{I} in the simulation with nonlinear micro-physics and the reference solution along a horizontal cut through $z = 0.5$. Positive Δw_{I} indicates amplification of up- or downdrafts by the nonlinear dynamics while negative Δw_{I} indicates damping. The constant horizontal dotted lines indicate positive or negative w_{I} in the reference simulation. At $\tau = 10$, a downdraft extends over the full size of the cloud-packet. The presence of the nonlinear dynamics damps the downdraft and the damping is stronger for $\beta = 4$ than for $\beta = 8$. In the figure in the center, an updraft is located in some part of the cloud-packets while a downdraft is found in the in the outer parts. The nonlinear dynamics amplify the updraft and damp the downdraft and again the effect is more pronounced for $\beta = 4$ than for $\beta = 8$. Finally, at $\tau = 30$ the cloud-packet is occupied by an updraft amplified by the nonlinear micro-physics. Slightly amplified downdrafts are located right behind and in front of the cloud-packet.

Summarized the nonlinear compared to the linear micro-physics in all figures amplifies updrafts while damping downdrafts inside the clouds. However, the differences are of the order of 0.05 m s^{-1}. The absolute values of the saturated velocities

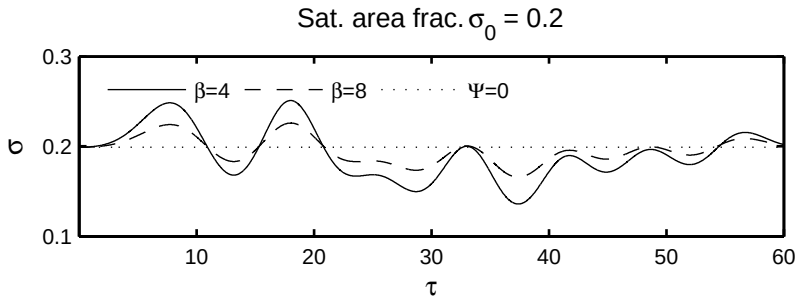

Figure 6.12.: *Evolution of σ at the center of the right cloud-packet. $\Psi = 0$ denotes the reference simulation without nonlinear micro-physics.*

w_{I} are about 2 m s^{-1} in all three simulations, so the effect is only of the order of a few percent.

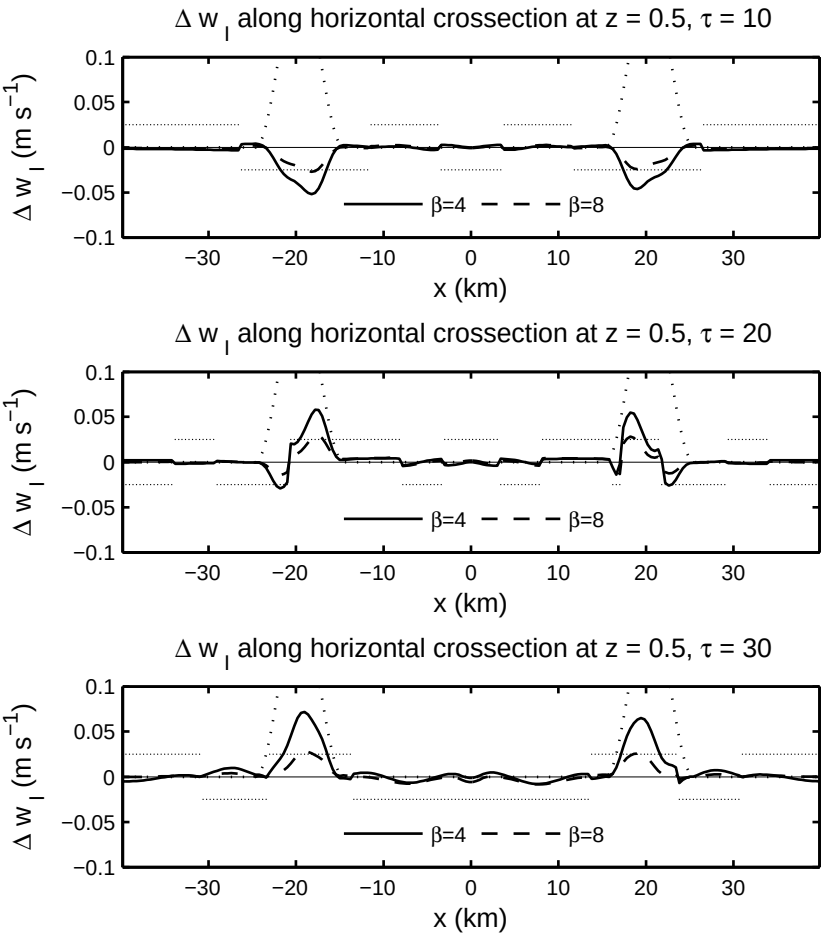

Figure 6.13.: *Difference between the moduli of saturation vertical velocities w_{I} in the simulation with nonlinear micro-physics and the reference simulation across a horizontal cross section at $z^* = 5$ km at $\tau = 10$, $\tau = 20$, $\tau = 30$. Positive values indicate amplification by the nonlinear tower-scale dynamics while negative values indicate damping. The dotted line indicates the constant σ in the reference solution. The horizontally distributed dots indicate updrafts (dots above zero) or downdrafts (dots below zero).*

Chapter 7.

Summary

This thesis presents the derivation, analysis and extension of a model describing propagation of internal gravity waves in an atmosphere that contains deep convective hot towers. The essential moisture-related parameter occurring in the equations is the saturated area fraction over the lengthscale of the cloud-towers in a horizontal slice. If the saturated area fraction is zero, the model reduces to the well-known linearized anelastic equations.

One essential result of the analysis is that moisture can significantly reduce the net vertical flux of horizontal momentum. This flux is closely related to gravity wave drag (GWD), i.e. the force exerted by breaking internal waves on mid-atmospheric flows. Global circulation models employed for weather forecasting as well as climate modelling require parameterizations of GWD in order to be able to produce realistic flows in the higher atmosphere. Incorporating the effect of moisture on momentum flux and thus GWD in such parameterizations might help to improve their level of realism.

Another important hypothesis emerging from the presented model is the introduction of a lower cut-off horizontal wave number by moisture below which modes turn from propagating to evanescent. While propagating modes cause a constant momentum flux with height, the momentum flux for evanescent modes is zero. Modes with small horizontal wave numbers, i.e. near-hydrostatic modes, contribute significantly to GWD, so the lower cut-off has a potentially strong effect on wave drag.

Moisture is also found to create critical layers in flows that are non-critical under dry conditions. As critical layers play a central role in the conversion of momentum flux into drag, this result is likewise of possible interest for the development of GWD parameterizations.

Further results include the derivation of the system's dispersion relation, showing that moisture reduces the range of accessible frequencies. Analyzing the group velocity of the model demonstrates that moisture inhibits propagation of wave-packets and energy transport by waves. Also, it reduces the angle of propagation of wave-packets. A series of steady-state solutions is presented, demonstrating the

cut-off for single mode solutions as well as the effect of moisture on a wave pattern excited from a Witch of Agnesi and consisting of a superposition of numerous modes. A significant reduction of net vertical flux of horizontal momentum is indicated in this example. Qualitative approximate solutions in the vicinity of critical layers are derived. A reformulation of the model demonstrates, that the arising averaged small-scale equations can be interpreted as a wave exciting oscillator and it is shown that the net tower-scale dynamics constitute a forcing for Eulerian pseudo-momentum.

A discretization of the model is introduced to compute approximate, time-dependent solutions. The analytically obtained results for steady-state solutions are confirmed numerically for unsteady solutions, demonstrating again the lower cut-off and providing a more detailed investigation of solutions in the presence of critical layers. Examples are shown, demonstrating how small-scale dynamics and evaporating rain in the model excite large-scale gravity waves. A simulation is presented, investigating how a pattern of mountain waves is disturbed by an advected cloud-packet. Damping of wave amplitudes behind the cloud as well as amplification inside it are found. Also, the momentum flux is again strongly reduced as the cloud-packet passes through the wave pattern. Another simulation demonstrates how waves excited from an initial perturbation in large-scale potential temperature are modulated as they propagate through two cloud-packets, placed in some distance from the initial perturbation. Again an amplification of amplitudes inside the clouds and reduced amplitudes behind them are found. The simulation also shows the reduced propagation velocity of the excited wave-packet inside of clouds.

In order to confirm some of the results obtained from the mathematical and numerical analysis of the reduced model, a code solving the compressible Euler equations in combination with a full bulk micro-physics model is employed. Some effort is made to emulate the parameter describing the tower-scale saturated area fraction arising in the reduced model, but several open questions remain at this point. A simulation is run, employing a setup similar to the advected cloud-packet. Despite noticeable differences, some results from the reduced model can be confirmed, most importantly the reduction of momentum flux by the presence of the cloud-packet although the effect is less pronounced than in the reduced model.

In the original model, the saturation deficit in non-saturated regions is of order unity. As vertical displacements are higher order on the employed timescale, the amount of released or evaporated condensate is not sufficient to affect the tower-scale saturated area fraction at leading order, thus saturated regions act as a wave-modulating background but are not affected by waves in return. By assuming weak under-saturation in advance, i.e. a systematically small saturation deficit, the model is extended so that the tower-scale saturated area fraction does nonlinearly depend on vertical displacements. Introducing a level-set function to approximately track the interface between saturated and non-saturated regions allows to derive an expression for the rate of change of the size of an individual

saturated spot. This result is then employed to compute a closed, nonlinear set of equations, in which the tower-scale saturated area fraction is no longer constant but now becomes a prognostic quantity, depending on the vertical displacement. The original linear model is contained in the nonlinear model as a special case.

An analysis of the evolution of plane wave solutions of the nonlinear model reveals a mechanism causing growing vertical velocities in saturated regions. This growth is linked to nonlinear terms arising in the energy equations, generating a small amount of small-scale energy over each oscillation of a parcel. Employing an operator splitting strategy allows to extend the numerical scheme developed for the linear model to the nonlinear case. A simulation is presented where again a perturbation in potential temperature is placed between to cloud-packets such that the excited waves interact with the saturated areas. It demonstrates that the nonlinear micro-physics amplify updrafts while damping downdrafts compared to the linear model. However, the effects observed in the presented example are only of the order of a few percent.

The derivation of the original linear model presented at the beginning of this thesis employs the framework for systematic development of reduced models presented in [Kle04, Kle08, Kle10] and is based on results from [MK03, KM06]. The used ansatz features time- and lengthscales corresponding to the regime of non-hydrostatic, non-rotating internal gravity waves plus a second horizontal micro-scale corresponding to the typical diameter of deep convective towers. By applying weighted averages conditioned on the small-scale towers, the resulting leading order equations can be closed analytically without requiring further approximations besides adopting a specific asymptotic regime. The final model describes flows on the lengthscales of internal waves but includes net effects from tower-scale dynamics. These are in turn described by two additional equations for the conditional averages over the perturbations of vertical velocity and potential temperature.

Numerous starting points for possible future research emerge during the presented analysis. A logical next step would be a thorough attempt to verify the findings from the analysis of the reduced model by further experiments with a full bulk micro-physic model. Further, as the arising saturated area fraction is reminiscent of the cloud cover fraction computed in GCMs, an attempt could be made to link these two quantities and develop a parameterization of orographic wave drag that takes into account the effect of modulation of internal waves by moisture. Also, the tower-scale dynamics provide a source term for pseudo-momentum absent in the dry anelastic model. Pseudo-momentum is the central quantity in the analysis of the effect of wave-dynamics on mean flow, cf. [Büh09], and and attempt could be made to perform such an analysis with the pseudo-momentum equation forced by the tower-scale dynamics. Finally, by replacing the bulk warm micro-physics model with a bulk model that includes ice phase as presented for example by [Gra99], it might be possible to extend the model's applicability to cold clouds like e.g. mid-latitude clouds.

Appendix A.

Appendix

A.1. Key Steps of the Derivation

A.1.1. Leading Order Equations from Dynamics

Inserting the expansions (2.40), (2.41) into the non-dimensional dynamic equations (2.9) and the expansion (2.42) into the bulk micro-physic equations (2.14) yields the subsequently presented leading order equations. Note that because of the two horizontal coordinates η and x in the model, the horizontal gradient is modified in the following way

$$\nabla_{||} \mapsto \nabla_x + \varepsilon^{-1}\nabla_\eta \tag{A.1}$$

Further, $(2.9)_{2,3}$ are multiplied by ε^4.

Below, the leading order equations arising from (2.9) are summarized.

Horizontal momentum

$$\begin{aligned}
\mathcal{O}(\epsilon^2) \;&:\; \nabla_\eta p^{(3)} = 0 \\
\mathcal{O}(\epsilon^3) \;&:\; \rho^{(0)}\mathbf{u}_\tau^{(0)} + \rho^{(0)}\mathbf{u}_{\tau'}^{(1)} + \rho^{(0)}\mathbf{u}^\infty \cdot \nabla_x \mathbf{u}^{(0)} + \rho^{(0)}\mathbf{u}^\infty \cdot \nabla_\eta \mathbf{u}^{(1)} \\
&\quad + \nabla_x p^{(3)} + \nabla_\eta p^{(4)} = 0
\end{aligned} \tag{A.2}$$

The second equation can be rewritten as

$$\rho^{(0)}\mathbf{u}_\tau^{(0)} + \rho^{(0)}\mathbf{u}^\infty \cdot \nabla_x \mathbf{u}^{(0)} + \nabla_x p^{(3)} = -\left[\rho^{(0)}\mathbf{u}_{\tau'}^{(1)} + \rho^{(0)}\mathbf{u}^\infty \cdot \nabla_\eta \mathbf{u}^{(1)} + \nabla_\eta p^{(4)}\right]. \tag{A.3}$$

Integrate this equation along a characteristic $\tau' + u^\infty \eta = const.$ and employ sub-linear growth condition for the higher order quantities $u^{(1)}$ and $p^{(4)}$ to conclude that the right hand side has to vanish. So (A.3) simplifies to

$$\rho^{(0)}\mathbf{u}_\tau^{(0)} + \rho^{(0)}\mathbf{u}^\infty \cdot \nabla_x \mathbf{u}^{(0)} + \nabla_x p^{(3)} = 0. \tag{A.4}$$

Dividing by $\rho^{(0)}(z)$ and using that by $(\text{A.2})_1$, $p^{(3)}$ is independent of η, yields

$$\mathbf{u}_\tau^{(0)} + \mathbf{u}^\infty \cdot \nabla_x \mathbf{u}^{(0)} + \nabla_x \pi = 0 \tag{A.5}$$

whereas

$$\pi := \frac{p^{(3)}}{\rho^{(0)}} \tag{A.6}$$

is the Newtonian limit form of the Exner function.

Vertical momentum

$$\begin{aligned}
\mathcal{O}(1) &: p_z^{(0)} = -\rho^{(0)} \\
\mathcal{O}(\epsilon) &: p_z^{(1)} = -\rho^{(1)} \\
\mathcal{O}(\epsilon^2) &: \rho^{(0)} w_{\tau'}^{(0)} + \rho^{(0)} \mathbf{u}^\infty \cdot \nabla_\eta w^{(0)} + p_z^{(2)} = -\rho^{(2)} \\
\mathcal{O}(\epsilon^3) &: \rho^{(0)} w_{\tau'}^{(1)} + \rho^{(0)} \mathbf{u}^\infty \cdot \nabla_\eta w^{(1)} + \rho^{(1)} w_{\tau'}^{(0)} + \rho^{(1)} \mathbf{u}^\infty \cdot \nabla_\eta w^{(0)} \\
&\quad + \rho^{(0)} w_\tau^{(0)} + \rho^{(0)} \mathbf{u}^\infty \cdot \nabla_x w^{(0)} + \rho^{(0)} \mathbf{u}^{(0)} \cdot \nabla_\eta w^{(0)} + p_z^{(3)} = -\rho^{(3)}
\end{aligned} \tag{A.7}$$

Assume $\rho^{(1)} = 0$ here and employ again sublinear growth condition. $(\text{A.7})_4$ then becomes

$$\rho^{(0)} w_\tau^{(0)} + \rho^{(0)} \mathbf{u}^\infty \cdot \nabla_x w^{(0)} + \rho^{(0)} \mathbf{u}^{(0)} \cdot \nabla_\eta w^{(0)} + p_z^{(3)} = -\rho^{(3)}. \tag{A.8}$$

As shown in [KM06], the leading order density and pressure read $\rho^{(0)} = p^{(0)} = \exp(-z)$ in the Newtonian limit $(\gamma - 1) = \mathcal{O}(\varepsilon)$. Employing this and the equation of state yields

$$\pi_z = \frac{p_z^{(3)}}{\rho^{(0)}} + \frac{p^{(3)}}{\rho^{(0)}} = \frac{p_z^{(3)}}{\rho^{(0)}} + \frac{\rho^{(3)}}{\rho^{(0)}} - \theta^{(3)}. \tag{A.9}$$

In dividing (A.8) by $\rho^{(0)}$ and using (A.9) one finally obtains

$$w_\tau^{(0)} + \mathbf{u}^\infty \cdot \nabla_x w^{(0)} + \mathbf{u}^{(0)} \cdot \nabla_\eta w^{(0)} + \pi_z = \theta^{(3)}. \tag{A.10}$$

Mass

$$\rho^{(0)} \nabla_\eta \cdot \mathbf{u}^{(1)} + \rho^{(0)} \nabla_x \cdot \mathbf{u}^{(0)} + \left(\rho^{(0)} w^{(0)} \right)_z = 0 \tag{A.11}$$

Potential temperature

$$\begin{aligned}
\mathcal{O}(\epsilon^3) \;&:\; \theta^{(3)}_{\tau'} + \mathbf{u}^\infty \cdot \nabla_\eta \theta^{(3)} = 0 \\
\mathcal{O}(\epsilon^4) \;&:\; \theta^{(3)}_{\tau} + \theta^{(4)}_{\tau'} + \mathbf{u}^\infty \cdot \nabla_x \theta^{(3)} + \mathbf{u}^\infty \cdot \nabla_\eta \theta^{(4)} + \mathbf{u}^{(0)} \cdot \nabla_\eta \theta^{(3)} + w^{(0)} \theta^{(2)}_z \\
&\qquad = \frac{L^{**}\Gamma^{**} q^{**}_{\mathrm{vs}}}{p_0} \left(H_{\mathrm{q_v}} C^{(0)}_{\mathrm{d}} + (H_{\mathrm{q_v}} - 1) C^{(0)}_{\mathrm{ev}} \right)
\end{aligned} \tag{A.12}$$

assuming there are no external sources of heat, i.e. $\tilde{S}^\epsilon_\theta = 0$. Again, the advective derivative of $\theta^{(4)}$ along $\tau' - \eta$ characteristics is eliminated by sublinear growth condition, so $(\mathrm{A.12})_2$ simplifies to

$$\begin{aligned}
&\theta^{(3)}_{\tau} + \mathbf{u}^\infty \cdot \nabla_x \theta^{(3)} + \mathbf{u}^{(0)} \cdot \nabla_\eta \theta^{(3)} + w^{(0)} \theta^{(2)}_z \\
&\qquad = \frac{L^{**}\Gamma^{**} q^{**}_{\mathrm{vs}}}{p_0} \left(H_{\mathrm{q_v}} C^{(0)}_{\mathrm{d}} + (H_{\mathrm{q_v}} - 1) C^{(0)}_{\mathrm{ev}} \right).
\end{aligned} \tag{A.13}$$

Note that for $\mathbf{u}^\infty = 0$ the leading order equations (A.5), (A.10), (A.11) and (A.13) become the leading order equations derived in [KM06].

A.1.2. Leading Order Equations from Bulk Micro-Physics

From the equation for the transport of water vapor arise the following equations

$$\begin{aligned}
\mathcal{O}(\epsilon^{-n}) \;&:\; C^{(-n)}_{\mathrm{d}} \sim C^{**}_{\mathrm{d}} \delta q^{(0)}_{\mathrm{vs}} H_\circ q^{(0)}_{\mathrm{c}} = 0 \\
\mathcal{O}(\epsilon^{-n+1}) \;&:\; C^{(-n+1)}_{\mathrm{d}} \sim C^{**}_{\mathrm{d}} \delta q^{(1)}_{\mathrm{vs}} H_\circ q^{(0)}_{\mathrm{c}} = 0 \\
\mathcal{O}(\epsilon^{-n+2}) \;&:\; C^{(-n+2)}_{\mathrm{d}} \sim C^{**}_{\mathrm{d}} \delta q^{(2)}_{\mathrm{vs}} H_\circ q^{(0)}_{\mathrm{c}} = 0
\end{aligned} \tag{A.14}$$

with

$$\delta q_{\mathrm{vs}} = q_{\mathrm{vs}} - q_{\mathrm{v}}. \tag{A.15}$$

Equation $(\mathrm{A.14})_1$ allows to distinguish two regimes with respect to the micro-physics: The regime of leading order saturation where δq_{vs} is nonzero only at higher orders and the non-saturated regime where $q^{(0)}_{\mathrm{c}} = 0$, i.e. the cloud water mixing ratio is zero at leading order. The equations for the two regimes are summarized below.

Saturated air

$$
\begin{aligned}
&q^{(2)}_{\mathrm{vs},\tau'} + \mathbf{u}^{\infty} \cdot \nabla_{\eta} q^{(2)}_{\mathrm{vs}} + w^{(0)} q^{(0)}_{\mathrm{vs,z}} = -C^{(0)}_{\mathrm{d}} \\
&q^{(1)}_{\mathrm{c},\tau'} + \mathbf{u}^{\infty} \cdot \nabla_{\eta} q^{(1)}_{\mathrm{c}} = 0 \\
&q^{(2)}_{\mathrm{c},\tau'} + \mathbf{u}^{\infty} \cdot \nabla_{\eta} q^{(2)}_{\mathrm{c}} + q^{(1)}_{\mathrm{c},\tau} + \mathbf{u}^{\infty} \cdot \nabla_{x} q^{(1)}_{\mathrm{c}} + \mathbf{u}^{(0)} \cdot \nabla_{\eta} q^{(1)}_{\mathrm{c}} = C^{(0)}_{\mathrm{d}} - C^{(0)}_{\mathrm{cr}} \\
&q^{(0)}_{\mathrm{r},\tau'} + \mathbf{u}^{\infty} \cdot \nabla_{\eta} q^{(0)}_{\mathrm{r}} = 0 \\
&q^{(1)}_{\mathrm{r},\tau'} + \mathbf{u}^{\infty} \cdot \nabla_{\eta} q^{(1)}_{\mathrm{r}} + q^{(0)}_{\mathrm{r},\tau} + \mathbf{u}^{\infty} \cdot \nabla_{x} q^{(0)}_{\mathrm{r}} + \mathbf{u}^{(0)} \cdot \nabla_{\eta} q^{(0)}_{\mathrm{r}} = 0
\end{aligned}
\tag{A.16}
$$

Again by using sublinear growth condition, the equations simplify to

$$
\begin{aligned}
&- w^{(0)} q^{(0)}_{\mathrm{vs,z}} = C^{(0)}_{\mathrm{d}} \\
&q^{(1)}_{\mathrm{c},\tau} + \mathbf{u}^{\infty} \cdot \nabla_{x} q^{(1)}_{\mathrm{c}} + \mathbf{u}^{(0)} \cdot \nabla_{\eta} q^{(1)}_{\mathrm{c}} = C^{(0)}_{\mathrm{d}} - C^{(0)}_{\mathrm{cr}} \\
&q^{(0)}_{\mathrm{r},\tau} + \mathbf{u}^{\infty} \cdot \nabla_{x} q^{(0)}_{\mathrm{r}} + \mathbf{u}^{(0)} \cdot \nabla_{\eta} q^{(0)}_{\mathrm{r}} = 0
\end{aligned}
\tag{A.17}
$$

The saturation vapor mixing ratio expands as

$$
q_{\mathrm{vs}} = q^{(0)}_{\mathrm{vs}}(z) + \varepsilon q^{(1)}_{\mathrm{vs}}(z) + \varepsilon^2 q^{(2)}_{\mathrm{vs}}(\eta, x, z, \tau', \tau) + \mathcal{O}(\varepsilon^3). \tag{A.18}
$$

See [KM06] for the derivation.

Non-saturated air

$$
\begin{aligned}
&q^{(0)}_{\mathrm{v},\tau'} + \mathbf{u}^{\infty} \cdot \nabla_{\eta} q^{(0)}_{\mathrm{v}} = 0 \\
&q^{(1)}_{\mathrm{v},\tau'} + \mathbf{u}^{\infty} \cdot \nabla_{\eta} q^{(1)}_{\mathrm{v}} + q^{(0)}_{\mathrm{v},\tau} + \mathbf{u}^{\infty} \cdot \nabla_{x} q^{(0)}_{\mathrm{v}} + \mathbf{u}^{(0)} \cdot \nabla_{\eta} q^{(0)}_{\mathrm{v}} = 0 \\
&q^{(1)}_{\mathrm{c},\tau'} + \mathbf{u}^{\infty} \cdot \nabla_{\eta} q^{(1)}_{\mathrm{c}} = 0 \\
&q^{(1)}_{\mathrm{c},\tau} + \mathbf{u}^{\infty} \cdot \nabla_{\eta} q^{(1)}_{\mathrm{c}} + \mathbf{u}^{(0)} \cdot \nabla_{\eta} q^{(1)}_{\mathrm{c}} + q^{(2)}_{\mathrm{c},\tau'} + \mathbf{u}^{\infty} \cdot \nabla_{\eta} q^{(2)}_{\mathrm{c}} = -C^{(0)}_{\mathrm{cr}} \\
&q^{(0)}_{\mathrm{r},\tau'} + \mathbf{u}^{\infty} \cdot \nabla_{\eta} q^{(0)}_{\mathrm{r}} = 0 \\
&q^{(1)}_{\mathrm{r},\tau'} + \mathbf{u}^{\infty} \cdot \nabla_{\eta} q^{(1)}_{\mathrm{r}} + q^{(0)}_{\mathrm{r},\tau} + \mathbf{u}^{\infty} \cdot \nabla_{x} q^{(0)}_{\mathrm{r}} + \mathbf{u}^{(0)} \cdot \nabla_{\eta} q^{(0)}_{\mathrm{r}} = 0
\end{aligned}
\tag{A.19}
$$

Sublinear growth condition yields

$$
\begin{aligned}
&q_{\mathrm{v},\tau}^{(0)} + \mathbf{u}^{\infty} \cdot \nabla_x q_{\mathrm{v}}^{(0)} + \mathbf{u}^{(0)} \cdot \nabla_\eta q_{\mathrm{v}}^{(0)} = 0 \\
&q_{\mathrm{c},\tau}^{(1)} + \mathbf{u}^{\infty} \cdot \nabla_\eta q_{\mathrm{c}}^{(1)} + \mathbf{u}^{(0)} \cdot \nabla_\eta q_{\mathrm{c},\eta}^{(1)} = -C_{\mathrm{cr}}^{(0)} \\
&q_{\mathrm{r},\tau}^{(0)} + \mathbf{u}^{\infty} \cdot \nabla_x q_{\mathrm{r}}^{(0)} + \mathbf{u}^{(0)} \cdot \nabla_\eta q_{\mathrm{r}}^{(0)} = 0.
\end{aligned} \tag{A.20}
$$

The equation for the evaporation source term is

$$
C_{\mathrm{ev}}^{(0)} = C_{\mathrm{ev}}^{**} \left(q_{\mathrm{vs}}^{(0)}(z) - q_{\mathrm{v}}^{(0)} \right) \sqrt{q_{\mathrm{r}}^{(0)}}. \tag{A.21}
$$

A.1.3. Average Equations

As explained in section 2.2, all quantities are split into η-averages defined in (2.44) and perturbations. Because $\mathbf{u}^{(0)}$ and π do not dependent on η, they are not affected by averaging. Averaging (A.10), (A.13) and (A.11) yields

$$
\begin{aligned}
\bar{w}_{\tau}^{(0)} + \mathbf{u}^{\infty} \cdot \nabla_x \bar{w}^{(0)} + \pi_x &= 0 \\
\bar{\theta}_{\tau}^{(3)} + \mathbf{u}^{\infty} \cdot \nabla_x \bar{\theta}^{(3)} + \bar{w}^{(0)} \Theta_z^{(2)} &= \frac{L^{**}\Gamma^{**} q_{\mathrm{vs}}^{**}}{p_0} \left(\overline{H_{\mathrm{q_v}} C_{\mathrm{d}}^{(0)}} + \overline{(H_{\mathrm{q_v}} - 1) C_{\mathrm{ev}}^{(0)}} \right) \\
\rho^{(0)} \nabla_x \cdot \mathbf{u}^{(0)} + \left(\rho^{(0)} \bar{w}^{(0)} \right)_z &= 0
\end{aligned} \tag{A.22}
$$

A.1.4. Perturbation Equations

Subtracting $(\mathrm{A.22})_{1,2}$ from (A.10) and (A.13) yields equations for the perturbations

$$
\begin{aligned}
&\tilde{w}_{\tau}^{(0)} + \mathbf{u}^{\infty} \cdot \nabla_x \tilde{w}^{(0)} + \mathbf{u}^{(0)} \cdot \nabla_\eta \tilde{w}^{(0)} = \tilde{\theta}^{(3)} \\
&\tilde{\theta}_{\tau}^{(3)} + \mathbf{u}^{\infty} \cdot \nabla_x \tilde{\theta}^{(3)} + \mathbf{u}^{(0)} \cdot \nabla_\eta \tilde{\theta}^{(3)} + \tilde{w}^{(0)} \Theta_z^{(2)} = \\
&\qquad \frac{L^{**}\Gamma^{**} q_{\mathrm{vs}}^{**}}{p_0} \left[H_{\mathrm{q_v}} C_{\mathrm{d}}^{(0)} - \overline{H_{\mathrm{q_v}} C_{\mathrm{d}}^{(0)}} + (H_{\mathrm{q_v}} - 1) C_{\mathrm{ev}}^{(0)} - \overline{(H_{\mathrm{q_v}} - 1) C_{\mathrm{ev}}^{(0)}} \right]
\end{aligned} \tag{A.23}
$$

A.2. Extension to General Stratification

The derivation of the model (2.70) relies on the assumption that perturbations of potential temperature from a moist adiabat are of order $\mathcal{O}(\varepsilon^3)$ and thus $\Theta^{(2)}$ satisfies (2.53). If this condition is relaxed, the ansatz still allows for the derivation of a closed model. Let $\Theta^{(2)}$ denote some arbitrary background stratification for the purpose of this section. Define the leading order moist adiabat by

$$\Theta_z^{(2)} \neq \theta_z^{\text{moist}} := -\hat{L} q_{\text{vs},z}^{(0)}. \tag{A.24}$$

The resulting counterpart to (2.60) then reads

$$\sigma \bar{w}^{(0)} \theta_z^{\text{moist}} + \overline{\left(H_{\text{q}_\text{v}} \tilde{w}^{(0)}\right)} \theta_z^{\text{moist}} = \hat{L} \overline{H_{\text{q}_\text{v}} C_{\text{d}}^{(0)}}. \tag{A.25}$$

Repeating the steps in subsection 2.2.5 yields the modified equations

$$\bar{\theta}_\tau + \mathbf{u}^\infty \cdot \nabla_x \bar{\theta} + \left(\Theta_z^{(2)} - \sigma \theta_z^{\text{moist}}\right) \bar{w} = \theta_z^{\text{moist}} w' \tag{A.26}$$

for $\bar{\theta}$ and

$$\theta'_\tau + \mathbf{u}^\infty \cdot \nabla_x \theta' + \left[\Theta_z^{(2)} - (1-\sigma)\, \theta_z^{\text{moist}}\right] w' = \sigma\,(1-\sigma)\, \theta_z^{\text{moist}} \bar{w} \tag{A.27}$$

for θ'. Replacing $(2.70)_{3,6}$ by (A.26), (A.27) still yields a closed model, but with supposedly quite different properties. The analysis of this modified model is not pursuit here.

Bibliography

[AS65] M. Abramowitz and I. A. Stegun, *Handbook of mathematical functions*, Dover Publications, 1965.

[BF85] A. Barcilon and D. Fitzjarrald, *A nonlinear steady model for moist hydrostatic mountain waves*, J. Atmos. Sci. **42** (1985), 58–67.

[BJB80] A. Barcilon, J. C. Jusem, and S. Blumsack, *Pseudo-adiabatic flow over a two-dimensional ridge*, Geophys. Astrophys. Fluid Dynamics **16** (1980), 19–33.

[BJD79] A. Barcilon, J. C. Jusem, and P. G. Drazin, *On the two-dimensional, hydrostatic flow of a stream of moist air over a mountain ridge*, Geophys. Astrophys. Fluid Dynamics **13** (1979), 125–140.

[Bou83] P. Bougeault, *A non-reflective upper boundary condition for limited-height hydrostatic models*, Mon. Wea. Rev. **111** (1983), 420–429.

[BS89] C. S. Bretherton and P. K. Smolarkiewicz, *Gravity waves, compensating subsidence and detrainment around cumulus clouds*, J. Atmos. Sci. **46** (1989), 740–759.

[Büh09] O. Bühler, *Waves and mean flows*, Cambrigde University Press, 2009.

[CEL80] G. Chimonas, F. Einaudi, and D. P. Lalas, *A wave theory for the onset and initial growth of condensation in the atmosphere*, J. Atmos. Sci. **37** (1980), 827–845.

[Cho67] A. J. Chorin, *A numerical method for solving incompressible viscous flow problems*, J. Comp. Physics **2** (1967), 12–26.

[DK82] D. R. Durran and J. B. Klemp, *On the effects of moisture on the Brunt-Väisälä frequency*, J. Atmos. Sci. **39** (1982), 2152–2158.

[DK83] ———, *A compressible model for the simulation of moist mountain waves*, Mon. Wea. Rev. **111** (1983), 2341–2361.

[DSWT03] T. Davies, A. Staniforth, N. Wood, and J. Thuburn, *Validity of anelastic and other equation sets as inferred from normal-mode analysis*, Q. J. R. Meteorol. Soc. **129** (2003), 2761–2775.

[Dur89] Dale R. Durran, *Improving the anelastic approximation*, J. Atmos. Sci **46** (1989), 1453–1461.

[Dur91] D. R. Durran, *The third-order Adams-Bashforth method: An attractive alternative to leapfrog time differencing*, Mon. Wea. Rev. **119** (1991), 702–720.

[Dur99] ———, *Numerical methods for wave equations in geophysical fluid dynamics*, Springer, 1999.

[EL73a] F. Einaudi and D. P. Lalas, *On the stability of a moist atmosphere in the presence of a background wind*, J. Atmos. Sci. **30** (1973), 795–800.

[EL73b] ———, *The propagation of acoustic-gravity waves in a moist atmosphere*, J. Atmos. Sci. **30** (1973), 365–376.

[EL75] ———, *Wave-induced instabilites in an atmosphere near saturation*, J. Atmos. Sci. **32** (1975), 536–547.

[Ema94] K. A. Emanuel, *Atmospheric convection*, Oxford University Press, 1994.

[Etl96] D. Etling, *Theoretische Meteorologie*, Springer, 1996.

[FDH91] R. Fovell, D. Durran, and J. R. Holton, *Numerical simulation of convectively generated stratospheric gravity waves*, J. Atmos. Sci. **49** (1991), 1427–1442.

[Gil82] A. E. Gill, *Atmosphere-ocean dynamics*, Academic Press, 1982.

[GK00] W. A. Gallus and J. B. Klemp, *Behavior of flow over step orography*, Mon. Wea. Rev. **128** (2000), 1153–1164.

[Gra98] W. W. Grabowski, *Toward cloud resolving modeling of large-scale tropical circulations: A simple cloud microphysics parameterization*, J. Atmos. Sci. **55** (1998), 3283–3298.

[Gra99] ———, *A parameterization of cloud microphysics for long-term cloud-resolving modeling of tropical convection*, Atmos. Res. **52** (1999), 17–41.

[Gri02] R. Grimshaw, *Group velocity*, Preprint 02-25, School of Mathematics, Loughborough University, 2002.

[HK05] D. Hinneburg and O. Knoth, *Non-dissipative cloud transport in Eulerian grid models by the volume-of-fluid (VoF) method*, Atmos. Env. **39** (2005), 4321–4330.

[IfTiL] Institut für Troposphärenforschung in Leipzig, *ASAM wiki*, http://asamwiki.tropos.de, Accessed february, 2010.

[Jak99] C. Jakob, *Cloud cover in the ECMWF reanalysis*, J. Climate **12** (1999), 947–959.

[JB85] J. C. Jusem and A. Barcilon, *Simulation of moist mountain waves with an anelastic model*, Geophys. Astrophys. Fluid Dynamics **33** (1985), 259–276.

[JK99] C. Jakob and S. A. Klein, *The role of vertically varying cloud fraction in the parameterization of microphysical processes in the ECMWF model*, Q.J.R. Meterol. Soc. **125** (1999), 941–965.

[Joo09] H. Joos, *Modelling of orographic cirrus clouds*, Ph.D. thesis, ETH Zürich, 2009.

[JSL+08] H. Joos, P. Spichtinger, U. Lohmann, J.-F. Gayet, and A. Minikin, *Orographic cirrus in the global climate model ECHAM5*, J. Geophys. Res. **113** (2008).

[KC96] J. Kevorkian and J. D. Cole, *Multiple scale and singular perturbation methods*, Springer, 1996.

[KD82] J. B. Klemp and D. R. Durran, *An upper boundary condition permitting internal gravity wave radiation in numerical mesoscale models*, Mon. Wea. Rev. **111** (1982), 430–444.

[KEC03] Y.-J. Kim, S. D. Eckermann, and H.-Y. Chun, *An overview of the past, present and future of gravity-wave drag parameterization for numerical climate and weather prediction models*, Atmosphere-Ocean **41** (2003), no. 1, 65–98.

[KL78] J. B. Klemp and D. K. Lilly, *Numerical simulation of hydrostatic mountain waves*, J. Atmos. Sci. **35** (1978), 78–107.

[Kle04] R. Klein, *An applied mathematical view of meteorological modelling*, Applied Mathematics Entering the 21st century; Invited talks from the ICIAM 2003 Congress, vol. 116, SIAM Proceedings in Applied Mathematics, 2004.

[Kle08] ———, *An unified approach to meteorological modelling based on multiple-scales asymptotics*, Adv. Geosci. **15** (2008), 23–33.

[Kle10] ———, *Scale-dependent models for atmospheric flows*, Annu. Rev. Fluid Mech. **42** (2010), 249–274.

[KM06] R. Klein and A.J. Majda, *Systematic multiscale models for deep convection on mesoscales*, Theor. & Comput. Fluid Dyn. **20** (2006), 525–551.

[KR01] M. F. Khairoutdinov and D. A. Randall, *A cloud resolving model as a cloud parameterization in the NCAR community climate system model: Preliminary results*, Geophys. Res. Letters **28** (2001), 3617–3620.

[Lal72] D. P. Lalas, *Effect of moisture on the propagation of internal and acoustic gravity waves*, Phys. Fluids **15** (1972), 734–736.

[Lig78] J. Lighthill, *Waves in fluids*, Cambridge University Press, 1978.

[Lin81] R. S. Lindzen, *Turbulence and stress owing to gravity wave and tidal breakdown*, J. Geophys. Res. **86** (1981), 9707–9714.

[LM04] C. Liu and M. W. Moncrieff, *Effects of convectively generated gravity waves and rotation on the organization of convection*, J. Atmos. Sci. **61** (2004), 2218–2227.

[LR01] T. P. Lane and M. J. Reeder, *Convectively generated gravity waves and their effect on the cloud environment*, J. Atmos. Sci. **58** (2001), 2427–2440.

[LRC01] T. P. Lane, M. J. Reeder, and T. L. Clark, *Numerical modeling of gravity wave generation by deep tropical convection*, J. Atmos. Sci. **58** (2001), 1249–1274.

[LZ80] M. A. LeMone and E. J. Zipser, *Cumulonimbus vertical velocity events in GATE. Part I: Diameter, intensity and mass flux*, J. Atmos. Sci. **37** (1980), 2444–2457.

[Maj07] A. J. Majda, *Multiscale models with moisture and systematic strategies for superparameterization*, J. Atmos. Sci. **64** (2007), 2726–2734.

[Map93] B. E. Mapes, *Gregarious tropical convection*, J. Atmos. Sci. **50** (1993), 2026–2037.

[MB03] M. M. Miglietta and A. Buzzi, *A numerical study of moist stratified flow regimes over isolated topography*, Q. J. R. Meteorol. Soc. **130** (2003), 1749–1770.

[McL98] C. McLandress, *On the importance of gravity waves in the middle atmosphere and their parameterization in general circulation models*, J. Atmos. Terr. Phys. **60** (1998), no. 14, 1357–1383.

[MK03] A. Majda and R. Klein, *Systematic multi-scale models for the tropics*, J. Atmos. Sci. **60** (2003), 393–408.

[MR05] M. M. Miglietta and R. Rotunno, *Simulations of moist nearly neutral flow over a ridge*, J. Atmos. Sci. **62** (2005), 1410–1427.

[OF02] S. Osher and R. Fedkiw, *Level set methods and dynamic implicit surfaces*, Springer, 2002.

[RKM10] D. Ruprecht, R. Klein, and A. J. Majda, *Modulation of internal gravity waves in a multi-scale model for deep convection on mesoscales*, J. Atmos. Sci. (2010), In press.

[Saw59] J. S. Sawyer, *The introduction of the effects of topography into methods of numerical forecasting*, Q. J. R. Meteorol. Soc. **85** (1959), 31–43.

[Sco49] R. S. Scorer, *Theory of waves in the lee of mountains*, Q. J. R. Meteorol. Soc. **75** (1949), 41–56.

[Ste05] B. Stevens, *Atmospheric moist convection*, Annu. Rev. Earth. Planet. Sci. **33** (2005), 605–643.

[Sur89] N. Surgi, *Systematic errors of the FSU global spectral model*, Mon. Wea. Rev. **117** (1989), 1751–1766.

[TL79] P. D. Thomas and C. K. Lombard, *Geometric conservation law and its application to flow computations on moving grids*, AIAA Journal **17** (1979), no. 10, 1030–1037.

[Tom02] A. M. Tompkins, *A prognostic parameterization for the subgrid-scale variability of water vapor and clouds in large-scale models and its use to diagnose cloud cover*, J. Atmos. Sci. **59** (2002), 1917–1942.

[Vat05] S. Vater, *A new projection method for the zero Froude number shallow water equations*, PIK Report 97, Potsdam Institute for Climate Impact Research, 2005.

[VK09] S. Vater and R. Klein, *Stability of a cartesian grid projection method for zero Froude number shallow water flows*, Numerische Mathematik **113** (2009), no. 1, 123–161.

[WSD96] M. G. Wurtele, R. D. Sharman, and A. Datta, *Atmospheric lee waves*, Annu. Rev. Fluid Mech. **28** (1996), 429–476.

Acknowledgements

First of all I want to thank my advisor Prof. Rupert Klein whose support and advise made this thesis possible.

I also want to thank Prof. Andrew J. Majda for being the second advisor as well as for numerous helpful suggestions and comments on this work.

I am also thankful to the whole AG Klein for plenty of interesting discussions, especially to Stefan Vater for answering all my questions about the projection method.

Special thanks to Dr. Oswald Knoth for inviting me to Leipzig and providing me a comprehensive introduction into the ASAM code.

I also want to thank Prof. Oliver Bühler for providing me excerpts from his book and for helping me with the theory of critical layers during his stay in Berlin.

Thanks to Prof. Michael Minion for lots of helpful hints during his stay at ZIB.

I also thank Dr. Peter Spichtinger for his interesting comments and helpful literature on parameterizations of gravity wave drag.

Parts of this work are published in [RKM10]. The three anonymous referees provided very constructive reviews that also helped to improve this thesis.

Abstract

The thesis presents the analysis of a reduced model for modulation of internal gravity waves by deep convective clouds. The starting point for the derivation are conservation laws for mass, momentum and energy coupled with a bulk micro-physics model describing the evolution of mixing ratios of water vapor, cloud water and rain water. A reduced model for the identified scales of the regime is derived, using multi-scale asymptotics. The closure of the model employs conditional averaging over the horizontal scale of the convective clouds.

The resulting reduced model is an extension of the anelastic equations, linearized around a constant background state, which are well-known from meteorology. The closure of the model is achieved purely by analytical means and involves no additional physically motivated assumptions.

The essential new parameter arising from the coupling to a micro-physics model is the area fraction of saturated regions on the horizontal scale of the convective clouds. It turns out that this parameter is constant on the employed short timescale. Hence the clouds constitute a constant background, modulating the characteristics of propagation of internal waves. The model is then investigated by analytical as well as numerical means. Important results are, among others, that in the model moisture (i) inhibits propagation of internal waves by reducing the modulus of the group velocity, (ii) reduces the angle between the propagation direction of a wave-packet and the horizontal, (iii) causes critical layers and (iv) introduces a maximum horizontal wavelength beyond which waves are no longer propagating but become evanescent. The investigated examples of orographically generated gravity waves also feature a significant reduction of vertical momentum flux by moisture.

The model is extended by assuming systematically small under-saturation, that is saturation at leading order. The closure is similar to the original case but requires additional assumptions. The saturated area fraction in the obtained model is no longer constant but now depends nonlinearly on vertical displacement and thus on vertical velocity.

Zusammenfassung

Die Arbeit präsentiert die Analyse eines reduzierten Modells für die Modulation von internen Schwerewellen durch hochreichende Konvektionswolken. Der Ausgangspunkt der Herleitung sind Erhaltungsgleichungen für Masse, Impuls und Energie, gekoppelt mit einem „bulk“ Modell für die Feuchteprozesse, welches die Entwicklung der Mischungsverhältnisse von Wasserdampf, Wolkenwasser und Regenwasser beschreibt. Mittels Techniken der Mehrskalenasymptotik wird ein reduziertes Modell für die identifizierten Skalen des analysierten Regimes hergeleitet. Die Schließung des Modells verwendet bedingte Mittelungen über die horizontale Skala der Konvektionswolken.

Das resultierende reduzierte Modell ist eine Erweiterung der aus der Meteorologie bekannten, um einen konstanten Hintergrund linearisierten, anelastischen Gleichungen. Hervorzuheben ist an dieser Stelle, dass die Schließung rein analytisch funktioniert und keine zusätzlichen physikalisch motivierten Approximationen notwendig sind.

Der wesentliche neue Parameter, welcher durch die Koppelung mit dem mikrophysikalischen Modell hinzukommt, ist der Flächenanteil gesättigter Bereiche auf der Skala der konvektiven Wolkentürme. Es zeigt sich, dass dieser Parameter auf der betrachteten kurzen Zeitskala konstant ist. Die Wolken bilden also in dem Modell einen konstanten Hintergrund, welcher die Eigenschaften der internen Schwerewellen moduliert. Im weiteren wird das Modell sowohl analytisch als auch numerisch untersucht. Zentrale Ergebnisse sind unter anderem, dass Feuchtigkeit (i) die Ausbreitung von Schwerewellen beeinträchtigt, bedingt durch eine Reduzierung des Betrags der Gruppengeschwindigkeit, (ii) den Winkel zwischen der Ausbreitungsrichtung eines Wellenpaketes und der Horizontalen reduziert, (iii) kritische Schichten erzeugen kann sowie (iv) eine maximale horizontale Wellenlänge bewirkt, oberhalb welcher Moden sich nicht länger vertikal fortpflanzen, sondern mit zunehmender Höhe abklingen. Die untersuchten Beispiele von orographisch erzeugten Schwerewellen zeigen zudem eine deutliche Reduzierung des vertikalen Impulsflusses durch Feuchtigkeit.

Das ursprüngliche Modell wird erweitert, indem systematisch kleine Untersättigung, d.h. Sättigung in führender Ordnung, angenommen wird. Die Schließung funktioniert ähnlich wie im ursprünglichen Fall, braucht jetzt aber zusätzliche Annahmen. Im resultierenden Modell ist der Flächenanteil der gesättigten Bereiche nicht länger konstant, sondern hängt nichtlinear von der vertikalen Auslenkung und damit von der Vertikalgeschwindigkeit ab.

Lebenslauf

Die online veröffentlichte Version enthält keinen Lebenslauf.